UNIVERSITY OF TWENTE.

Analysis of the electrophysiological data acquired on the PhysioHeart™ platform (ex vivo beating heart)

July 18, 2024

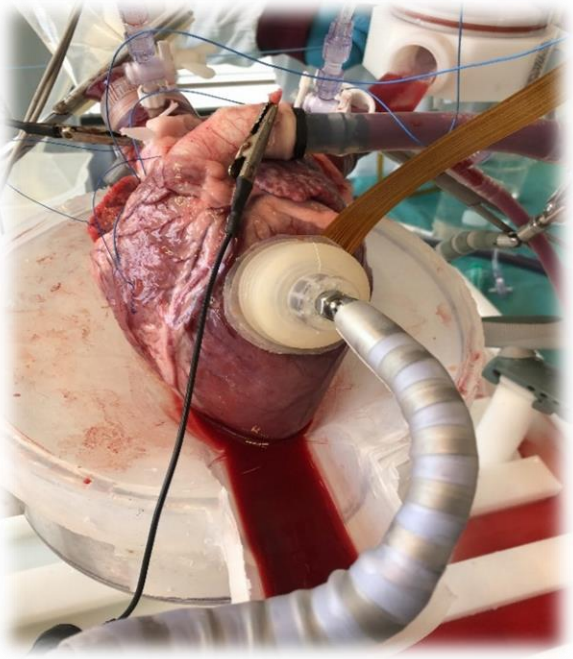

Author
Simone van der Hoek

Supervisors/committee
Prof. Dr. -ing. Jutta Arens (UT)
Ing. Bart Smeets (LifeTec)
Dr. -ing. Renate Boekhoven (LifeTec)
Dr. Frank Halfwerk (UT)
Dr. Venkat Kalpathy Venkiteswaran (UT)

Master thesis organization
LifeTec Group B.V.

Duration + EC
13-11-2023 until 18-07-2024
45 EC

MASTER THESIS – FACULTY OF ENGINEERING TECHNOLOGY
DEPARTMENT OF BIOMECHANICAL ENGINEERING

Abstract

Cardiovascular diseases require effective preventive strategies and minimally invasive interventions. LifeTec Group B.V. developed the PhysioHeart™ platform using slaughterhouse hearts to simulate cardiac conditions. Enhanced for MRI-guided therapies, the platform aims for real-time treatment visualization. This research compares the 2-chamber and 4-chamber configurations to determine the better setup. Ion imbalances were induced to assess their impact on electrophysiology and mechanical activation and local stimulation was applied, to show the possibility of detecting arrhythmic substrates. Results showed that local activation can be effectively measured through grid pacing. The 2-chamber setup offered more stability and consistent results. Electrophysiology and mechanical activation patterns combined effectively detected ion imbalances.

Contents

1 Introduction

[1] Among the leading causes of illness and death globally are cardiovascular diseases. Given this, implementing strategies to prevent these conditions and manage their risk factors is crucial, as it can alleviate the burden on the healthcare system. However, when interventions are necessary, keeping them as minimally invasive as possible is preferable. This can be achieved through drugs and catheter-deliverable therapies, including ablation, annuloplasty rings, valve substitutes, and heart pumps. Additionally, the potential use of robots in the operating room is becoming increasingly essential.

The safety and effectiveness standards for drugs and devices are exceptionally high, necessitating meticulous development and testing processes to obtain certification for use and reimbursement. Before employing these drugs and devices in humans, the final steps involve pre-clinical trials. During these trials, the designs and action mechanisms are tested in animals. The animal's heart must closely resemble human anatomy and pathophysiological conditions for cardiovascular studies.

[2] Mice and rats are the most commonly used animals in heart failure studies due to their practicality, cost-effectiveness, and genetic similarity to humans. Mice, in particular, are ideal for investigating heart function, structure, and diseases because of their ease of handling, rapid reproduction, and low maintenance costs. They are well-suited for drug tests and therapeutic interventions. However, mice are inadequate for testing large devices like catheters and valves. Rats, being larger, are more practical for surgical procedures but still not suitable for catheter and valve studies. For such purposes, pigs are preferred due to their anatomical and physiological similarities to humans, accessibility of coronary arteries, tolerance to procedures, and translational relevance in cardiology research.

If a product fails during pre-clinical trials, companies must redesign and retest, incurring significant expenses and additional time. To mitigate this risk and minimize time to market, technologies should be exposed to scenarios mimicking real life, e.g., platforms addressing challenges early in their development phase. This reduces the likelihood of high re-iteration costs and saves time.

To streamline the transition from benchtop environment to in vivo testing, an ex vivo approach utilizing slaughterhouse material offers a promising solution. LifeTec Group B.V. is committed to delivering authentic, pertinent, and customized testing platforms characterized by reliability and reproducibility, accurately mirroring in vivo conditions. This approach furnishes a realistic, life-like environment and holds the potential to serve as a viable alternative to certain aspects of whole-animal experiments. One of the platforms developed by LifeTec Group B.V. is an ex vivo isolated beating heart (PhysioHeart™ platform), which will be the focus for the research described in this report.

The PhysioHeart™ has emerged as a valuable tool for studying heart failure, to test supporting heart pumps and other structural heart devices, owing to its ability to mimic the pumping and contracting behavior of a real heart. However, its electrical activity and behavior remain relatively unexplored. Recognizing this gap, LifeTec Group B.V. is actively participating in the SIGNET project to investigate the electrophysiology of the platform. The anticipated outcomes of this project include the development of core technologies for higher precision and motion compensated MR-guided therapies. Additionally, the project aims to implement necessary architecture and interface modifications to support multiple treatment modalities within a single, maintainable, standardized, and expandable platform. For LifeTec Group B.V., the expected technology and solution outputs involve utilizing the PhysioHeart™ platform to evaluate cardiac MRI in the presence of ablation catheters, with the potential to visualize treatment effects in real time. To ensure real-time visualization of treatment effects, it is crucial to first determine

the physiological performance of the PhysioHeart™ before progressing to MRI compatibility. Therefore, this study focuses on investigating the electrophysiology of the PhysioHeart™ platform.

The physiological behavior of the PhysioHeart™ platform is amongst others regulated by the ion balance in the blood and can be represented by the electrophysiological and mechanical activation of the heart. A standard PhysioHeart™ platform is based on the left side of the heart only, which is called the 2-chamber configuration. In terms of electrophysiological behavior it is however hypothesized by the SIGNET consortium that a whole heart experiment will lead to more physiologically correct results. To understand this, it must be known how the cardiac cycle works [3]. In case of a normal heart, the action potential starts in the SA node and causes the atrial muscle cells to depolarize, see the starting point of Figure 1. The depolarization of the atrial muscle cells leads to the contraction of the atria, which causes the pressure to increase in the atria. Once the atrial pressure exceeds ventricular pressure the mitral and tricuspid valve open nearly simultaneously and the blood flows into the ventricles. Once the ventricles are filled, the electrical potential travels through the AV node, down to the bundle of His, and through the Purkinje fibers, causing the ventricle to depolarize, resulting in contraction of the ventricles. Due to this contraction the pressure in the ventricles exceeds the pressure in the atria and the mitral and tricuspid valves will close. The pressure in the ventricles will increase again until ventricular pressure exceeds aortic and pulmonary pressure causing the aortic and pulmonary valves to open. In case of the 2-chamber configuration on the PhysioHeart™ platform the right atrium is only filled by the coronary veins and as it takes longer for the atrium to fill causing the mean blood pressure to be lower than physiological. By comparing the 2-chamber and 4-chamber configurations and assessing their resemblance to normal heart physiology, this study aims to determine which setup more accurately replicates physiological conditions. This evaluation will guide the selection of the optimal configuration to use on the PhysioHeart™ platform projects. Additionally, to ensure the visualization of treatment effects, the platform should also accurately measure local activation. To achieve this, tests will be conducted using local stimulations.

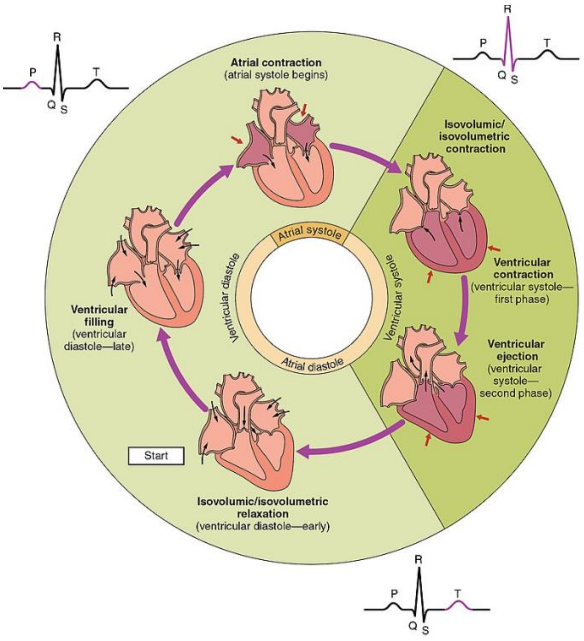

Figure 1: The cardiac cycle [36].

The mechanical activation is an important aspect alongside electrophysiology. It is hypothesized that the PhysioHeart™ platform will show a more pronounced effect on the mechanical activation than on electrophysiology when compared to the 2-chamber and 4-chamber configurations. In the 2-chamber configuration, abnormal pressure exists in the right atrium, where many baroreceptors are located. The heart might try to compensate for this, using compensatory mechanisms like an increase in heart rate, enhanced contractility, etc., resulting in prominent changes in mechanical activation and electrophysiology [3]. However, since the platform lacks a neural network, baroreceptors signaling to the brain is absent, leading to an expectation that the mechanical activation is more prominently visible. By measuring both electrophysiology and mechanical activation, it can be tested if this expectation holds and whether the difference or combined results can aid in diagnosing various conditions and detect ion imbalances as mentioned below.

Finally, the ion balance plays an important role as well; chapters 2.1, 2.3 and 9.1 provide an in-depth explanation regarding the physiology of the heart's intrinsic cardiac conduction systems and what kind of ions are involved. The primary ions that play a role in the conduction system are sodium, calcium, potassium, and less-known magnesium. It is known that an imbalance will cause the electrophysiology as well as the mechanical activation patterns to be altered. By testing boluses of these ions on the PhysioHeart™ platform it is expected to identify how the heart responds to an imbalance in the ions. If we can detect the ion imbalance by means of electrophysiology in an early stage, even before the mechanical alteration takes place, it would be possible to maintain the stability of the heart even better by adding the correct compound.

2 State of technology

2.1 Electrophysiology

Electrophysiology studies electrical properties and patterns within biological cells and tissue. When focusing on the heart, the name is extended to cardiac electrophysiology. This field focuses on the heart's electrical system and diagnosing, treating, and managing arrhythmias. Key aspects of cardiac electrophysiology include understanding cardiac action potentials, ion channels, the heart's conduction system, the basics of Electrocardiography (ECG), the workflow of electrophysiological studies (EPS), and cardiac mapping.

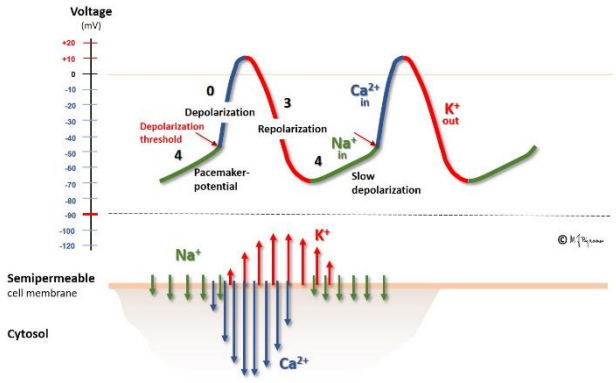

Figure 2: The action potential in the sinoatrial (SA) node [37].

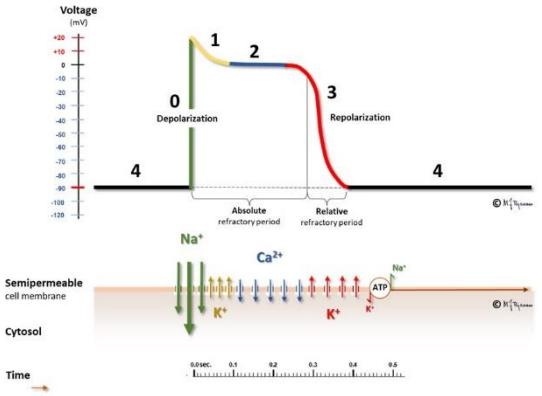

Figure 3: The action potential in the contractile myocardial cells in the ventricular muscle [37].

2.1.1 The heart's conduction system

The heart's intrinsic conduction system, including its natural pacemaker, coordinates its rhythm and contraction. This system allows the heart to spontaneously depolarize and generate action potentials that spread through the myocardium, the heart's muscle layer, causing it to contract. The myocardium has two types of cells: nodal cells and contractile cells. Nodal cells can intrinsically polarize and generate action potentials in the SA node, AV node, Bundle of His, bundle branches, and Purkinje fibers. These cells are connected by gap junctions, allowing fast conduction between the nodal cells and slower conduction between the nodal and contractile cells [4].

2.1.2 The creation of action potential

Initially, sodium ions enter nodal cells via funny sodium channels, raising the potential from -60 mV to -55 mV (see Figure 2 for the full cycle). This triggers T-type calcium channels to open, increasing the potential until the depolarization threshold is reached. Then, L-type calcium channels open, causing the cell to fully depolarize to around 10 to 40 mV. Positive ions flow through gap junctions from nodal to contractile cells, raising their potential from -90 mV to -70 mV. This threshold triggers rapid depolarization to 10 mV (phase 0) as sodium channels open.

After phase 0, sodium channels close, and potassium channels open, causing the potential to drop from 10 mV to 0 mV (phase 1). At 0mV, more calcium channels open, balancing calcium inflow with potassium outflow, creating a plateau phase (phase 2). Calcium from the sarcoplasmic reticulum binds to troponin, initiating muscle contraction. Potassium channels then open in nodal cells, reducing the potential back to -60 mV. The cycle repeats as funny sodium channels reopen.

In contractile cells (see Figure 3), potassium channels open wider, and calcium channels close, causing repolarization back to -90 mV (phase 3). During the refractory period (phase 4), cells reset their ion gradients through active transport, preparing for the next cycle.

The ECG shown in Figure 4 reflects these phases: the P wave (atrial depolarization), PR interval (AV node conduction), QRS complex (ventricular depolarization), and QT interval (ventricular action potential duration). Each action potential phase contributes to the overall ECG.

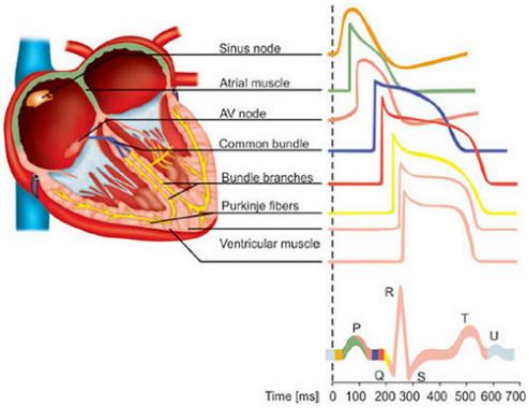

Figure 4: The difference in cardiac action potentials along the various regions of the cardiac conduction system and the corresponding ECG [38].

For a more in-depth explanation of the action potential, see paragraph 9.1 in the appendix or the lectures by Zack Murphy [4] and [5].

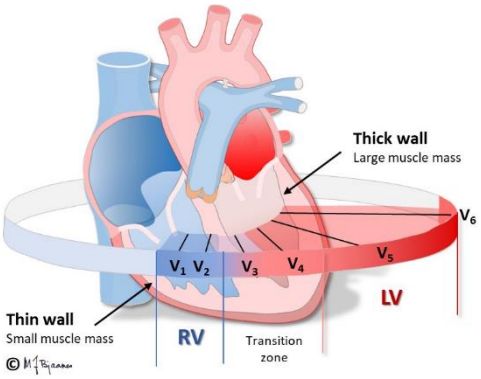

Figure 5: The location of the 6 chest leads with respect to the heart [40].

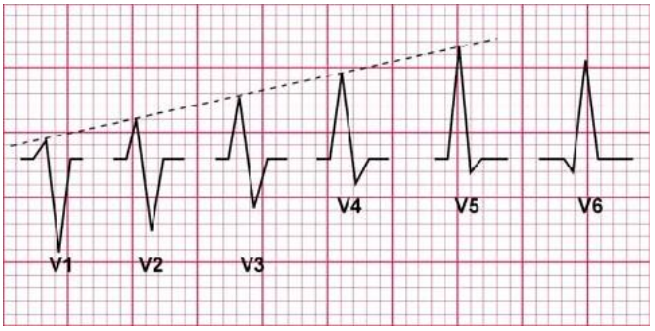

Figure 6: R and S-wave propagation from V1 to V6. R-wave starts out small and becomes larger towards V6. The S-wave starts out larger and becomes smaller towards V6 [39].

2.1.3 ECG waveforms

A standard ECG has 12 leads: three limb leads, three augmented unipolar limb leads (aVR, aVL, aVF), and six precordial chest leads (V1 to V6), recorded from 10 electrodes placed on the limbs and chest. The chest leads, particularly significant for diagnosing heart conditions, are unipolar and placed at specific chest locations to provide detailed information about different heart regions, as shown in Figure 5.

Leads V1 to V3 focus on the right ventricle, V2-V3 on the basal septum, V2-V4 on the anterior wall, and V5-V6 on the lateral wall of the left ventricle. The R and S waves are the key components in these leads, with the R-wave representing an upward deflection due to ventricular depolarization, and the S-wave representing a downward deflection.

Significant Q waves are typically absent in leads V1 to V3. The R-wave vector is small in V1, indicating the right ventricle, and increases in magnitude through V6, reflecting the larger left ventricular vector. The S-wave decreases from V1 to V6, as the depolarization direction becomes nearly perpendicular to the electrodes in V6. Figure 6 illustrates these changes, showing an increase in R-wave and a decrease in S-wave from V1 to V6.

For a more in-depth explanation of the action potential, see paragraph 9.1 in the appendix or the lectures by Zack Murphy [6].

2.1.4 Electrophysiology studies

Hospital electrophysiology studies involve more than just measuring ECG [7]. Multi-electrode catheters measure electrical signals at multiple locations in the heart, providing insight into how electrical impulses move through it. Throughout the study, electrical signals can be sent through the catheter to manipulate the speed of heartbeats. Medication can also be delivered to block or slow down electrical activity in specific areas, managing irregular heart rhythms.

Moreover, cardiac mapping, a process to create a heart map, is performed. This mapping determines optimal sites for procedures like cardiac ablation, which uses a different catheter to apply hot or cold energy to target specific heart areas. This process creates scar tissue, blocking irregular electrical signals and restoring a typical heart rhythm.

Cardiac mapping can use various methods, such as body surface, endocardial, and epicardial mapping. The precordial lead on a standard ECG falls under body surface mapping. Endocardial mapping uses a catheter to place places electrodes on the inner heart wall, while epicardial mapping places them directly on the outer heart wall, like during open-heart surgery. Additionally, high-density maps can be generated using electrode arrays or catheters with numerous closely spaced electrodes, providing detailed information applicable to both the endocardium and epicardium, enabling comprehensive mapping of heart electrical activity.

These mapping technologies rely on unipolar or bipolar electrograms as a base [8][9]. Unipolar electrograms offer insight into electrical activity at a specific electrode relative to a common reference point, aiding in understanding the spatial distribution of electrical signals on the heart's surface. Analyzing the steepest downward slope in unipolar electrograms determines local activation times (AT) at individual electrode sites.

Bipolar electrograms measure potential differences between adjacent electrodes, providing information about electrical conduction between those points. Analyzing bipolar electrogram shape and timing helps ascertain the direction and velocity of the electrical wavefront moving through tissue. Bipolar mapping is helpful in identifying re-entry circuits and understanding mechanisms behind certain arrhythmias.

Unipolar electrograms exhibit waveforms similar to ECG waves from leads V1 to V6, depending on electrode placement. For example, electrodes placed on the right ventricle produce an ECG wave resembling lead V1, while those on the left ventricle create a wave similar to lead V5. In bipolar electrograms, verification is slightly more challenging as the resulting activation pattern is similar to the differential of a unipolar signal, depending on electrode location.

2.1.5 Measurement parameters

To visualize and analyze the recorded electrograms multiple parameters can be measured like the AT, the recovery time (RT), activation recovery interval (ARI), and the conduction velocities.

Activation time

The AT refers to the initiation of the electrical activity within the cardiac tissue. It marks the beginning of the depolarization. In terms of the ECG the AT is determined as the maximum negative slope in the

QRS complex. Understanding AT is crucial for diagnosing and treating cardiac arrhythmias, as abnormalities in AT can lead to irregular heart rhythms [8][10]. In case of the bipolar electrograms the AT is determined as the maximum negative peak.

Recovery time

The RT is determined as the maximum positive slope of the T complex in case of the unipolar electrograms and marks the completion of the depolarization. In case of the bipolar electrograms or the derivative of the unipolar electrograms the RT is determined as the maximum positive peak in the electrogram. During the recovery period the cell's return to its resting level. The duration of recovery period can vary depending on factors such as the type of cardiac tissue and the presence of certain ions. In some cases, a prolonged recovery period might indicate cardiac conditions such as arrythmias or conduction abnormalities [10].

Activation Recovery Interval

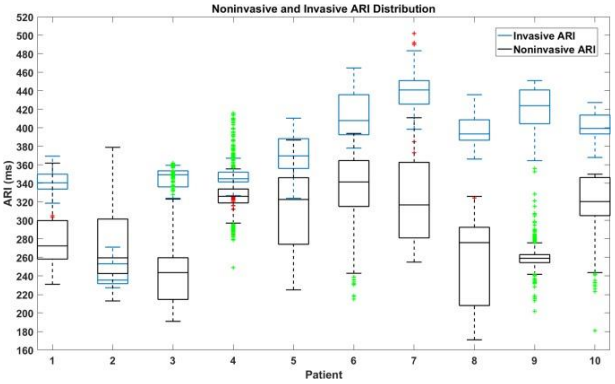

Figure 7: Comparison of invasive and noninvasive ARI by Yang et al [11].

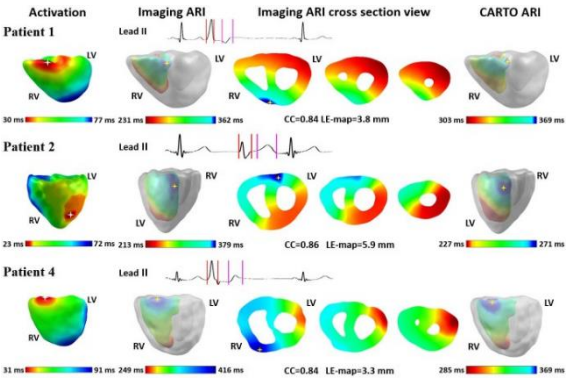

Figure 8: Activation, 3D ARI and CARTO ARI maps by Yang et al [11].

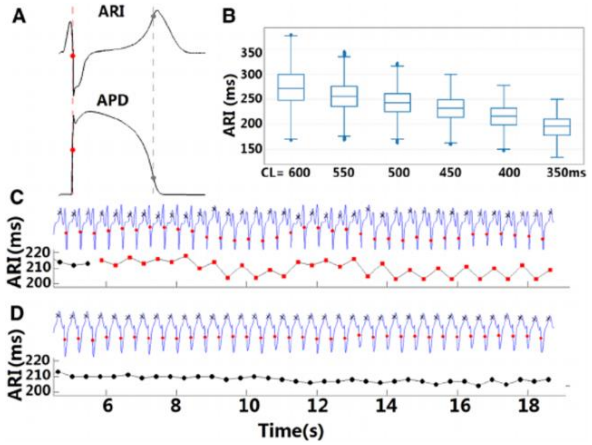

Figure 9: The effect of different pacing ranges on the ARI. The longer the cycle (lower HR), the higher the ARI [12].

The ARI is a crucial metric for understanding ventricular repolarization. It measures the duration from the onset of activation to the completion of repolarization in cardiac cells. More easily put the ARI is the RT minus the AT [10]. Any prolongation or shortening of the ARI could signal abnormal electrical activity in the heart, potentially leading to arrhythmias like atrial fibrillation or ventricular tachycardia. Monitoring changes in ARI offers valuable insights into the impact of ion balance on cardiac function, as ion balance influences cellular mechanisms and electrical potential. By imaging ARI, the repolarization dynamics across the grid can be visualized. Variations within the ARI can indicate heterogeneity in repolarization, which is crucial in understanding the risk of arrhythmias. Areas with long ARI are often associated with arrhythmic substrates and may serve as targets for interventions like catheter ablation. Also, the effect of the treatment can be detected by looking at an ARI map. For the range of the ARI Yang et al [11] performed a study regarding the ARI imaging of premature ventricular contraction, showing that there is a large variety between the ARI across a map in comparison to the mean. Figure 8 shows the maps created by a 3D ARI mapping system and the other was an interpolated CARTO ARI map. These results show

differences between the maps of different patients, which is also evident from Figure 7. From the activation and ARI maps in Figure 8 it can be seen that the longest ARI is present at the earliest activation and the shortest at the latest activation during pacing.

The main reason for the difference between the different patients is that they all had a different heart rate (HR) during the measurements. In Figure 9 the in vivo recordings of the ARI by Zhou et al [12] are shown. Within these results it can be seen that with an increasing HR the ARI will decrease. At a HR of 100 bpm for example the ARI should be between 250 to 300 ms. However, according to the Imaging ARI used by Yang et al [11] a patient that had a HR of approximate 95 bpm (patient 6) shows and ARI that ranges from 320 to 340 ms, which is a lot higher than the study by Zhou [12]. But patient 6 has premature ventricular contractions, which could cause the ARI to be higher. A study by Ghosh et al [13] mentions that for a normal epicardial left ventricle ARI is between 280 to 300 ms with a dispersion of 40 – 50 ms, they however do not mention what the related HR is in this study and thus hard to compare with the other findings. In general, the expected range in a healthy human heart for a HR of 100 bpm should be between 250 and 300 ms with an expected dispersion of approximately 40 – 50 ms. In case of a porcine heart the ARI range found for a sinus rhythm with a HR of 100 bpm was between 270 to 331 ms with a dispersion of 20 ms, this range is slightly higher than the range for human hearts [14].

Conduction velocity

The conduction velocity (CV) describes the speed and direction of the electrical activation propagating through the heart. Disorders like myocardial ischemia and infarction, atrial fibrillation, and a wide range of ventricular arrhythmias can introduce changes in CV. By accurately measuring CV, it is possible to identify arrhythmias and localize diseased tissue. The challenge with CV is that reconstructing the wavefront requires dense sampling on the surface of the heart. Once recordings are made, the data can be processed to reconstruct high-density maps of CV.

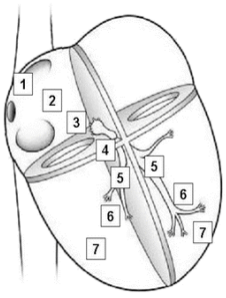

Normal Activation Sequence	Structure	Conduction velocity (m/sec)	Pacemaker rate (beats/min)
1	SA node	< 0.01	60 – 100
2	Atrial myocardium	1.0 – 1.2	None
3	AV node	0.02 – 0.05	40 – 55
4	Bundle of His	1.2 – 2.0	25 – 40
5	Bundle branches	2.0 – 4.0	25 – 40
6	Purkinje network	2.0 – 4.0	25 – 40
7	Ventricular myocardium	0.3 – 1.0	None

Figure 10: CV and intrinsic pacemaker rates at different location in the heart along the conduction pathway [41].

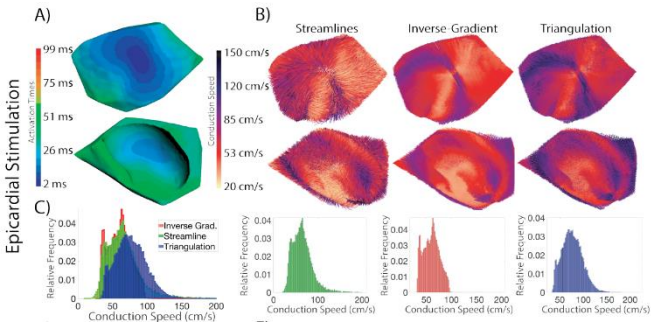

Figure 11: Epicardial AT and CV maps. With histograms of the overall CV for different methods [15].

Some methods currently used include triangulation, the inverse gradient method, and a streamline-based technique (see Figure 11). The streamline method is better suited for detailed studies were visualizing the conduction pathways and understanding the spatial propagation of the wavefront is crucial. The inverse gradient method is preferred for applications requiring robust and quick calculations of CV, such as clinical settings or large-scale studies where computational efficiency and noise robustness are important. Therefore, it is often more beneficial to use the inverse gradient method [15].

Regarding the range of CV in the heart, it depends on the location of the electrodes and whether the measurements are taken on the epicardium or the endocardium. In Figure 10, the CV within the myocardium are shown for different regions of the heart. From this information, it can be seen that in the ventricular myocardium, the CV ranges from approximately 0.3 to 1 m/s in a human heart, in case of a porcine heart this range is similar.

2.1.6 Inter-electrode spacing

Another important aspect is the inter-electrode spacing on the catheter as well as an electrode grid. With regards to unipolar signals, numerous studies recommend an inter-electrode spacing of 2 mm. However, the electrode grid available for this study has a 4 mm inter-electrode spacing. Therefore, a literature review was conducted to assess the impact of different inter-electrode spacings, given the challenge of obtaining a 2 mm spaced grid.

Abdi et al. [16] examined the effect of electrode size and inter-electrode spacing on epicardial electrograms and activation properties. They simulated atrial tissue as a 2D monolayered grid of cells and conducted a clinical trial on nine atrial sites in multiple humans. Optimal interelectrode distance for unipolar signals was found to be approximately 1.9 mm for electrodes with a diameter of 0.5 mm. Given our electrode diameter of 1 mm, the optimal inter-electrode spacing would likely be around 2.4 mm. These values, however, were determined through simulations, and only a setup with a 2 mm inter-electrode spacing and a 0.5 mm diameter was clinically tested. Remarkably, the correlation coefficient between simulation and clinical trial results was 0.97, indicating a strong relationship. Nonetheless, it remains unclear whether this high correlation coefficient applies to larger inter-electrode spacings or diameters.

In a related study, Rodrigo et al. [17] suggested that the maximum inter-electrode distance for detecting sub-endocardial microanatomic re-entries sustaining atrial fibrillation should be smaller than 4 mm. They found unipolar mapping to be more reproducible than bipolar mapping, as bipolar electrodes were highly sensitive to orientation relative to the common path of conduction.

Beheshti et al. [18] elucidated the relationship between bipolar voltage and inter-electrode spacing, particularly in the context of healthy and diseased myocardial tissue in porcine models. Their findings indicate a linear relationship between observed bipolar voltage values and inter-electrode spacing up to approximately 4 mm. For healthy tissue, electrode orientation had minimal effect on bipolar voltage values for inter-electrode spacings greater than 3.6 mm. However, in diseased tissue, this trend was observed for spacings less than 3.6 mm. Consequently, an inter-electrode spacing of 4 mm should suffice for healthy tissue, but it might overlook crucial information in unhealthy tissue, as activation maps could appear more smoothed out.

Takigawa et al. [19] investigated the impact of bipolar electrode spacing on both far-field and near-field electrograms in infarcted sheep, using inter-electrode spacings of 2, 4, and 8 mm. Their findings suggest a significant loss of information with increased spacing. Larger spacings might fail to accurately distinguish local tissue characteristics and could misidentify scars or normal tissue as areas of abnormal activity. For identifying surviving tissue within a scar, a closely spaced electrode grid would be preferred. However, a larger spaced grid might still be useful for identifying interesting electrograms nearby, albeit not directly underneath the grid.

Concerning omnipolar electrograms (OEs), Letchumy et al. [20] identified an inter-electrode spacing of either 2 mm or 3 mm as optimal for capturing high-quality OEs from human myocardial tissue. This

spacing effectively minimizes cancellation effects associated with smaller spacings and enhances the localization of activation signals. Electrode configurations with spacing exceeding 4 mm were less effective in accurately delineating the myocardial tissue's underlying characteristics due to the presence of multiple minima in the OEs, complicating the differentiation between healthy and scarred regions. Conversely, an inter-electrode spacing of less than 2 mm resulted in low-amplitude signals, making them more susceptible to noise interference and compromising the clarity and accuracy of tissue characteristics. Therefore, the optimal range for OEs lies between 2 and 4 mm. As omnipolar electrograms are derived from unipolar electrograms, it is expected that the range of 2 to 4 mm would also provide sufficient unipolar electrograms.

An inter-electrode spacing of 4 mm for both unipolar and bipolar configurations is considered a practical compromise for epicardial measurements, balancing the need for high-quality signal acquisition with the practical limitations of electrode size and spacing. High accuracy in voltage is crucial for determining AT, a fundamental parameter in electrophysiological studies for understanding the timing of myocardial tissue depolarization. Integrating the cross-configuration approach into clinical practice holds significant promise for advancing the field of cardiac electrophysiology but requires further validation to ensure its robustness and reliability in clinical settings.

Some studies, such as Magtibay et al [21] and van Schie et al [22], employ calculated bipolar signals. In both cases the bipolar signals are then used to calculate omnipolar signals. They subtract the unipolar signals that are close to each other. Another possibility is to take the first derivative of the unipolar signals, which should be proportional to each other as long as the time difference between the signals is small enough. This condition is met if the distance between the poles is sufficiently small. The question arises, however: how small can this distance be? Van Schie et al uses an inter-electrode spacing of 2 mm and Magtibay et al use inter-electrode spacings of 2, 2.4 and 4 mm.

To our knowledge, only one study has investigated computed bipolar electrograms from unipolar epicardial electrograms [23]. In this study, both bipolar and unipolar electrograms were measured with an inter-electrode distance of 2 mm. According to this paper, bipolar electrograms can be accurately reconstructed from unipolar electrodes with an inter-electrode spacing of 2 mm, as the correlation coefficient between the measured and calculated bipolar electrograms was greater than 0.9 for 94% of the electrograms. Larger inter-electrode spacing may result in greater differences between the shapes and AT of measured and calculated electrograms, thereby decreasing the correlation coefficient between the two.

Both Van Schie et al and Magtibay et al use a 2 mm grid, which is small enough to calculate the bipolar electrograms. However, Magtibay et al also uses larger size inter-electrode spacings but does not provide enough information about the accuracy of the measurements when using a higher inter-electrode spacing, nor do they provide more detail for identifying scars/threshold values for scars and scar borders using different inter-electrode spacings. From these studies, it remains unclear if a larger inter-electrode spacing provides good results.

2.1.7 Filtering

To process the unipolar and bipolar electrograms effectively before the parameters can be analyzed, they must undergo filtering. Current clinical mapping systems offer a wide range of filter settings:

- High-pass filter: 0.5 (default), 1, 2, 3, 4, 5, 10, 20, 30, 40, 50, 60, 70, 75, 80, 90, 100 Hz
- Low-pass filter: 400 (default), 300, 250, 200, 150, 100, 75, 60, 50, 40, 30, 20, 10 Hz

- Notch filter at 50 Hz: off(default) and on

The signals are commonly zero-phase filtered with IIR Butterworth low- and high-pass filters and/or IIR notch filtered with a quality factor of 30 [24]. The initial filter settings were inspired by a previous study concerning the PhysioHeart™ platform of LifeTec Group B.V. [25]. They utilized a digital Butterworth band-pass filter with cutoff frequencies of 0.5 and 30 Hz for the unipolar signals. The rationale behind these filters was to eliminate the undesirable DC component, baseline wander, and high-frequency, low-amplitude noise. However, the justification for using 30 Hz remains unclear.

In most cases, unipolar signals are filtered with a high-pass filter of around 0.5 Hz and a low-pass filter of 100 Hz or higher. Frequencies higher than 100 Hz are preferred because a low-pass filter with a frequency lower than 100 Hz can significantly increase fractionation delay time and decrease the percentage of detected fibrillation potentials. Adjusting the high-pass and low-pass filter frequencies significantly impacts the unipolar and bipolar electrograms. Filtering out baseline drift and noise may result in under-detection of fractionations and/or low-voltage areas, potential targets for ablation procedures.

The choice of 0.5 to 30 Hz as a bandpass filter by Kappler et al. [25] raises questions about whether this range is sufficient for determining AT, ARI, and conduction velocities for the PhysioHeart™ platform. While the QRS complex and the T complex, which lie within 0.5 to 30 Hz, are of primary interest, it remains uncertain if filtering within this range removes crucial information.

For bipolar signals, the most employed filter ranges are between 30 – 50 Hz and 300 – 500 Hz. Since the previous study on the PhysioHeart™ platform did not include bipolar electrogram measurements, a new frequency range needed to be established.

Choosing a 20 Hz high-pass filter was aimed at facilitating the calculation of the ARI interval. However, even with this setting, the T-complex remains barely visible. Further reduction of the frequency is not advisable for bipolar signals, as higher frequencies are more relevant in this context.

If the study's primary focus involves determining AT, a filtering range of 20 – 50 Hz appears adequate. However, if the study aims to examine activation amplitude, a wider range of 20 –100 Hz may be necessary. Given the primary interest in AT, opting for a narrower frequency range offers the advantage of reduced computational time without compromising measurement accuracy.

2.2 Mechanical activation

Next to electrophysiology, is mechanical activation equally important. By measuring mechanical activation parameters such as ventricular ejection fraction, stroke volume, cardiac output, and pressure-volume loops, valuable insights into the ability of the heart to pump blood can be obtained.

2.2.1 Pressure-volume loops

Pressure-volume (PV) loops show the relationship between the left ventricular pressure and volume during a cardiac cycle [3]; see Figure 12. In phase A, the mitral valve initially open up and the blood that was stored in the atrium will flow into the ventricles due to the pressure difference between the atrium and the ventricle; after the atrium contracts at the end of the diastole, the mitral valve will close and the ventricle will contract with all the valves closed, phase B, this will increase the pressure in the ventricles, while the volume remains the same. When the pressure inside the ventricles exceeds that in the arteries, the aortic and pulmonary valves open, allowing blood to eject from the ventricles in the

systemic and pulmonary circulation, phase C. The valves will close as the pressure within the ventricles decreases to below the pressures in the arteries. As the heart valves are closed and the ventricles start to relax with an unchanging volume, the pressure inside the ventricles will decrease, phase D. As ventricular pressure decreases below atrial pressure, the mitral valve begins to open, allowing blood to flow into the atrium. Towards the end of diastole, atrial contraction ejects the remaining blood, completing the cycle.

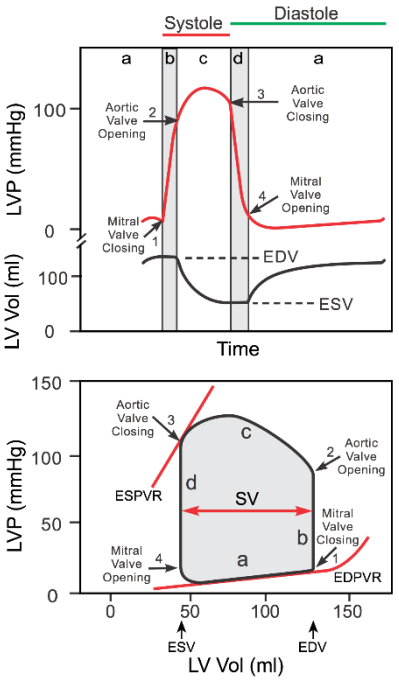

Figure 12: PV loop and cardiac cycle [3].

2.2.2 Stoke Volume and Cardiac Output

From PV loops, multiple parameters can be measured, such as stroke volume (SV), cardiac output (CO), ejection fraction (EF), dP/dt_{min}, and dP/dt_{max} [3][26]. Measures of ventricular function are also available within the PV loops themselves. The maximum pressure in the left ventricle at any volume is described by the end-systolic pressure-volume relationship (ESPVR). This slope represents end-systolic elastance, which indicates how strong the heart muscle is contracting. When the heart contracts more strongly, the ESPVR slope becomes steeper and shifts to the left. If the heart's contractility decreases, the ESPVR slope becomes flatter and shifts to the right.

Another example is the end-diastolic pressure-volume relationship (EDPVR), which shows how the ventricle fills with blood when it's relaxed. It reflects the heart muscle's passive properties, and the slope of this curve indicates how stiff the ventricle is. If the slope is steeper, ventricular compliance is decreased, meaning the ventricle is stiffer. Conversely, if the EDPVR slope is flatter, ventricular compliance increases, indicating that the ventricle is less stiff.

These relationships and parameters provide critical insights into the functional state of the heart and are useful for diagnosing and monitoring cardiac conditions.

2.3 The effects of ion imbalances on the electrophysiology and mechanical activation

As mentioned in chapters 1, 2.1, and 9.1 in the appendix, the primary ions that play a role in the heart's intrinsic cardiac conduction system are sodium, calcium, potassium, and less-known magnesium. From which it is assumed that an imbalance will cause the electrophysiology as well as the mechanical activation patterns to be altered. Magnesium is a less commonly discussed ion that has a crucial role in maintaining a proper heart function. Magnesium modulates the conductance of potassium and calcium channels, affecting the duration of the action potential and cardiac excitability. It also serves as a cofactor for several enzymes involved in energy metabolism, including ATP synthesis, which is essential for heart muscle contraction. Adequate magnesium levels are necessary for cellular energy production, electrolyte balance maintenance, and vascular function, all of which indirectly impact cardiac function. Imbalances in magnesium levels can lead to arrhythmias and other cardiac abnormalities.

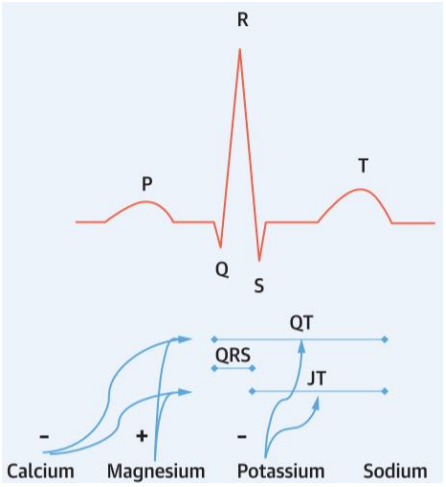

Figure 13: Main finding on how calcium, magnesium and potassium influence the ventricular repolarization phase [27].

As mentioned, maintaining proper ion concentrations is crucial for regulating the electrophysiology and mechanical activation of the heart within physiological boundaries, thus preventing cardiac arrhythmias and other impairments in cardiac function. Noordam et al. [27] investigated the impact of calcium, magnesium, and potassium levels on ventricular repolarization in a study involving a broad cross-section of individuals. The research aimed to uncover correlations between serum electrolyte concentrations and alterations in cardiac electrophysiology within the general population. Data was collected from a large group of individuals, and the relationship between electrolyte concentrations and electrocardiographic intervals was examined.

The findings revealed several significant associations see Figure 13. Lower calcium levels were linked to longer QT intervals and JT duration, while higher magnesium levels correlated with prolonged QT intervals and JT duration. Additionally, decreased potassium levels were associated with longer QT intervals, JT, QRS, and PR durations. Interestingly, with respect to the sodium or RR intervals no physiologically relevant connection was observed.

It is anticipated that if these results are present within a large group of individuals, similar trends would be observed in an ex vivo heart. While the results might not be identical due to differences between human and porcine hearts, the overall trend is expected to be similar. If these similar trends are found in the ex vivo heart, it would open possibilities for maintaining ion balance in other ways than by measuring blood levels. During the measurements of the electrical signal, if smaller or larger QT complexes occur or other changes within the heart rhythm are observed, it would be possible to identify specific ions that can restore the heart to its original rhythm.

Additionally, to the electrophysiology, the effect of the ion imbalance on the mechanical activation are as follows, see also Table 1 for a complete overview of the different effects. According to Drop et al. [28], the effect of calcium on the heart varies depending on the initial levels of ionized calcium. When initial calcium levels are low (hypocalcemia) and return to normal, the mean arterial pressure (MAP), CO, and SV are significantly increased without a change in HR. This indicates enhanced cardiac performance due to increased myocardial contractility and blood flow. In cases of excessive calcium (hypercalcemia), vascular resistance is mainly increased without enhancing CO. Regarding the PV loops, transitioning from hypo to normal calcium levels results in a larger loop that shifts leftward and slightly upward, indicating improved contractility and SV. When transitioning from normal to hypercalcemia, the expectation is that the PV loops remain similar to their original shape, but potentially shifts slightly further upwards.

[29] In the case of magnesium, this ion mainly influences the cardiac conduction pathways and interactions by altering the inflow and outflow of other ions. Magnesium acts, for example, as a calcium antagonist, regulating the influx of calcium into cardiac cells through L-type calcium channels. This regulation helps decrease myocardial oxygen consumption by reducing HR and contractility and protects the cells from calcium overload. Additionally, magnesium interacts with potassium channels, helping to stabilize cell membrane potentials, which is essential for maintaining proper cardiac function. By preventing calcium overload, magnesium can stabilize cardiac contractility. If magnesium improves contractility, SV might increase, but excessive magnesium could reduce contractility and decrease SV.

For optimal magnesium levels that stabilize cardiac contractility, the expectation is that the PV loop will shift leftward, slightly upward and wider, indicating improved contractility and SV. When excessive amounts are used the PV loop will shift to the right and downwards and will become narrower.

Table 1: The effects of ion imbalances on the hearts functions and how it alters the shapes of the related PV loops.

	General changes	PV loop changes
Hypocalcemia to normal	↑ contractility ↑ mean arterial pressure ↑ CO ↑ SV -- HR -- CV	• Wider loop • Shift left • Shift upwards
Normal to Hypercalcemia	↑ contractility ↑ vascular resistance ↑ CV -- CO -- SV	• May become wider • Further upwards
Hypomagnesemia to normal	↑ contractility ↑ SV ↑ CO -- normalized CV -- stabilized HR	• Wider loop • Shift left • Shift upwards
Normal to Hypermagnesemia	↓ contractility ↓ SV ↓ CV ↓CO↓HR	• Narrower loop • Shift right • Shift downwards
Mild to moderate hyperkalemia	↑ CV -- SV (mild effect) -- contractility (mild effect) -- CO (mild effect)	• The loop is almost unchanged
Severe hyperkalemia	↓ contractility ↓ SV ↓ CV ↓ CO	• Narrower loop • Shift right • Shift downwards

[30] Potassium is crucial for maintaining the resting membrane potential and proper cardiac excitability. Elevated potassium levels can depolarize the resting membrane potential and promote conduction blocks, reentries, and ventricular fibrillation. In mild to moderate hyperkalemia cases, there may be depolarization of the resting membrane potential as well as faster CV, leading to a slight increase in contractility and a potential leftward shift. In severe hyperkalemia, conduction blocks, reentries, and ventricular fibrillations might occur. The PV loop may exhibit reduced contractility, resulting in a rightward shift and decreased SV. An even higher level of potassium can lead to arrhythmias and alter the general shape of the PV loop.

Examining the effects of ion balance on both electrophysiology and mechanical activation is intriguing. Administering calcium, magnesium, and potassium can significantly affect pressure volume

loops, reflecting alterations in cardiac function. Conducting a study on ion levels while simultaneously measuring mechanical and electrical activations enables a deeper understanding of ion effects and the necessity of adding specific ions during experiments.

3 Methods

3.1 Harvesting procedure and administration of cardioplegia

Dutch Landrace pigs, destined for human consumption, were utilized in all experiments. The protocols followed by both the slaughterhouse and laboratory were in complete adherence to EC Regulations 1069/2009, governing the utilization of animal material from slaughterhouses for diagnostic and research purposes. These protocols underwent rigorous oversight by the Dutch government, specifically the Ministry of Agriculture, Nature and Food Quality, and received approval from relevant legal authorities responsible for animal welfare, including the Food and Consumer Product Safety Authority. These protocols where the same as utilized by Kappler et al [25].

The procedural steps are outlined as follows: The pig undergoes electrical stunning once or twice on the head, followed by hanging and exsanguination, causing death by loss of excessive blood. A veterinarian then conducts a thorough examination, approving the pig if deemed fit. Subsequently, a parasternal incision opens the chest, enabling removal of the heart along with any excess material. The heart undergoes immediate topical cooling, followed by the opening of the pericardial sac and transection of the pulmonary artery beneath the first supra-aortic vessel. The heart is isolated and prepared for aortic cannulation, facilitating the administration of a cardioplegic solution into the coronary arteries at a mean pressure of 80 mmHg. Similar to the experiments done by Kappler et al[25].

Typically, the time from electrical stunning to perfusion initiation remains under 4 minutes. During the heart harvesting process, excess material, such as portions of the lungs, are removed. Approximately 4 to 5 litres of blood from the same pig is collected for experimental use and stored in a vessel at room temperature with no additional treatment.

3.2 Mounting of the pig heart on the PhysioHeart^{TM} platform

The Langendorff blood perfusion system consists of several crucial components as shown in Figure 14. At its core, a pump is responsible for circulating the blood. This blood then passes through an arterial filter featuring Cortiva bioactive surface technology from Medtronic, which helps maintain its quality. Subsequently, the blood enters a Maquet Quadrox-i hollow fiber oxygenator, where it is oxygenated to ensure proper oxygenation before being circulated through the heart.

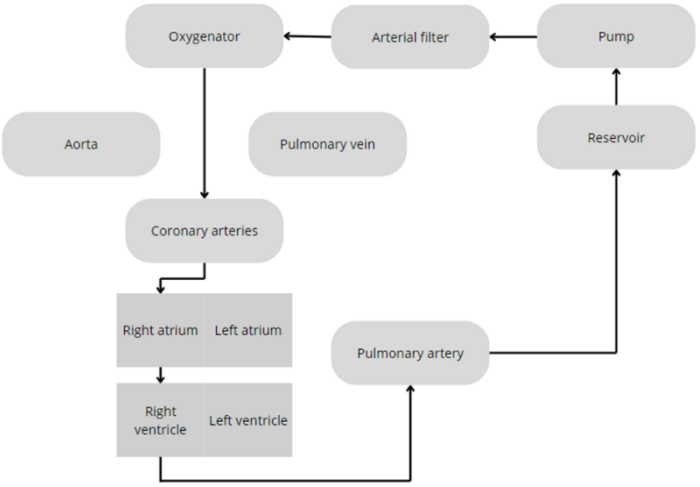

Figure 14: Langendorff perfusion set up.

A line known as the Langendorff line extends from the oxygenator to the starting point of the coronary arteries at the entrance of the aorta, forming a closed-loop system. Within this system, the coronary arteries of the heart are filled with blood, which is maintained at a pressure of approximately 80 mmHg. The blood in the coronary arteries is then emptied through the heart's right atrium, which is drained via the pulmonary vein. In this case, the flow in the pulmonary artery represents the coronary flow.

From the pulmonary artery, the blood returns to the reservoir. Any blood that may have leaked from the heart also flows back to the reservoir. Finally, from the reservoir, the blood returns to the pump, completing the cycle, and the process repeats. This continuous circulation ensures that the heart receives the necessary oxygen and nutrients for experimental procedures.

During Langendorff mode, blood circulates continuously, gradually warming to stabilize the heart over about 45 minutes. Initially, temporary pacing leads are placed in the right ventricle, and later, in the right atrium, to monitor and regulate electrical activity for maintaining a steady rhythm. If required, defibrillation may also be administered.

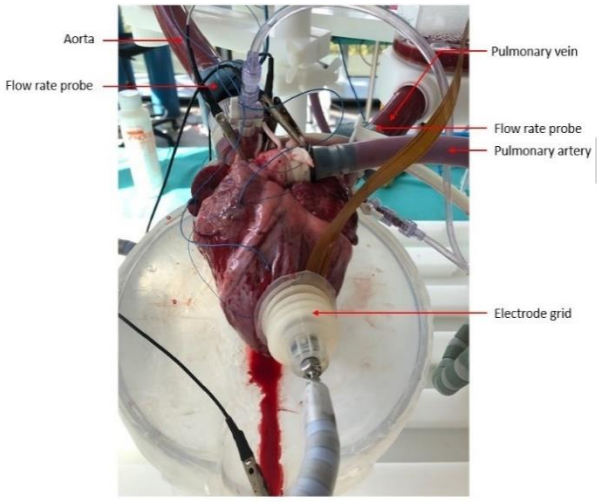

Figure 15: Real porcine heart on the PhysioHeart™ platform in a two-chamber configuration

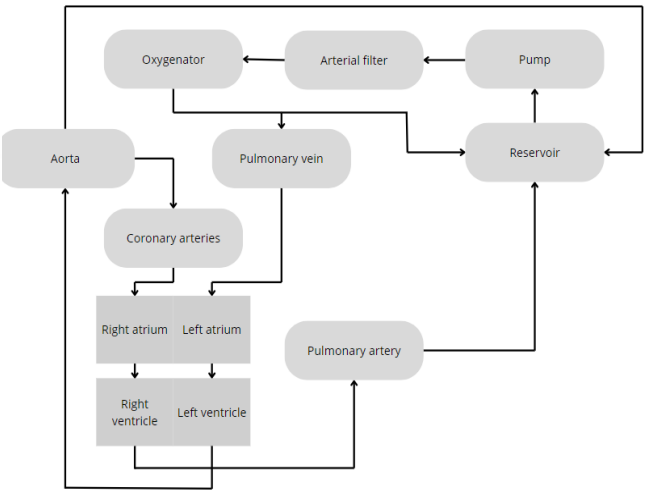

Figure 16: Two-chamber configuration

After approximately 60 minutes, the preload of the pulmonary artery and afterload of the aorta are opened, and the Langendorff line is closed. During this two-chamber working mode seen in Figures 15 and 16, the blood flows from the preload of the pulmonary vein to the left atrium and into the left ventricle. From the left ventricle, the blood flows to the afterload of the aorta, and a portion also enters the coronary arteries. The blood from the aorta returns to the reservoir, while the blood from the coronary arteries flows back into the right atrium and empties into the pulmonary artery and then into the reservoir. Throughout the process, all pressures and flows are monitored and kept within the physiological range.

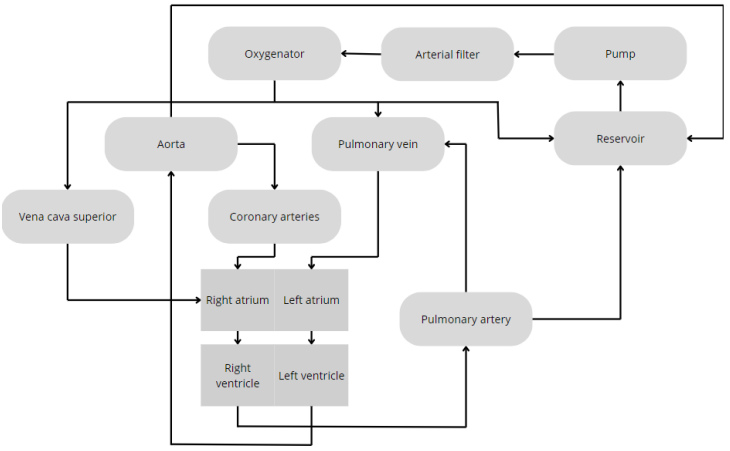

Figure 17: four-chamber configuration.

In case of the four-chamber configuration seen in Figure 17 the first hour is the same as for the two-chamber configuration. First the heart is started up in the Langendorff mode. Once the first hour is completed the two-chamber mode will be started and after approximately 30 minutes the configuration is changed to the four-chamber configuration, first with an open loop and if the heart allows it can be changed to a closed loop configuration. To go from the two-chamber to four-chamber configuration the pre-load of the superior vena cava will be opened as well as a larger after-load of the pulmonary artery,

to create a closed loop the blood should be able to flow from the pulmonary artery toward the pre-load of the pulmonary vein. This can however lead to high pressures and therefore this connection is first kept closed and slowly opened depending on the amount of pressure and flow the heart can take. The loop on the left side of the heart is overall kept the same as in the two-chamber configuration, with an added connection coming from the pulmonary artery.

3.3 Blood analysis and control

Arterial blood samples were extracted from the oxygenator. The baseline measurement was taken before the heart was attached to the platform, and subsequently, measurements were performed approximately every half hour. To conduct these measurements, an ABAXIS VetScan i-STAT was utilized to measure blood gas values and electrolytes. Based on these measurements, efforts were made to maintain physiological levels of pH, glucose, ionized calcium, and potassium by administering glucose, calcium chloride, potassium, sodium bicarbonate, and/or magnesium sulfate, as necessary. Also, from these measurements the boluses were determined for the study regarding the balancing of the ion levels.

3.4 Sensor placement and data acquisition

3.4.1 Electrode grid placement

For the infusion experiment involving calcium, magnesium, and potassium, various regions of the heart are relevant for the electrode grid placement. Particularly sensitive regions include the conduction system, the AV and SA nodes, and the myocardial cells throughout the atria and ventricles. Changes in ion levels can significantly impact the excitation-contraction coupling process and alter the duration and strength of the cardiac action potential, observable in both the atria and ventricles. Given the accessibility and frequent usage of the left ventricle in experimental setups, it serves as an optimal location for electrode grid placement. While the left ventricle is commonly utilized in studies due to its prominent role in cardiac function, it also allows for consistent comparisons across experiments, enhancing the reliability of results.

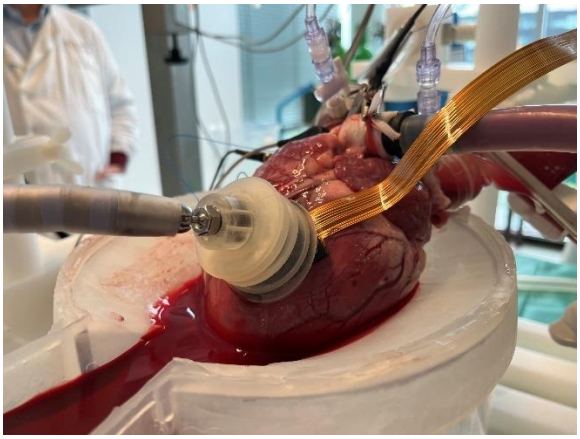

Figure 18: Side view from the right of the PhysioHeart™ platform and structure holding the electrode grid in place.

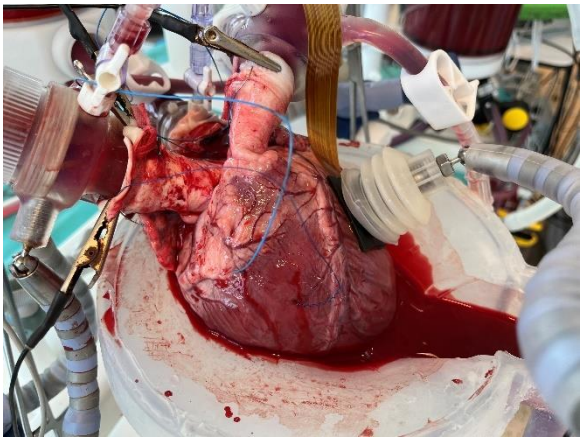

Figure 19: Side view from the left of the PhysioHeart™ platform and structure holding the electrode grid in place.

To secure the electrode grid in place, a suction cup holder with a slightly curved silicon pad underneath was employed see Figures 18 and 19. This holder ensured stability and flexibility, allowing the grid to move with the heart's motion. Compared to previous methods involving manual placement, the suction cup holder minimizes variability between measurements and reduces the risk of excessive

pressure on the heart. Even if the setup is positioned closely to the heart, it mitigates the undesirable effects of grid pressure on cardiac function.

3.4.2 Data acquisition

For the study, multiple comparisons are necessary between configurations, different methods of recording electrograms, variations in mechanical and electrical activation, and the impact of ion levels on both mechanical and electrical activity. Each of these aspects requires different approaches to data acquisition. To demonstrate the deterioration of cardiac function over time across various configurations and recording methods, multiple measurements are required in a stable environment.

Initially, the plan was to measure electrograms every 30 minutes for approximately 2 to 3 hours, followed by additional studies on ion levels and other methods to validate expected activation patterns. However, after conducting several pilot experiments, it became evident that more frequent measurements would be beneficial for detecting subtle changes over time. Therefore, the decision was made to measure electrograms every 15 minutes, provided that the heart remained stable at those intervals. Additionally, more frequent measurements were taken when anomalies occurred. As a 3-hour time period proved too lengthy to conduct ion level measurements, pacing, and scarring on the heart, a 1-hour interval was chosen instead. During this time, the heart has to remain stable with no alterations to additional parameters, allowing for the observation of any changes in cardiac function over time.

Throughout all measurements, both unipolar and bipolar electrograms were acquired, as detailed in the following section. Initially, mechanical activation was assessed using a pressure-volume catheter, which was later replaced by flow probes. Initially, the flow probes were only utilized during boluses, but their use extended throughout the entire experiment as it progressed.

The final protocol for data acquisition involved measuring unipolar and bipolar electrograms, coronary, pulmonary vein, and aortic flow rates, and left ventricular pressure for at least 1 minute at various intervals:

- Twice during Langendorff.
- Five times during the first working hour (immediately after change and every 15 minutes).
- Whenever pacing from the grid was performed (preferably at least twice, for comparison).
- During every bolus (for 3 minutes instead of 1 minute).
- Just before and after scarring the heart.

Unipolar and bipolar data acquisition

Simultaneous recording of unipolar and bipolar signals was performed from all electrodes using a National Instruments (NI) 6031E acquisition card at a sampling rate of 1000 Hz. With this acquisition card, it was possible to measure both the single-ended-ground and differential referenced signals, referred to in our study as unipolar and bipolar signals, respectively. Each channel pair can be defined as AI < i, i+8 > (i = 0...7,16...23,32...39,48...55) and they can be configured either as one differential input or two single-ended inputs. This means that there are a limited number of bipolar channels, namely 24 inputs, which is half of the amount of unipolar inputs that can be measured. Meaning that during data processing less points on the grid are available for the bipolar signals then for the unipolar

signals on the grid. The acquisition card was connected to the electrode grid through an NI SCB-100 shielded connector block followed by an NI-SH100100 connector block, replicating the setup employed by Kappler and Ledezma et al. Signal configuration and recording were conducted using a customized virtual instrument developed in NI LabVIEW, adapted to facilitate the recording of bipolar signals.

In Figure 20 a schematic of the electrode grid and its bipolar pairs is depicted. As previously mentioned, due to limitations of the current acquisition card, only 24 bipolar signals can be measured from the 48 electrodes. The current setup is designed to measure only the horizontal bipolar signals. While it is possible to measure the vertical bipolar signals instead of the horizontal ones, this would require adjusting all the wires within the shielded connector block. Another approach to acquiring the bipolar signals is by calculating them.

In our case, we only have a usable electrode grid with an inter-electrode spacing of 4 mm. To create a finer activation map than the 24 bipolar channels allow, it should be possible to calculate the bipolar signals. However, a quantitative comparison between the measured and calculated bipolar signals should be conducted first. If the correlation coefficient is sufficiently high, it would be feasible to generate a more detailed activation map than with just 24 points in the horizontal and/or vertical direction.

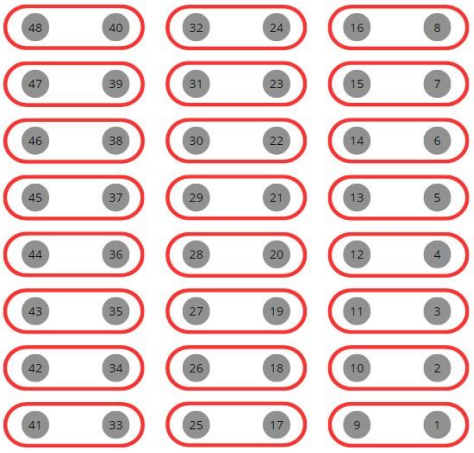

Figure 20: A representation of the electrode grid and its bipolar signal pairs. The measurement of electrode 1 = AI0, electrode 2 = AI1, etc..

Figure 21: Electrode grid with inter-electrode spacing of 4 mm.

Flow rates and pressure data acquisition

For the mechanical activation multiple parameters are measured. The flow rates through certain arteries and veins and the pressures from multiple arteries and veins as well as the left ventricle. For the flow rates the COnfidence flowprobes from transonic are used as well as clamp on tranducers from em-tec. For the flowrates measurement of the aorta and pulmonary vein a transonic perivascular flow model TS420 is used, for the inflow in the right atrium (only applicable in the four-chamber configuration) a HFM-10-1 is used and for the pulmonary artery/coronary flow (in case of the two-chamber experiments) and the aorta a LFM-10-1 is used. In Figure 15 two flow rate probes are shown. The inflow probe is placed on the pulmonary vein, just before the left atrium and the outflow probe is placed on the Aorta. To be able to compensate for the blood flow that goes through the coronaries the pulmonary artery was also cannulated to return the blood to the reservoir and the flow rate was measured. In case of a two-chamber heart perfusion the blood flow through the pulmonary artery should be equal to the coronary flow. To find the volume that goes through the heart the coronary flow rate is added to the flow rate in the aorta. This is done such that the inflow from the pulmonary vein

should match the outflow from the aorta and coronary arteries combined. One problem that remains is that it will still contain the compliance of the atrium, which is hard to remove.

The pressure catheter is positioned in the left ventricle through the pre-load, the pulmonary vein and the left atrium and measured at the same time as the flow rates and the electrical signals. The measurement equipment used to measure the pressure, so not only the left ventricle pressure, but also the left and right atrial pressure, Aortic pressure, and pulmonary pressure, is a Peekel instruments multichannel compact amplifier system PICA wit BP transducers. Depending on the configuration, 2 or four-chamber, all or some pressure sensors will be used.

All outputs of the flow rate modules and the pressure sensor modules come together in a national instruments acquisition box BNC-2090A. The signal configuration and recording were conducted using a customized virtual instrument developed in NI LabView.

3.5 Data processing

3.5.1 Pre-processing

Unipolar electrogram filtering

After the data acquisition the first step in the data processing is to filter the recorded electrograms from the electrode grid. The type of filters that are used are a 4th order butterworth filter, which is a type of filter that is often used within electrophysiology studies according to the literature study. At first a high-pass filter is used and afterwards a low-pass butterworth filter with specific frequencies. As mentioned in the introduction the current clinical mapping systems use a large variety of filter settings. From the literature study it remained unclear if Kappler er al was using an appropriate bandpass filter or, if too much information is lost when using a filter from 0.5 to 30 Hz. Therefore, it was decided to test multiple filtering ranges to either prove that this filter setting is sufficient or that a larger range should be suggested.

As the literature study suggests that using a low-pass filter higher than 100 Hz as using lower frequencies can significantly increase the fractionation delay time and decrease the percentage of detected fibrillation potentials and thus making the signals less accurate. It was decided to compare the filtering ranges from 0.5 to 100 Hz and from 0.5 to 30 Hz. As the main frequency spectrum of interest lies between 0.5 to 30 Hz. In the last case the low-pass filter will use a frequency of 30 Hz and the high-pass filter 0.5 Hz.

Bipolar electrogram filtering

For the bipolar electrogram, also a 4th order low and high pass butterworth filter was used. As mentioned in the introduction lies an appropriate filter for the bipolar electrograms between 30 – 50 Hz for the high-pass filter and 300 – 500 Hz for the low-pass filter, but as mentioned this study would like to test if an accurate AR can be found and because of that the high-pass filtered should be lowered to 20 Hz. Lower than this value is not advised as higher frequencies are more relevant in the case of bipolar electrograms. In this study the ranges that where tested and compared to the original electrogram are between 20 – 50 Hz and 20 – 100 Hz.

Calculated bipolar electrograms filtering

For the calculated bipolar electrograms the filtered unipolar electrograms are used. After the unipolar electrograms are subtracted from each other the resulting bipolar electrograms are filtered again using the same filter as the measured bipolar signals, such that they contain the same frequency spectra. The filtered measured and calculated bipolar electrograms are then compared to each other.

3.5.2 Activation and recovery times

Activation times

To determine the AT and RT, a moving average (MA) method was employed, similar to the approach by Aziz et al. [31]. This method helps identify the region where the activation occurs, allowing the pinpointing of the AT or RT within this area. For detecting the AT within the QRS complex, which typically lasts approximately 80 to 100 ms, two MA were used: one based on individual heartbeats (event) and the other on heartbeats over multiple cycles (cycle). A 100 ms window was used for the event, while the cycle window depended on the HR. Given that HR vary, the cycle window was either adjusted according to the HR or maintained at a size that accommodates multiple HR ranges. While smaller event windows might be preferable for certain arrhythmias, a slightly larger window generally suffices for normal cases. In the experiments, HR were primarily maintained between 80 to 115 bpm through pacing or naturally, depending on the heart's intrinsic rhythm. Within this range, a window of at least 1000 ms seemed suitable. If proven insufficient, the window would be adjusted based on the HR.

$$\mathrm{MA}_{\mathrm{event}}(n) = \frac{1}{W}\sum_{k=-l}^{l} x(n+k) \quad (1)$$

Here W represents the duration/window of the event, in case of the QRS complex W is 100 ms and in case of the heart rhythm this s 1000 ms.

For the UEG, the differential signal was used rather than the standard electrograms as input (x) for the MA. This differential signal was squared to amplify the peak values. Despite these modifications, the maximum change in frequency still occurs at the QRS complex. To further enhance peak detection accuracy, the Fractional Fourier Transform (FrFT) was applied, which rotates the signal in a time-frequency plane. The degree of rotation can either push the signal towards the frequency domain (with higher values) or towards the time domain (with lower values). Starting with a value of 0.01, as used by Aziz et al. [31], the FrFT was applied to the signal. After FrFT, the signal was squared again to boost the peaks before using it as input for the MA.

The FrFt of the signal is defined as follows [31]:

$$FrFT^{\phi}(t,u) = F^{\alpha}\big(x(t)\big) = X_{\phi}(u) = \int_{-\infty}^{\infty} x(t)K_{\phi}(t,u)dt \quad (2)$$

Here $\propto$ is the order of the FrFt and $\phi = \frac{\sigma\pi}{2}$ is the angle of rotation. $F^{\alpha}\big(x(t)\big)$ denotes the FrFt operator and $K_{\phi}(t,u)$ the kernel of FrFT and is defined as:

$$K_{\phi}(t,u) = \begin{cases} \sqrt{\dfrac{1-j\cot\phi}{2\pi}}\exp\left(j\dfrac{t^2+u^2}{2}\cot\phi - jtu\csc\phi\right), \phi \neq n\pi \\ \delta(\mathrm{t}-\mathrm{u}), \text{for } \phi = 2n\pi \\ \delta(\mathrm{t}+\mathrm{u}), \text{for } \phi = 2\left(n+\dfrac{1}{2}\right)\pi, \end{cases} \quad (3)$$

To identify the activation area, the two MA were overlaid, and a one was assigned to an array whenever the QRS complex MA exceeded the HR MA; otherwise, a zero was assigned. The resulting plot, consisting of zeros and ones, highlights the activation regions. An example of this plot is shown in Figure 22, where the regions of interest are depicted in red for UEG, and the UEG is shown in dark blue. Within the non-zero regions, AT were identified as the steepest negative slopes, equivalent to the negative peaks in the differential of the UEG.

In case of the BEG the principle is the exact same, but the BEG are already similar in shape and frequency spectrum to the differential of the UEG. Therefore, the input of the MA is made using the BEG itself, which will be squared, fractional Fourier transformed and squared again. For the FrFt the same value is used.

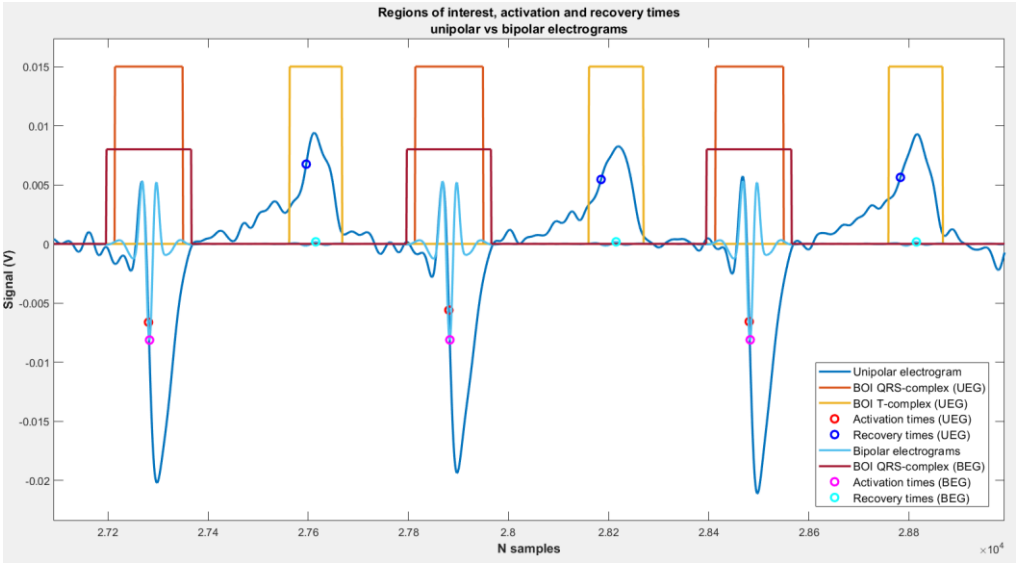

Figure 22: Block of interest for QRS complex shown in red and dark red. Block of interest of the T-complex shown in yellow. The resulting AT (red and pink dots) and the RT (blue and light blue dots). These results are established from a UEG and BEG from electrode 7 and 15 on the electrode grid during experiment 5.

Recovery times

To determine the RT, a MA method was also employed [31]. However, in this case, the input has already been modified from the original UEG differential or BEG. From both the UEG differential and BEG, the R-peak is removed. This is achieved by utilizing the previously identified R-peaks and eliminating everything 0.083 seconds before the peak and 0.166 seconds after the R-peak. In this removed region, there is almost a zero percent chance that the P and T waves will occur. Once this segment is deleted from the signals, the signal is squared to enhance the peaks. Additionally, the signal is subjected to fractional Fourier transformation (FrFT) and then squared again. The value used in the FrFT is 0.01, consistent with the FrFT used to identify the activation regions.

The widths of the MA are based on the P-wave duration and the QT interval, approximately 80 and 400 ms, respectively. Similar to the other MA, these two are overlapped, and when the MA of the P-wave exceeds that of the QT interval, a value of one is assigned. The resulting blocks of interest will encompass both the P-wave and the T-wave. However, there will be a significant difference in the width of these blocks of interest, allowing for the distinction between the different waves.

As a second option, or simultaneously, the location with respect to the R-peak or AT can also be utilized to determine whether the block can be considered the T-wave or the P-wave. In our case, both

methods are employed for more accurate results. The T-wave's location must be directly after a detected AT and within a certain number of samples, and the width of the block of interest must exceed 70 samples.

Within Figure 22 the regions of interest for the AT and RT are shown. In the block of interest for the RT the P-wave blocks have been deleted, such that only the blocks that include the RT are included, shown in yellow. Within this Figure the normal unipolar electrograms are shown. The RT can be found as the steepest positive slope in the T-wave region, which is equivalent to the maximum peak in the T-wave region in the differential of the unipolar electrogram.

As mentioned in Chapter 2.1.7, the filtering range for bipolar electrograms mainly targets higher frequencies. However, since the T-wave lacks high frequency components, it becomes challenging to detect in bipolar signals with a high-pass filtering frequency higher than 20 Hz. Lowering the high-pass filter frequency is not viable due to the risk of increased baseline fluctuations and noise levels. Consequently, detecting RT in bipolar electrograms seems unfeasible under these constraints.

For AT, the same method employed in unipolar electrograms was used: a MA approach. However, for RT detection, this method was not applicable. Instead, a windowing method was adopted. A window ranging from 100 ms to 370 ms after the AT was utilized, within which the T-wave is expected to occur. The RT was then determined as the maximum peak within this window.

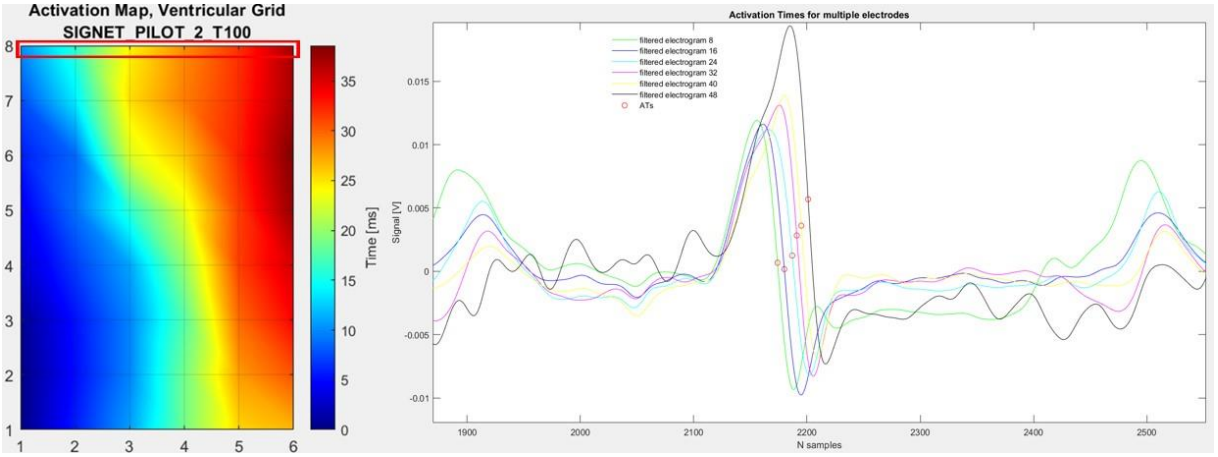

Figure 23: Example of an activation map and unipolar electrograms with AT represented as the red dots. In the activation map the red bar represents the AT from the unipolar electrograms to the right.

Activation map

From all the identified activation timestamps, it becomes possible to determine their relationship with respect to each other. On the right side of Figure 23, multiple electrograms are displayed for different electrodes. The electrodes used are represented within the red bar in the activation map. Within the unipolar electrograms, it's noticeable that all the AT occur at different moments in time or at different samples. By selecting one electrode as a reference, it's possible to discern how all the AT are related to each other. For example, within the displayed electrograms, all AT occur successively, resulting in a wave propagation from the left to the right within the red bar, which accurately reflects what is depicted in the graph on the right of Figure 23. By conducting this analysis across multiple heartbeats and across the entire electrode grid, an average activation map can be generated. This map illustrates how the electrical wave propagates across the electrode grid and reveals any inconsistencies in AT.

On the left side of Figure 23, an example of such an activation map is presented. In this map, it's evident that the wave propagates from the bottom left to the top right. The onset of the wave is depicted in blue, while the termination of the wave that remains within the grid boundaries is shown in red. As the electrode grid only represents a small area of the heart, it's not possible to directly compare it to a full wave propagating across the heart. However, it is possible to understand how the electrical wave moves across the electrode grid and whether it is moving in a proper direction with respect to the physiology of the heart.

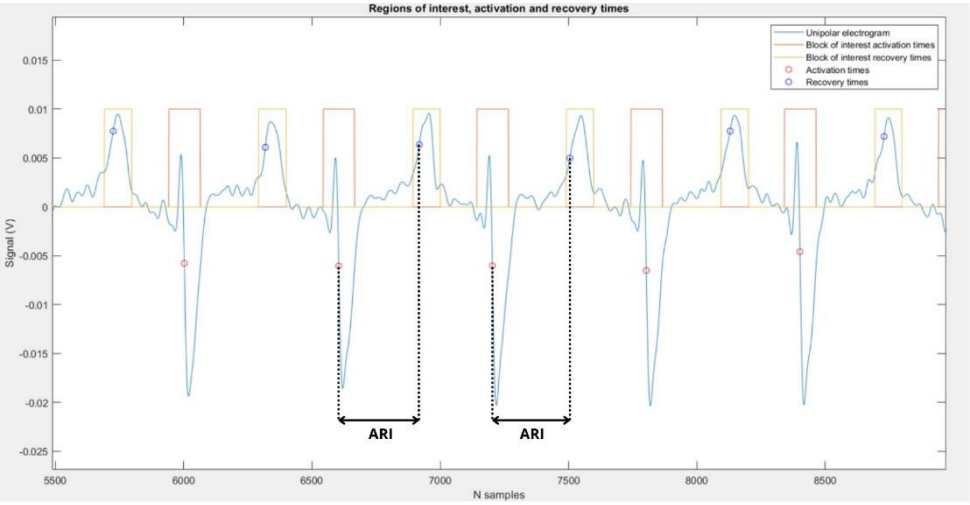

Figure 24: Identification of ARI from the activation and RT

3.5.3 Activation Recovery Interval (ARI)

The ARI is derived by determining the duration between the activation and RT. Subtracting the AT from the RT yields the ARI, see Figure 24. During normal operation, the objective is to discern if the ARI fluctuates over time. Various methods can be employed to obtain an appropriate value for comparing different timestamps. One approach involves plotting all ARIs per beat and per electrode in a histogram. Alternatively, ARIs can be analyzed per beat or per electrode, though this may significantly reduce the number of data points. Thus, generating a histogram of all ARIs per timestamp is often the preferred option. From this histogram, the ARI mode—the ARI most frequently represented within the measurement—can be identified. To further explore the range of ARIs, investigating the standard deviation of the mode is advisable. Conducting this analysis for all timestamps facilitates easier comparisons between timestamps and experiments.

Another method to analyze ARIs per timestamp involves creating an ARI map, which depicts the mean value of each electrode during a given measurement or timestamp. These maps offer valuable insights into the spatiotemporal distribution of cardiac repolarization. ARI maps are particularly useful for detecting subtle changes in repolarization patterns, aiding in the identification of arrhythmia risks.

Moreover, ARI maps facilitate the identification of regions exhibiting delayed or heterogeneous repolarization. This information is instrumental in pinpointing specific areas for catheter ablation, a critical aspect of electrophysiological studies and ablation procedures. Overall, ARI maps serve as powerful tools for investigating cardiac electrophysiology and guiding therapeutic interventions in the management of arrhythmias.

3.5.4 Conduction Velocity (CV)

To calculate the conduction, an inverse gradient method was employed [32][15]. On the left of Figure 25, an example grid containing 9 electrodes is depicted. Gradients of activation are computed along the dotted lines in both horizontal and vertical directions, which are then utilized to determine the CV in the direction of activation, as shown in equations 4 and 5. The middle of Figure 24 illustrates a contour plot of an activation map, where arrows indicate the directional component of the gradients. The gradient of horizontal component G_x and the vertical direction G_y, together they can be translated to the directional component of the gradient G_A, equation 4. However, this directional gradient has the units $\frac{s}{m}$ and therefore the inverse of the absolute value of the gradient should be taken to find the CV, equation 5.

$$G_A = \sqrt{G_x^2 + G_y^2} \tag{4}$$

$$|u| = \frac{1}{|G_A|} \tag{5}$$

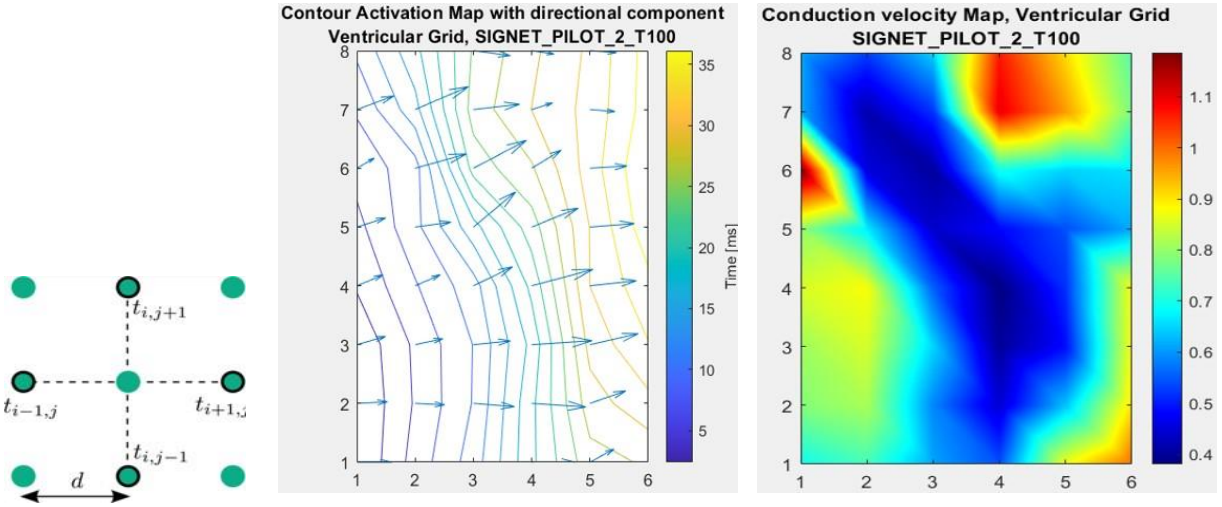

Figure 25: Left, a visualization of the finite difference technique. All separate dots represent the different electrodes that each has their own value for the AT [29]. Middle, a contour plot of an activation map as shown in Figure 23, with the arrows indicating the directionality of the gradients in units s/m. Right, a CV plot that is rendered from the inverse of the directional gradient.

By performing this process for all electrodes on the grid, it becomes feasible not only to provide the mean value of CV over the electrode grid but also to generate a CV map, see the right side of Figure 25. To mitigate localized noise in AT and achieve a smoother CV map, a 2D Gaussian smoother operator was applied.

The resulting map serves to identify unusual CV or if CV fall within the physiological range for porcine hearts, which is expected to be similar to the range observed in human hearts (0.3–1.0 m/s).

3.5.5 Pressure-volume loops

To create PV loops of the two-chamber configuration, measurements from multiple flow probes/sensors are utilized, along with a pressure sensor pigtail catheter placed in the left ventricle. In the case of the two-chamber configuration, the flow rate sensors on the pulmonary artery equate to

the coronary flow rate, as blood flows from the left ventricle into the aorta and the coronary artery. Hence, the coronary flow and the aortic flow rate should be summed to match the amount of blood flowing into the heart from the pulmonary vein.

By integrating the inflow (pulmonary artery) and outflow (aortic flow plus coronary flow) rates over time, the volume flowing along the flow probes/sensors can be determined. By subtracting the outflow from the inflow, the volume change withing the left ventricle can be calculated. The baseline wander was removed by filtering the volume change using a 0.5 Hz butterworth high-pass filter. Resulting in PV loops as depicted in Figure 26, the blue lines. By now finding the repetitions an average PV loop can be created, the red line, which will be used to compare all the measurements with each other.

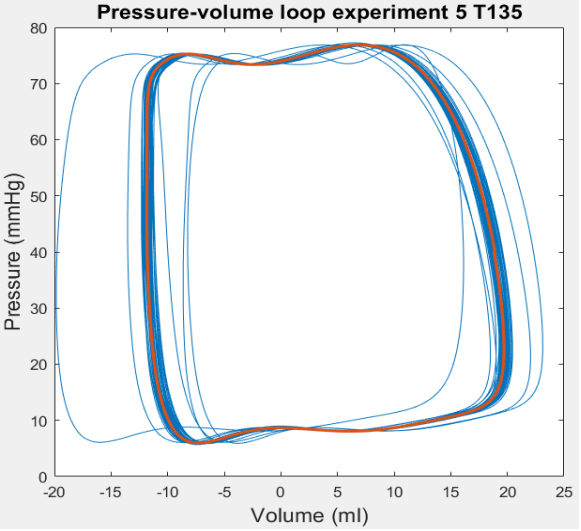

Figure 26: PV loop after baseline removal. The blue lines mark the loops from the whole data set and the red line, marks the average PV loop.

In case of the 4-chamber configuration the coronary flow cannot be measured as being the same as the pulmonary artery flow alone. The flow on the superior vena cava has to be measured as well and should be subtracted from the flow of the pulmonary artery to get an estimation of the coronary flow. The next steps of calculating the volume flowing into and out of the left ventricle are the same as in the 2-chamber configuration.

4 Introductory results

4.1 Unipolar electrogram filter settings

Within Figure 27, the resulting unipolar electrograms (UEG) can be seen. As mentioned earlier the main frequency spectrum of interest lies between 0.5 to 30 Hz, but it is questionable when using a filter with this range if it filters away too much information. Within Figure 27 the dots in red and blue represent the AT, it is visible that there are some differences in the time stamps of activation between different filtering settings, but it is not significant. Also, in case of using the range from 0.5 to 100 Hz, it sometimes registers the pacing spike as the steepest negative slope and therefore does not find the correct AT. For the RT, also a better estimation is made when using a smaller range as within the larger range there is a lot of noise within the T-complex, which would make it more difficult to find the maximum slope. The main interest of this study is to find the AT, ARI, and the CV, therefore, a filtering range of 0.5 to 30 Hz is chosen.

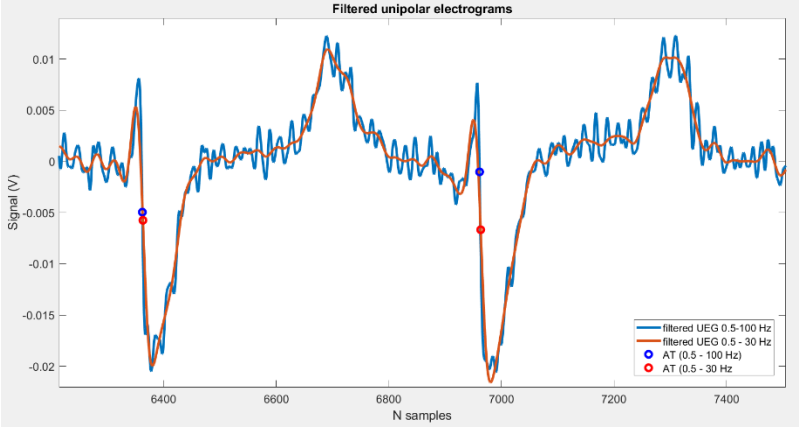

Figure 27: Filtered UEG from electrode 6 on the electrode grid.

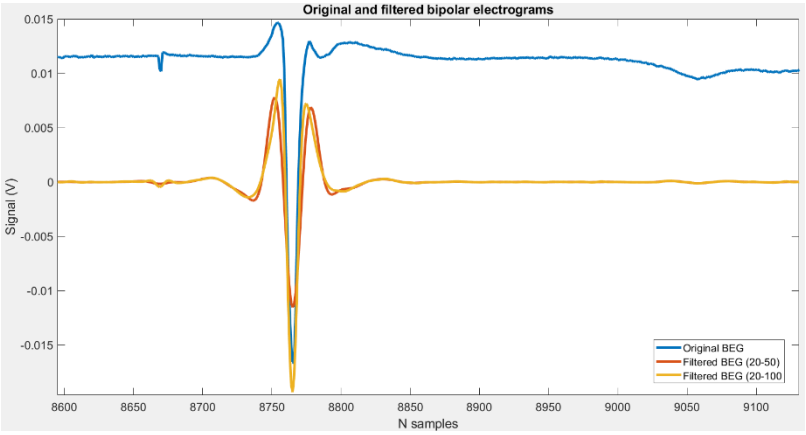

Figure 28: The original and filtered BEG from electrodes 6 and 14 on the electrode grid.

4.2 Bipolar electrogram filter settings

In this scenario, the primary interest lies in the AT. Consequently, we choose a narrower frequency range due to its advantage of reduced computational time, which is particularly beneficial given the extensive volume of data requiring processing. This streamlined approach does not compromise the accuracy of AT measurements.

Within Figure 28, the resulting filtered bipolar electrograms (BEG) can be viewed. The AT in these graphs can be seen at the minimum peak, and for all graphs shown, these AT are exactly at the same

spot. The main differences are that the original electrogram has an offset with respect to the zero-line, and the steepness of the QRS complex is larger. Additionally, the amplitudes of the electrograms filtered between 20 to 50 Hz are much smaller. This aligns with expectations, as a larger frequency range can more accurately measure abnormalities within cardiac function. However, since the difference between both settings is minimal, we opted for the narrower range to enhance efficiency without significant loss of quality.

4.3 Calculated Bipolar electrograms

To increase the number of data points for the BEG data processing, calculated BEG were used. According to the performed literature study, no comparison between measured and calculated BEG has been performed for an inter-electrode spacing of 4 mm, only for inter-electrode spacings of 2 mm. The correlation factor for the 2 mm spacing between measured and calculated BEG was approximately 0.9 for 90% of all the measurements.

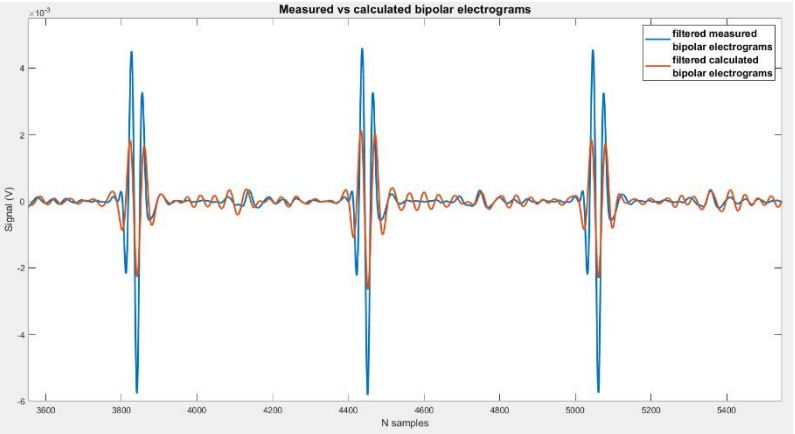

Figure 29: Filtered measured and calculated BEG.

In Figure 29, the difference is shown between the filtered measured and filtered BEG. It can be seen that the amplitudes during the QRS complex are much lower for the calculated electrograms, and there is some extra noise between the activations. However, the overall trend of the activations is similar. For this specific activation, the correlation is 0.8, but many other comparisons between measured and calculated electrograms are less accurate.

The correlation factors for all electrodes during different experiments in working mode, during grid pacing, and during the boluses were determined and are shown in Tables 1 and 2. These tables present the percentage of occurrence of different correlation factors. During the 2-chamber configuration (Table 1), the highest correlation factors are observed in most cases, with approximately 80% of all measurements having a correlation factor higher than 0.6. In the 4-chamber configuration (Table 2), the highest correlation factors are also common, with approximately 90% of all measurements having a correlation factor higher than 0.6. For measurements where grid pacing was utilized, the correlation between the measured and calculated BEG worsened in the 2-chamber configuration but remained relatively high in the 4-chamber configuration.

From these measurements, it seems like the correlation between measured and calculated electrograms improves with the 4-chamber configuration, but it is still not as high as the results from Blanchard et al. [23]. As no smaller grid was available for this study, it was not possible to compare the results of different inter-electrode spacings using the same data-processing setup. Therefore, it remains uncertain if the same accuracy achieved with a 2 mm inter-electrode spacing could be obtained with

the data-processing used in this study. However, comparing the correlation from the study by Blanchard et al. [23] and the results from this study with the 4 mm inter-electrode spacing, the correlation factor is significantly lower than expected, potentially influencing shapes and AT to an extent that could hinder the creation of accurate maps.

Table 2: Correlation factors between filtered measured and calculated BEG for the 2-chamber configuration.

2-chamber configuration	Very weak 0 – 0.19	Weak 0.2 – 0.39	Moderate 0.4 – 0.59	Strong 0.6 – 0.79	Very strong 0.8 – 1.0
Working mode	1%	8%	13%	61%	17%
Grid	5%	17%	50%	22%	6%
bolus	1%	7%	14%	70%	8%

Table 3: Correlation factors between filtered measured and calculated BEG for the 4-chamber configuration.

4-chamber configuration	Very weak 0 – 0.19	Weak 0.2 – 0.39	Moderate 0.4 – 0.59	Strong 0.6 – 0.79	Very strong 0.8 – 1.0
Working mode	1%	3%	8%	68%	20%
Grid	0%	6%	36%	54%	4%
bolus	0%	4%	6%	72%	18%

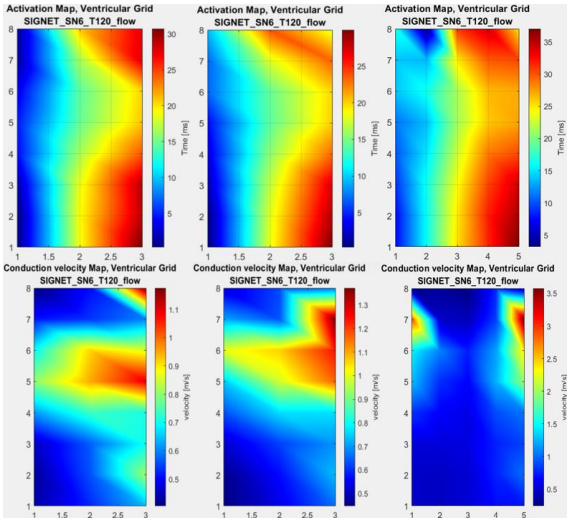

Figure 30: AT and CV maps for measured BEG (left), calculated BEG 24 points (middle) and calculated BEG 40 points (right).

In Figure 30, three AT (top) and CV (bottom) maps are shown: one using measured signals, one using calculated BEG using the same (24) amount of points as the measured signals and one using calculated BEG with increased (40) amount of points. In some cases, the measured and calculated maps are almost identical in case of similar amount of points, but when a larger number of BEG are calculated, the maps start to show different patterns. Also, within the CV maps at the bottom there are small changes between the measured and calculated 24-point maps. But, when 40 points are calculated the CV at specific points seems to be significantly higher. On one hand, this makes sense as the spacing between the points is smaller and less data is smoothed out, but in other places, a large CV suddenly appears in measured low CV areas.

As the main reason for using calculated BEG was to create finer maps, it does not seem reasonable to continue using calculated BEG in this study. It remains unclear if the BEG are as accurate in comparison to the measured BEG and if the maps represent the real-life scenario.

4.4 Bipolar ARI maps

Figures 31 and 32 show ARI maps from the UEG and the BEG. The UEG maps have significantly more data points than the BEG maps, making it harder to identify patterns in the BEG maps. In some cases, the ARI jumps from high to very low values for the BEG, whereas the differences between the separate ARI values are much smaller in the UEG. The electrode spacing and the way RT is identified in the BEG also play a role. The RT lies in a lower frequency range, which is not typically part of the filtering range for the BEG, making it difficult to identify the RT without decreasing the filtering range.

In this case, the filtering range was reduced to 20 Hz for the BEG instead of 30 Hz. Initially, the MV method was used to identify the BEG RT just like the UEG RT, but this did not improve the results. A

different windowing method was then used, but this also did not improve the identification of the RT. Figure 22 shows an example of both RT from UEG and BEG. As the measurement locations are close to each other, the RTs should be closely spaced together. However, the BEG peaks are so hard to identify that the RT often seems to represent the maximum of the T-complex of the UEG rather than the upwards slope.

Therefore, it was decided to no longer use the ARI maps from the BEG, as they did not provide reliable results.

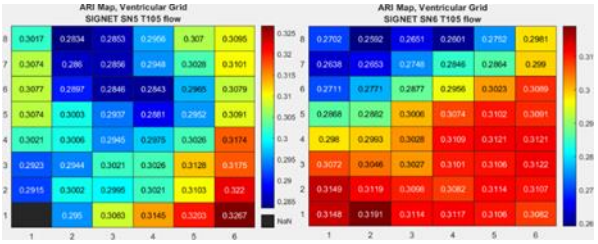

Figure 31: ARI maps of the mean ARI from every UEG during a 2-chamber configuration. In this Figure two maps are shown to the left from experiment 5 and to the right from experiment 6, during a specific timestamp.

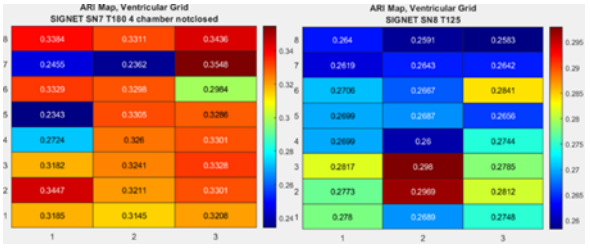

Figure 32: ARI maps of the mean ARI from every BEG during a 2-chamber configuration. In this Figure two maps are shown to the left from experiment 5 and to the right from experiment 6, during a specific timestamp.

5 Results

5.1 Grid pacing

To determine if local activation can better be visualized using BEG compared to UEG, experiments were conducted where pacing occurred within the electrode grid. Figure 33 illustrates the AT maps, CV maps for both UEG and BEG, the ARI map, and the PV loops during a grid pacing measurement in a 2-chamber configuration. The pacing location was from electrodes 21 and 29, at coordinates (3,5) and (4,5) for the UEG maps, and at (2,5) for the BEG maps.

From Figure 1, significant changes in patterns on the maps compared to normal pacing were observed (see Figures A5 and A7). Both UEG and BEG AT maps show outward motion from the center. The CV maps also differ from their previous states, with a single point now showing very high CV, obscuring the original pattern. This is true even in the BEG CV map where the CV is lower. This indicates that grid pacing significantly influences activation and CV maps.

The ARI map shows higher values in the middle of the grid compared to normal pacing (see Figure A10), although the same low ARI values remain at the top. The PV loop shape became slightly narrower, indicating a decreased SV. Since the HR remained the same, CO also decreased.

In the 4-chamber configuration (see Figure A23), similar effects were observed. Activation maps show an outward motion from the center, and the highest CV is near the grid pacing location. The ARI map shows lower values surrounding the grid pacing location instead of higher values. The PV loop shape remained the same, but HR increased significantly, resulting in higher CO.

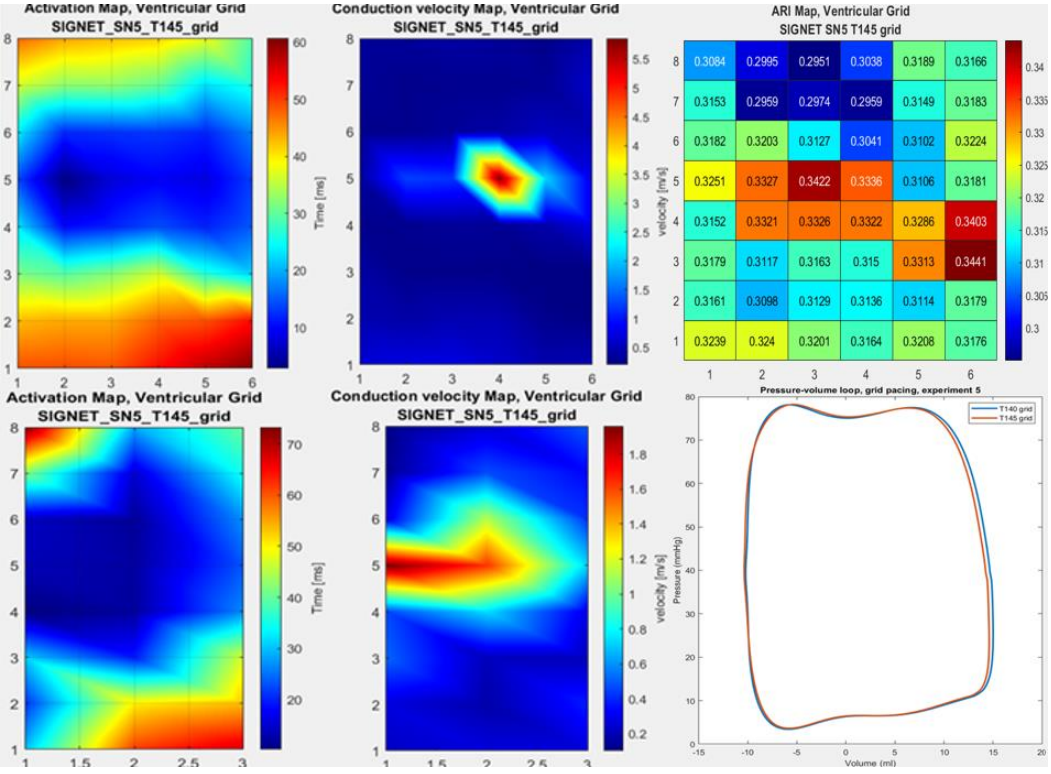

Figure 33: Top row from left to right, activation map, CV map and ARI map from UEG. Bottom row from left to right, activation map and CV map from BEG and the last figure contains the PV-loops during pacing on the grid. These figures represent the results from experiment 5 during 2-chamber configuration.

Table 4: All parameters measured during baseline, grid pacing and ion boluses for multiple experiments during 2 and 4-chamber configuration and using unipolar and bipolar electrograms. Green indicates the higher values with respect to the working mode and orange the lower values.

	Unipolar		Bipolar		Unipolar		Bipolar				
	ARI mode	ARI std	ARI mode	ARI std	CV mean	CV range	CV mean	CV range	SV	HR	CO
Units	s	s	s	s	m/s	m/s	m/s	m/s	ml	bpm	L/min
Baseline ex.5	0.3025	0.0178	0.3074	0.0282	0.6261	0.4232-0.8559	0.5841	0.4176-0.7428	31.54	99	3.1
Baseline ex.6	0.3225	0.0149	0.3236	0.0283	0.9891	0.4430-1.9849	0.7672	0.3781-1.3708	30.78	97	3
Baseline ex.7	0.3230	0.0077	0.3318	0.0368	1.1335	0.4983-1.8919	0.8331	0.4983-1.8919	29.25	114	3.3
Baseline ex.8	0.2875	0.0186	0.2831	0.0167	0.7955	0.2843-2.0842	0.8658	0.2843-2.0842	26.70	108	2.9
2-chamber Grid ex.5	0.3155	0.0157	0.3155	0.0300	0.4363	0.2044-1.3287	0.4484	0.1173-1.7351	24.97	99	2.5
2-chamber Grid ex.6	0.3277	0.0187	0.3601	0.0420	0.5555	0.2020-1.2687	0.8940	0.3088 – 7.9006	39.58	74	2.9
4-chamber Grid ex.7	0.3155	0.0109	0.3358	0.0233	0.7074	0.2742-1.5969	1.0176	0.6305-3.6300	32.25	105	3.4
4-chamber Grid ex.8	0.2588	0.0192	0.2628	0.0221	0.5148	0.2003-1.5416	0.6874	0.1881-2.7698	27.50	114	3.1
2-chamber Ca+ 5.p1									42.06	72	3.0
2-chamber Ca+ 5.p2									42.28	103	4.4
2-chamber Ca+ 5.p3									42.18	103	4.4
2-chamber Ca+ 5.p4	0.3115	0.0217	0.3196	0.0243	1.4614	0.5568-5.2669	0.8164	0.2929-8.7335	41.89	103	4.4
4-chamber Ca+ 8.p1	0.2953	0.0188	0.2953	0.0186	1.1274	0.4171-4.0061	1.0694	0.4254-2.6601	33.64	78	2.6
4-chamber Ca+ 8.p2									32.63	100	3.2
4-chamber Ca+ 8.p3									31.90	98	3.1
2-chamber Mg+ 5.p1	0.3074	0.0119	0.3155	0.0199	1.1438	0.4725-4.3632	0.8476	0.2063-6.6043	39.89	105	4.2
2-chamber Mg+ 5.p2	0.3074	0.0132	0.3155	0.0199	1.1240	0.4659-4.0616	0.9453	0.2127-7.7994	38.99	104	4
4-chamber Mg+ 8.p1	0.2872	0.0103	0.2912	0.0182	1.4528	0.3517-11.7452	0.8143	0.3809-1.7571	31.65	96	3.0
4-chamber Mg+ 8.p2									30.50	86	2.7
4-chamber Mg+ 8.p3									31.51	86	2.7
2-chamber K+ 5.p1									38.76	102	4.0
2-chamber K+ 5.p2	0.3074	0.0124	0.3155	0.0195	1.0935	0.4710-3.6289	0.9778	0.2130-8.6836	37.03	105	3.9
2-chamber K+ 5.p3									45.20	69	3.1

Table 4 summarizes the ARI mode, standard deviation, mean CV, 90% CV range, SV, HR, and CO for experiments 5-8 during grid pacing compared to the baseline. Key observations include that the ARI mode increased in both UEG and BEG for the 2-chamber configuration and varied in the 4-chamber configuration. The mean CV decreased in UEG for all experiments, while BEG showed mixed results. The SV generally increased, except in experiment 5, where it significantly decreased. The HR results were mixed, leading to mixed CO results. Lastly, the maximum ranges of CV were generally larger during grid pacing for BEG and smaller for UEG.

Due to the key observations, including the highest BEG CV values being more centered at the pacing site compared to UEG, it was observed that local activation patterns are better visualized using bipolar electrograms.

5.2 2 vs 4 chamber configuration

In the working mode, the focus is primarily on comparing the 2-chamber and 4-chamber configurations. The decision to prioritize UEG over BEG was based on several factors. The AT map patterns for UEG and BEG are similar, but the ARI derived from BEG is less reliable. Additionally, CV maps show only minor differences, and UEG maps provide denser data compared to BEG maps. Therefore, UEG was chosen yielding a more effective comparison between the 2-chamber and 4-chamber configurations.

However, it is important to note that BEG has its own advantages in certain contexts. While UEG is better suited for providing a dense and reliable dataset in the working mode, BEG excels in local activation analysis. BEG measures potential differences between adjacent electrodes, offering detailed information about electrical conduction and helping to identify re-entry circuits and arrhythmia

mechanisms. In the appendix, BEG results can still be viewed, particularly for CV maps where some BEG cases show significantly different patterns.

5.2.1 Activation maps

In Figure 34, 2 AT maps are shown for a 2-chamber configuration using UEG. The AT map on the left side displays how the activation propagates along the electrode grid during the Langendorff mode. Compared to the electrode grid location shown in Figures 18 and 19, the activation moves from the top left, near the left coronary artery, to the bottom right, near the apex of the heart. When switched to working mode, the activation pattern changes, moving from the bottom left to the top right, indicating that the activation originates more from the apex and moves upwards. Figure A4 in the appendix shows the full extent of this experiment, revealing small variations in the measurements.

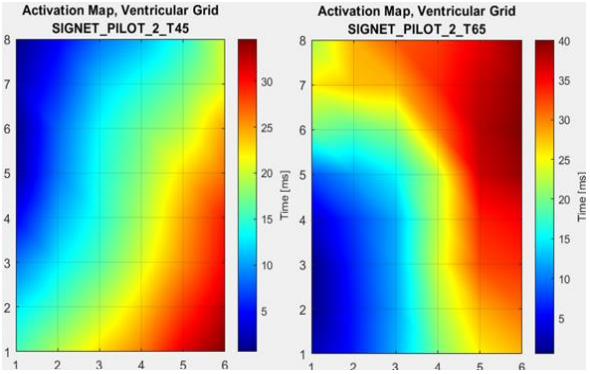

Figure 34: AT maps of the UEG during a 2-chamber experiment. Left: AT map during Langendorff. Right: AT map during working mode.

When examining other experiments utilizing UEG (Figure A5), differences in the shapes of the activation maps are observed. They all propagate from the left to the right, but some originate more from the bottom left while others originate from the top. The shape of the activation pattern varies; in some cases, activation accelerates at certain points, while in others, it takes longer. Significant changes in the activation pattern can occur during Langendorff mode, sometimes resulting in a pattern at the end of Langendorff mode that matches the beginning of the working mode.

In Figure 35, AT maps from UEG in 4-chamber configuration are shown for different moments during an experiment. Workflow during an experiment is from Langendorff mode to 2-chamber and then to 4-chamber. The AT maps show that there is not much change in the AT patterns during the working mode in both configurations.

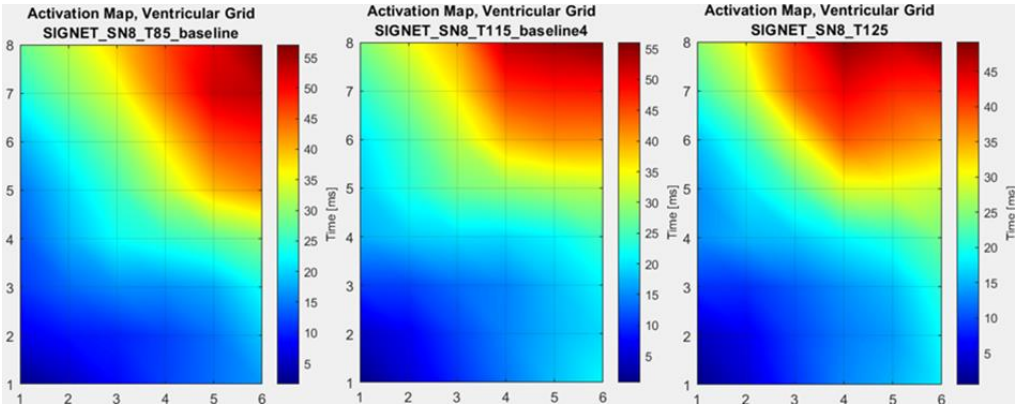

Figure 35: 4-chamber experiment AT maps of the UEG. In the Figure to the left an AT map is shown during the 2-chamber configuration. In the middle an AT map just after the change from 2 to 4-chamber and to the right a AT map in 4-chamber configuration is shown 40 minutes after the change.

In another experiment using the 4-chamber configuration, the electrode grid was damaged, causing the need to replace the grid on the heart potentially on a shifted location. Figure A8 in the appendix shows several AT maps during this experiment. Initially, activation starts at the bottom right in the 2-chamber configuration and then shifts to start at the top left, differing significantly from Figure 3, where activation propagates from the bottom left to the top right. Figure A9 in the appendix shows an AT map

during Langendorff mode, where activation starts at the bottom left and propagates to the top right. In the working mode, the activation starts at the bottom left but is more spread along the bottom of the electrode grid, originating more from the bottom than from the left.

5.2.2 Activation recovery interval

As mentioned in the methodology there are multiple ways to determine the ARI. It is possible to create maps that contain the average ARI per electrode and plots them on the whole map, shown in chapter 5.3.1 and 5.3.2. It is also possible to plot all the measured ARI during a measurement in a histogram. On this histogram the mode is taken (instead of mean) as the histogram has an odd shape and from this point the standard deviation can be calculated, shown in chapter 5.3.3.

ARI maps

The mean ARI maps from UEG for experiments 5 and 6 in the 2-chamber configuration are shown in Figure 36. The maps reveal patterns in mean ARI values, with blue areas representing smaller ARI values and red areas indicating larger values. For experiment 5, the mean ARI ranges from 0.285 to 0.325 seconds, while for experiment 6, the range is from 0.26 to 0.32 seconds. In experiment 5, lower ARI values are spread out on the left side and top of the grid, whereas in experiment 6, lower ARI values are concentrated only in the top left corner with the highest ARI values in the bottom left corner. Additional ARI maps for the UEG at various timestamps, shown in Figure A10 in the appendix, display minimal changes over time. The ranges are consistent, and the overall shapes of the ARI maps remain stable throughout the experiment.

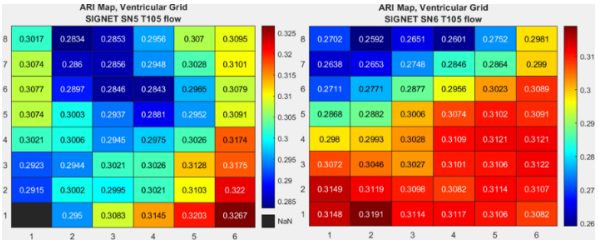

Figure 36: ARI maps of the mean ARI from every UEG during a 2-chamber configuration. In this Figure two maps are shown: left from experiment 5 and right from experiment 6, during a specific timestamp.

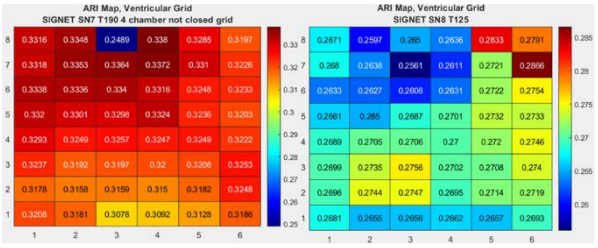

Figure 37: ARI maps of the mean ARI from every UEG during a 4-chamber configuration. In this Figure two maps are shown: left from experiment 7 and right from experiment 8, during a specific timestamp.

The mean ARI maps derived from the UEG of experiments 7 and 8 in the 4-chamber configuration are shown in Figure 37. In the map from experiment 7, an oddly low ARI value is surrounded by very high values, all above 0.3 seconds. The ARI values appear smaller at the bottom of the grid and higher at the top. Additional measurements during experiment 7, presented in Figure A12 in the appendix, reveal a clear pattern emerging at certain timestamps, especially in the last two maps.

The map from experiment 8 looks similar to the map of experiment 5 in Figure 36, with lower ARI values in the same location and increasing values towards the right. Additional maps from experiment 8, shown in Figure A12, exhibit different patterns at various timestamps. While the overall patterns vary, high values are consistently present in certain areas, leading to differing ARI ranges across the maps.

Average ARI comparison

Tables 7 and 9 in the Appendix present ARI modes and standard deviations for experiments in 2-chamber and 4-chamber configurations, respectively. In the 2-chamber setup (Table 7), ARI modes varied notably across experiments (0.2675 to 0.3150 seconds), influenced by pacing rates (96 to 105 bpm). Actual HR fluctuations, despite efforts to maintain consistency with pacing, also impacted ARI measurements.

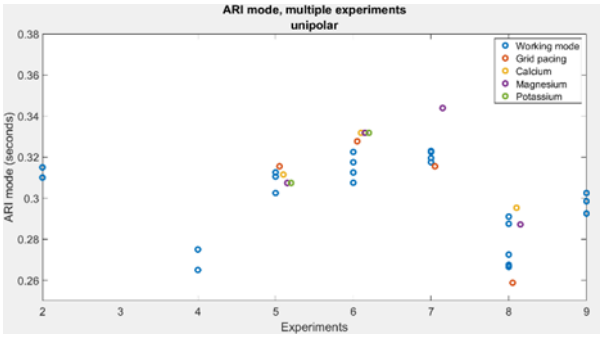

Figure 38: ARI mode of multiple experiments during working mode (blue), grid pacing (red), calcium bolus (yellow), magnesium bolus (purple) and potassium bolus (green), using UEG.

ARI modes and standard deviations were tracked at different timestamps during experiments to assess temporal changes. In 2-chamber setups, ARI modes showed average differences of 2 to 5 ms between timestamps, fluctuating rather than following a linear trend. For instance, experiment 5 exhibited a decrease in ARI mode from 0.3105 to 0.3025 seconds, with variations observed at intermediate points.

Fewer experiments were conducted in the 4-chamber configuration (Table 9), yet significant variations in ARI modes were evident. Experiment 7, paced at approximately 100 bpm, showed higher ARI values compared to Experiment 8, paced at around 115 bpm. ARI ranges during working mode differed between experiments (Experiment 7: 0.3175 to 0.3230 seconds, experiment 8: 0.2665 to 0.2910 seconds), with slight increases observed over time.

Figures 38 depict plots of calculated ARI modes, highlighting substantial variability between configurations and experiments within each setup. Interestingly, no consistent difference in ARI ranges was observed between the 2-chamber and 4-chamber setups, with unique ranges noted in each experiment during working mode.

Notably, despite efforts to maintain constant pacing rates, slight fluctuations in HR during experiments (Figure A14 in the appendix) underscored potential influences on ARI measurements beyond experimental duration alone.

5.2.3 Conduction velocity

CV maps

The CV can be determined from the AT and AT maps using an inverse gradient method. The resulting CV maps for the 2-chamber and 4-chamber configurations, using the UEG measurement setup, are shown in Figures 39 and 40, respectively.

For the 2-chamber configurations, each experiment exhibits different CV maps. Additional timestamps during the working mode, shown in Figure A15 in the appendix, indicate that the UEG patterns remain consistent for almost all measurements. In experiment 5, the pattern shows lower CV values at the bottom of the grid and higher CV values at the top. Experiment 6, however, displays slightly different patterns with lower CV values at the bottom left and top right, and higher values in between these lower regions.

Similarly, the 4-chamber configurations also exhibit different CV maps for each experiment. The CV maps for the 4-chamber configurations, shown in Figure 8, highlight these differences. As depicted in Figures A17 in the appendix, the CV patterns remain consistent during the working mode for most cases. In experiment 7, the pattern shows a region of higher CV in the top left, surrounded by lower values. In experiment 8, the higher CV region is located at the bottom of the grid, close to the apex, also surrounded by lower CV values.

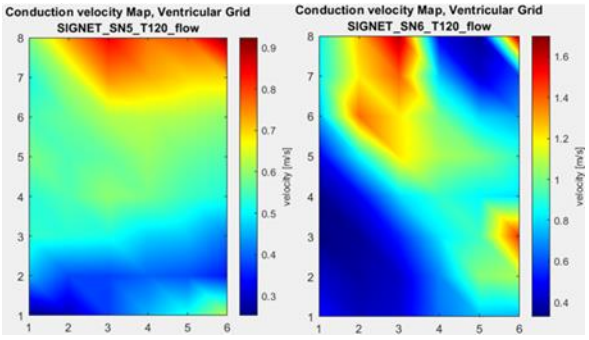

Figure 39: CV maps from experiments 5 and 6 using the 2-chamber configuration and the UEG measurement set up. In blue the smallest CV are shown and in red the largest values.

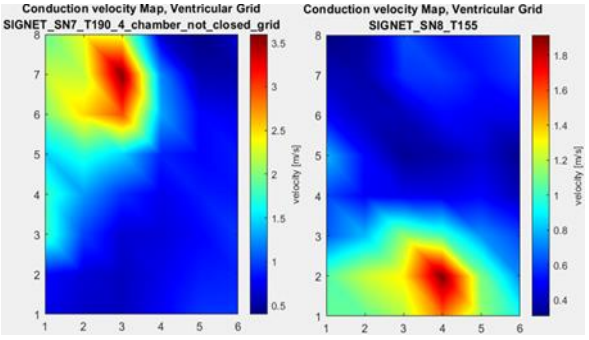

Figure 40: CV maps from experiments 5 and 6 using the 4-chamber configuration and the UEG measurement set up. In blue the smallest CV are shown and in red the largest values.

Average CV comparison

Figures 41 present the mean CV values for each electrode, measurement, multiple experiments, and multiple methods, combining two experiments in either a 2-chamber or 4-chamber configuration using the UEG. The limited number of CV calculations per measurement (48) made creating individual histograms unfeasible, so all experiments during the working mode were combined to identify CV trends. The histograms reveal a skewed distribution of CV values, indicating prevalent ranges within the measurements. Comparing the CV maps from the UEG, the distribution of CV is similar between the 2-chamber and 4-chamber configurations. The 4-chamber configuration exhibits a wider range of CV values, while the 2-chamber configuration shows a pronounced spike in the histogram. The range of UEG CV values in the histograms is approximately 0.3 to 1.7 m/s.

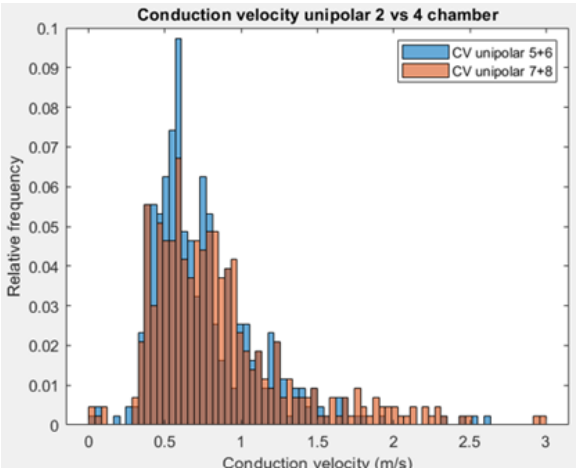

Figure 41: Histograms of all mean CV from the UEG during 2 and 4-chamber configuration

To further investigate CV per measurement per experiment, mean CV and 90% ranges were calculated. Tables 9 to 12 in the appendix show all mean CV values and 90% ranges for the 2 and 4-chamber configurations. Figure 42 visualizes these mean CV values, highlighting the different ranges of CV in each experiment. For the 2-chamber configuration, the mean CV during the working mode ranges from 0.56 to 1.22 m/s for the UEG, with smaller ranges within each experiment. The CV

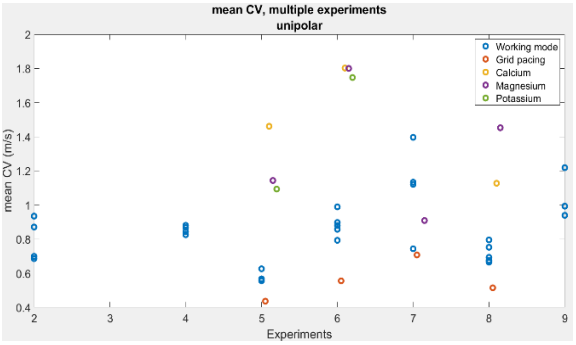

Figure 42: Mean CV from the UEG during working mode, grid pacing and ion boluses, for multiple experiments in both 2-chamber configuration (experiments 2, 4, 5, 6 and 9) and 4-chamber configuration (experiments 7 and 8)

differences within experiments generally remain below 0.1 m/s. For the 4-chamber configuration, only two experiments are available. The minimum mean UEG CV is 0.66 m/s, and the maximum is 1.4 m/s, occurring in different experiments. The mean UEG CV for experiment 7 ranges from 0.74 to 1.40 m/s, and for experiment 8, from 0.66 to 0.79 m/s. CV differences generally range between 0.04 to 0.17 m/s.

The 90% range of the CV during each measurement is also important. In the 2-chamber configuration during working mode, the overall minimum of the 90% range for all UEG CV is 0.3263 m/s, and the maximum is 3.0286 m/s. The length of these ranges varies from a minimum of 0.4327 m/s to a maximum of 2.2223 m/s. For the 4-chamber configuration during working mode, the overall minimum of the 90% range for all UEG CV is 0.3376 m/s, and the maximum is 3.0748 m/s. The range length varies from a minimum of 0.6327 m/s to a maximum of 2.4383 m/s. Comparing the 2-chamber and 4-chamber configurations, the minimum and maximum ranges, and values for the UEG are similar in both cases.

5.2.4 Pressure-volume loops and additional parameters

To compare the mechanical activation with the electrophysiology, pressures and flow rates were measured during the experiments. These measurements were used to create PV loops. This chapter presents the results of the PV loops and additional parameters concerning the working mode. Figure 43 and 44 show the results of experiments with 2- and 4-chamber configurations respectively.

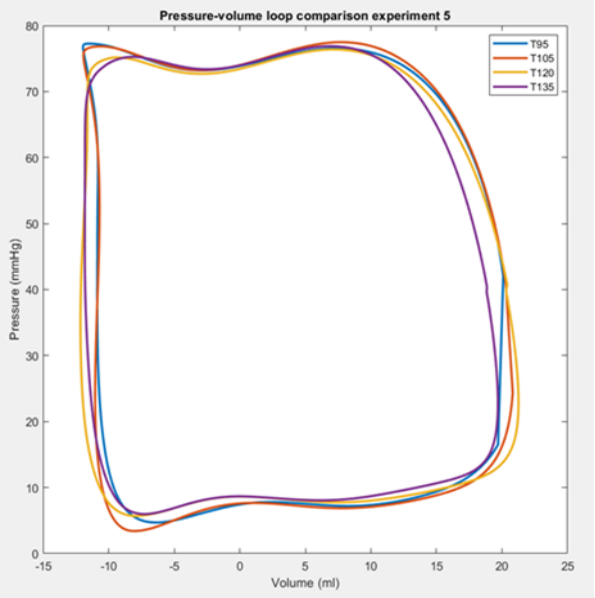

Figure 43: PV loops of experiment 5 during working mode in a 2-chamber configuration.

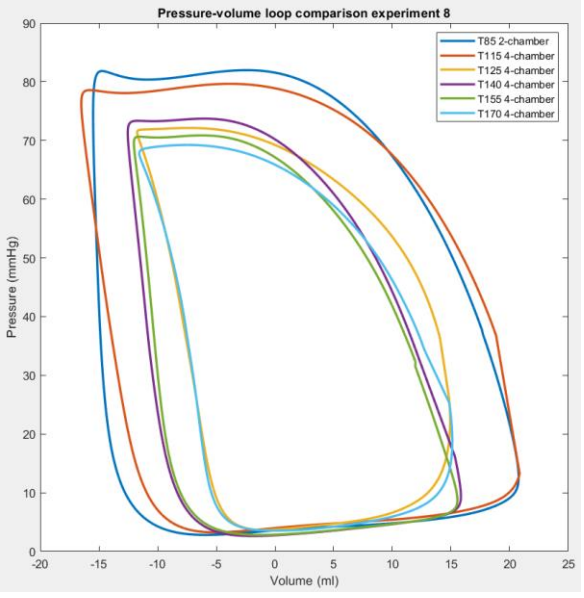

Figure 44: PV loops of experiment 8 during working mode in a 4-chamber configuration. The blue line indicates the loop in a 2-chamber configuration just before change and at T125 a large shift in PV loop can be observed.

Pressure-Volume loops

In general, Figure 42 exhibits a pattern that is similar to the theoretical PV loops. It has near-straight increases in pressure in the isovolumetric phases. Additionally, in the filling phase (A), there is a slight increase in pressure. In the ejection phase (C), the shape is slightly different, showing a dip in pressure but also a spike at the end of the ejection phase towards the closure of the aortic valve. However, another experiment with the 2-chamber configuration shows completely different results (see Figure A20 in the appendix). This PV loop has a significant dip in pressure during the ejection phase (phase C)

and remains low. It also has an unusual shape where the mitral valve close in the bottom right corner, where the volume increases and decreases, but the pressure remains unchanged.

Figure 44 presents PV loops for an experiment using the 4-chamber configuration. Similar to Figure 43, this PV loop closely resembles the theoretical PV loops. As time progresses, the PV loop starts to become smaller but maintains a similar shape. Another experiment using the 4-chamber configuration showed completely different results, which can be seen in Figure A21 in the appendix. Initially, in a 2-chamber configuration, the PV loop still somewhat resembles the theoretical loop. Phases A and B are similar, but starting from phase C, a dip in pressure can be seen, followed by an increase. When the pressure drops in phase D, the volume already becomes larger, where all valves should be closed. After the change at the end-diastolic phase, the End-Diastolic Pressure-Volume Relationship (EDPVR) becomes a lot steeper, and the overall size of the loop first increases and then becomes smaller, with an even steeper EDPVR.

Cardiac Function Parameters

Table 7 shows the SV, HR, and CO for multiple experiments during working mode. Experiments 5 and 6 show almost no change in SV, HR, and CO during the experiments, with only a dip in SV and thus a decrease in CO at the end of experiment 5. On the other hand, experiments 7 and 8 exhibit significant differences in SV, HR, and consequently CO. In these experiments, the initial measurements are taken in a 2-chamber configuration and are subsequently changed to a 4-chamber configuration. After the first measurements, the HR in both cases increases, with either an increasing or decreasing SV, leading to an increased CO, which later starts to drop due to either a decrease in SV or a decrease in HR.

Table 5: Stroke volume, Heart rate and Cardiac Output during multiple experiments at different timestamps during working mode. Experiments 5 and 6 represent the 2-chamber configurations and experiments 7 and 8 the 4-chamber configuration.

Ex. 5 Units	**SV ml**	**HR bpm**	**CO L/min**		**Ex.7**	**SV ml**	**HR bpm**	**CO L/min**
T95	32.08	99	3.2		**T135 (2)**	39.36	100	3.9
T105	32.78	99	3.2		**T170**	36.76	115	4.2
T120	33.44	99	3.3		**T180**	36.12	115	4.2
T135	31.54	99	3.1		**T190**	29.25	114	3.3
Ex.6 Units	**SV ml**	**HR bpm**	**CO L/min**		**Ex.8 Units**	**SV ml**	**HR bpm**	**CO L/min**
T90	29.30	98	2.9		**T85 (2)**	36.30	99	3.6
T105	29.64	98	2.9		**T115**	37.40	104	3.9
T120	30.11	98	2.9		**T125**	26.70	114	3.0
T135	30.37	97	2.9		**T140**	28.42	98	2.8
T150	30.78	97	3.0		**T155**	27.60	98	2.7
					T170	26.70	108	2.9

5.3 Ion boluses

Calcium bolus

To identify how electrophysiology and mechanical activation are influenced by a calcium imbalance, a bolus of calcium was added during a measurement and the electrophysiology and mechanical activation data were recorded. Table 4 shows a large portion of the acquired data for some of the experiments. Due to problems with data acquisition, only one moment during the bolus was measured for the electrophysiology, but multiple changes in mechanical activation could be measured during a single measurement.

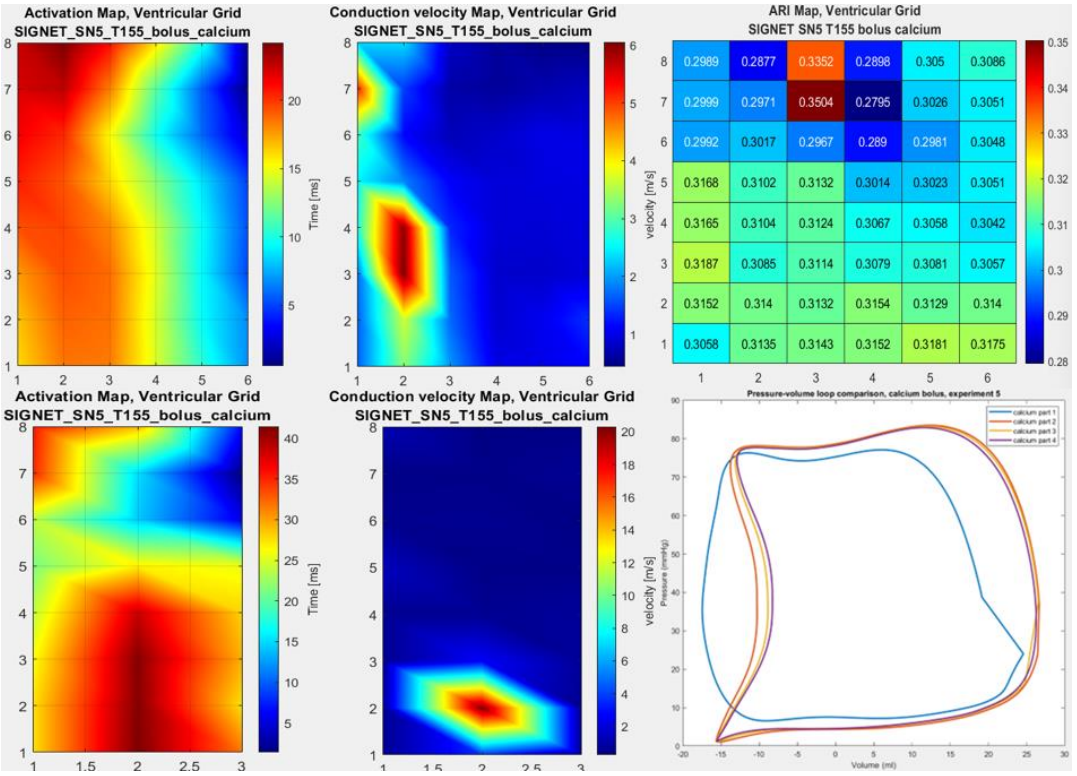

Figure 45: Top row from left to right, activation map, CV map and ARI map from the unipolar electrograms. Bottom row from left to right, activation map and CV map from the bipolar electrograms and the last figure contains the PV-loops during a calcium bolus. These figures represent the results from experiment 5 during 2-chamber configuration.

Regarding changes in electrophysiology, Table 4 shows the mode ARI and the mean CV during the measurements, which can be compared to the values measured during the working mode. In the 2-chamber working mode, the change in ARI mode from UEG showed an approximate increase of 3%, and for BEG, approximately 4%. The mean CV increase ranged from 82% to 133% for UEG and 31% to 40% for BEG.

In the 4-chamber experiment, only one measurement was performed, which showed an increase in the ARI mode for UEG of 3% and for BEG of 4%. For the mean CV, an increase of 42% was found for UEG and 24% for BEG.

For the AT maps, CV maps, and ARI maps, only one measurement per configuration is evaluated in this section. The effect of the calcium bolus on the different maps in the 2-chamber configuration can be seen in Figure 45 and should be compared to the baseline maps (the last maps in the working mode hour, see Figures 35, A7, A9, A10, A12, A15 and A17). The activation map from the UEG shows a complete reversal in direction, moving from right to left instead of left to right. For the BEG, the

activation pattern no longer moves left to right; it starts at the top right and splits towards the bottom and top left.

In the CV maps, the patterns of slowly increasing or decreasing CV seen during the working mode are replaced by very high CV points at different locations during the bolus. In experiment 5, the maximum CV is significantly higher for UEG compared to BEG, with different locations for these maxima.

For the ARI map, only UEG are used for comparison between working mode and the calcium bolus. The minimum ARI values remain in a similar spot to the working mode, but there are very high ARI values in the same area.

In the PV loops, a shift from left to right is visible, along with an increase and decrease in volume during the relaxation phase (phase D). The diastolic pressure is much higher, resulting in a larger overall PV loop. Despite the shape of the PV loops, the SV did not change significantly during the bolus measurement itself. However, compared to the baseline, the SV increased by approximately 25%. Without pacing, the HR initially remained low but later increased, resulting in a change in CO from approximately 3 to 4 l/min.

In the 4-chamber configuration, as seen in Figure A29 in the appendix, the activation map pattern remains the same or shows slight changes in wave propagation speed for both UEG and BEG. The CV map patterns are totally different during the bolus compared to the working mode, with multiple locations showing higher CV values at different locations.

For the ARI map, the bolus introduces a pattern that was not present during the working mode. Initially, the CV was relatively uniform across the grid, but after the bolus, a pattern emerges with low CV values in the top left and higher CV values in the middle to bottom right.

In the PV loops, there is a visible shift. Initially, during the working mode, the PV loops are quite small, ranging from -10 to 15 ml and 0 to 70 mmHg. During the bolus, this range changes to -15 to 17 ml and 0 to 80 mmHg, making the PV loop higher, wider, and thus larger. For experiment 8, the isovolumetric contraction has almost returned. The pressure seems to increase with almost no change in volume. During the working mode, there was no true isovolumetric contraction visible.

When examining the cardiac parameters measured during the bolus and working mode in Table 4, it is evident that the SV increases with the addition of the bolus. Initially, due to a low HR, the CO is lower than during the working mode. Over time, as the HR increases and the SV remains the same, the CO also increases.

Magnesium bolus

To study the influence of a magnesium imbalance on the electrophysiology and mechanical activation, a magnesium bolus of 1500 mg was added. Table 4 presents the mode ARI, standard deviation, mean CV, and range for the UEG and BEG.

In the 2-chamber configuration, one experiment showed no change after the magnesium bolus, while another showed some changes. The mode ARI dropped by about 1.5% for both UEG and BEG. The mean CV for the UEG dropped by 22%, while the BEG mean CV increased by 4%. In the 4-chamber configuration, the mode ARI dropped by 2.5% for UEG and 1.5% for BEG. The mean CV increased by 29% for UEG but dropped by 24% for BEG.

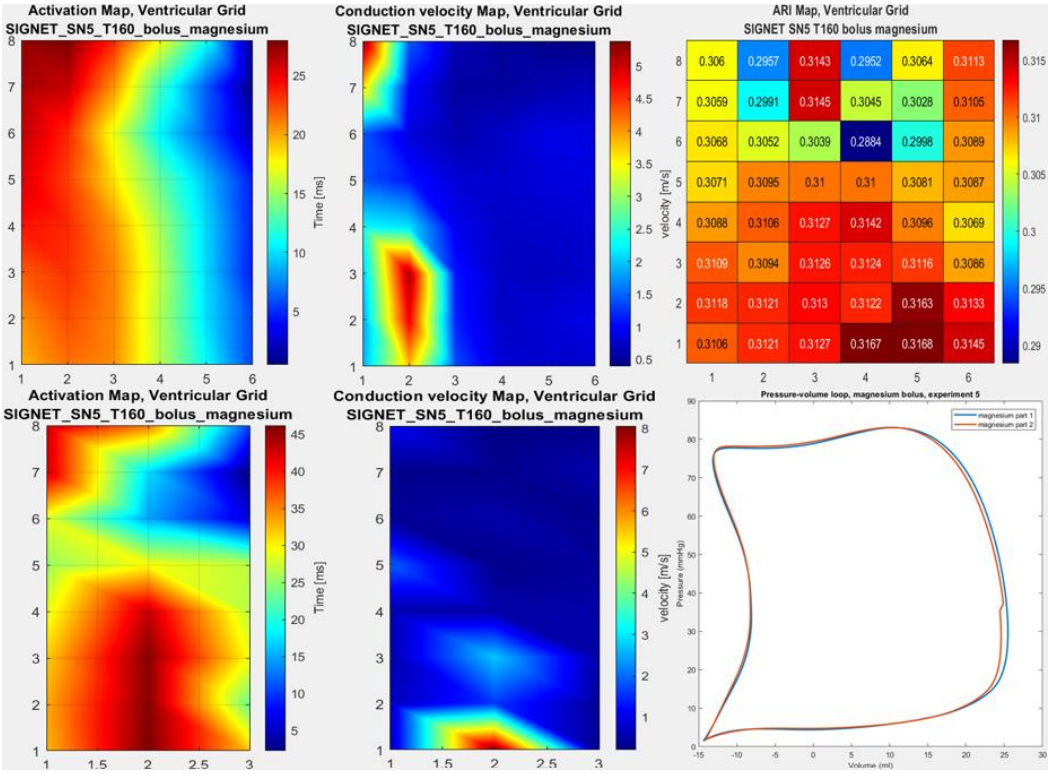

Figure 46: Top row from left to right, activation map, CV map and ARI map from the unipolar electrograms. Bottom row from left to right, activation map and CV map from the bipolar electrograms and the last figure contains the PV-loops during a magnesium bolus. These figures represent the results from experiment 5 during 2-chamber configuration.

For the AT, CV, and ARI maps, only one measurement per configuration is evaluated. In the 2-chamber activation map (Figure 46), there is not much change between the calcium and magnesium boluses for both UEG and BEG, though the activation duration increased slightly. CV maps show that for UEG, the largest CV values move outward, while for BEG, they move toward the bottom. ARI maps indicate that areas with high ARI values become lower, especially at the bottom of the grid, even though the values remain similar.

PV loops show minimal change in shape after the magnesium bolus, but the loops become slightly narrower, resulting in a decrease in SV by 2 to 3 ml, and a stable HR, resulting in a decrease in CO by 0.2 to 0.4 L/min.

In the 4-chamber configuration, the PV loops of experiment 8 initially remains the same as the calcium bolus, then shifts left and downward, reducing the pressure range by 10 mmHg. Isovolumetric relaxation is affected, with blood moving into the heart while all valves are supposed to be closed. Experiment 7 shows significant changes from the working mode to the bolus, with the EDPVR becoming flatter, higher diastolic pressure, and an increased volume range, significantly increasing SV. Experiment 8 shows a decrease in SV by 1 ml and HR, resulting in a CO that is 0.4 L/min lower. Experiment 7 shows an increase in SV by 10 ml, with HR decreasing, resulting in a similar CO.

Potassium bolus

To study the impact of a potassium imbalance on electrophysiology and mechanical activation, potassium boluses were administered in the 2-chamber configuration. The 4-chamber configuration failed after the magnesium bolus. Table 4 summarizes the mode ARI, std, mean CV, and range for both experiments (5 and 6). The ARI mode remained consistent with that during the magnesium bolus. The mean CV decreased by 5 – 7% for the UEG and increased by 15 – 20% for the BEG.

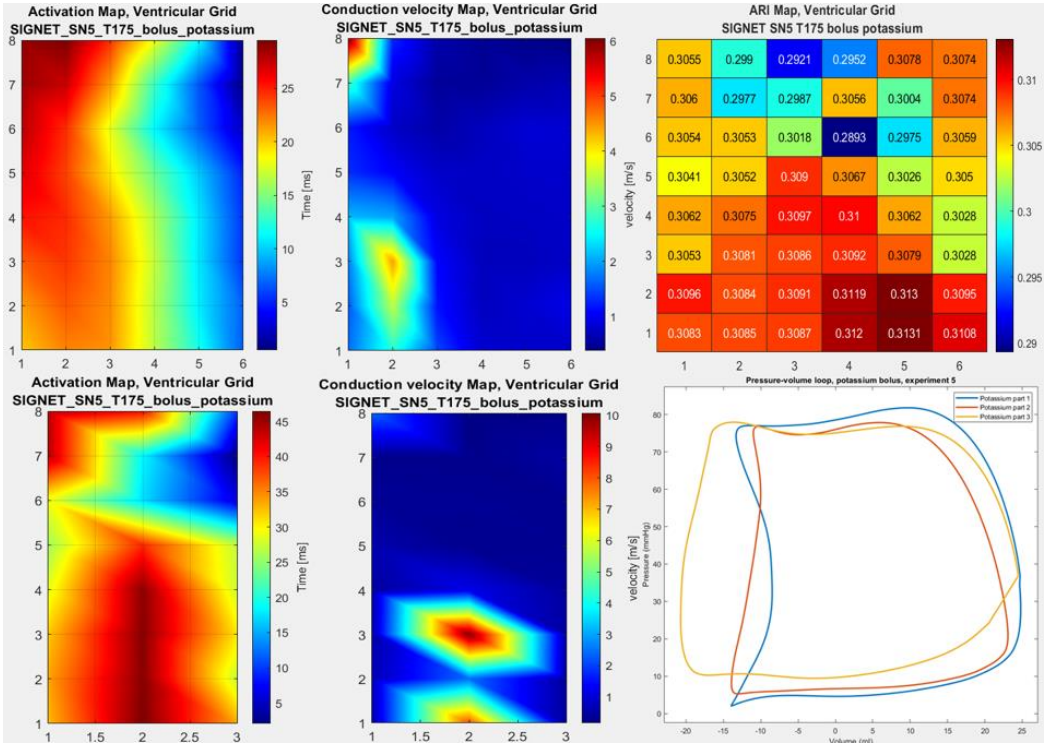

Figure 47: Top row from left to right, activation map, CV map and ARI map from the unipolar electrograms. Bottom row from left to right, activation map and CV map from the bipolar electrograms and the last figure contains the PV-loops during a potassium bolus. These figures represent the results from experiment 5 during 2-chamber configuration.

Figure 47 shows the AT, CV, and ARI maps for experiment 5. The UEG activation maps show minimal differences between the magnesium and potassium bolus. BEG maps show a slight change as two red sections move closer. UEG CV maps show slightly lower intensity, but increased color bar values indicate a CV increase in the top left corner with the potassium bolus. BEG maps reveal an additional CV peak at coordinates (2,3). ARI maps show a shift where high ARI values at the top of the electrode grid are replaced by smaller values, with larger ARI values remaining at the bottom.

The PV loop for experiment 5 (Figure 47) shows minimal initial change but later turns slightly. Phase A starts with higher pressure, and during phase B, volume decreases more with increasing pressure, resulting in a smaller loop. As arrhythmias occur, the loop starts to double, leading to a larger average PV loop. In experiment 6 (Figure A36), the PV loop initially widens, and lowers compared to the magnesium bolus, then becomes significantly smaller in both width and height. Volume range changes from -25 to 15 ml to -15 to 7 ml, and pressure range changes from 5 to 80 mmHg to 0 to 70 mmHg.

Table 4 shows that the potassium bolus led to a decrease in SV by approximately 2 ml in experiment 5, with the HR remaining unchanged, resulting in a slight decrease in CO. In experiment 6, SV decreased by 15 ml, but the HR increased from 68 to 97, causing a SV decrease of only 0.2 L/min.

6 Discussion

6.1 Data-processing

For the UEG the filtering range of 0.5 to 30 Hz was chosen instead of up to 100 Hz as negative effects such as delays in AT were almost negligible and the decrease in the amplitude did not affect the position of the AT. Using a smaller range shortens the processing time significantly and benefits the data-processing.

In case of BEG the filtering range chosen was between 20 and 50 Hz yielding optimal conditions for T-wave detection. However, despite multiple experiments and processing methods, it was found that the T-wave has too low amplitude in BEG to be properly detected. From these results, it was concluded that the RT and ARI for the BEG cannot be accurately found and was therefore not used further in the experiments.

With respect to the PV loops, as it is not known how much blood remains in the left ventricle after a contraction, it is not possible to accurately represent the volume within the heart, but only the change in volume. Therefore, the x-axis is not comparative to most articles, but the size and shape are comparative. Another aspect to consider when comparing the PV loops to other articles is that the atrium compliance is not removed from the flow rate measurements [3][26].

6.2 Grid pacing

When pacing from the grid, the AT maps showed significant changes, with the center of activation starting in the middle and moving outwards, consistent with expectations [33]. This was observed in both UEG and BEG readings. In the 4-chamber configuration, the direction of the oval slightly shifted, but still indicated the presence of local activation.

The ARI maps displayed notable alterations in the middle of the grid compared to the baseline. The 2-chamber configuration showed higher ARI values than expected [11][12][13][14], while the 4-chamber configuration showed lower values. Some locations in both configurations exhibited higher ARI than the baseline, suggesting potential arrhythmic substrates.

For the CV maps, the highest CV typically shifted to the middle of the grid. In the 2-chamber experiments, this shift was to the middle plane. In the 4-chamber configuration, the highest CV was slightly right of center in UEG and perfectly centered in BEG. These results align with expectations that CV would peak near the pacing leads, as the larger the difference in AT, the larger the CV, and this large difference in AT occurs near the pacing site [34]. However, the results were mixed, with some cases showing varying results in intensity and type.

The PV loop during grid pacing became narrower in the 2-chamber configuration, with phases B and D almost vertical, compared to the initial more oval shape. In contrast, the 4-chamber configuration showed minimal change in the PV loop compared to the baseline. These findings suggest that pacing can potentially improve heart function but may also have no significant impact.

Discrepancies between expected and actual results may stem from grid pacing occurring on electrodes that could not be used for measurements simultaneously. Measurements however did occur on these electrodes, but deleting these results would result in a significant loss of information surrounding these electrodes, so by using smoothing algorithms, an expectation of this area was

formed. This however implies that not all experiments will yield consistent results within the electrophysiology maps due to potential over-smoothing.

6.3 2 vs 4 chamber configuration

Understanding the nuances of experimental configurations in cardiac electrophysiology and mechanics is crucial for accurately interpreting research findings. This study compared 2-chamber and 4-chamber setups to evaluate their electrophysiology, mechanical activation, and physiological behavior, testing the expectation that a whole heart setup is superior to a 2-chamber setup by analyzing various parameters.

Activation maps are critical in identifying the direction of cardiac activation propagation. While spontaneous activation patterns typically show a bottom-to-top propagation with a leftward bias, higher pacing rates can alter this pattern, often initiating activation from the left side in our case which is the direction of the pacing leads [33]. No significant differences were found between the 2-chamber and 4-chamber configurations in terms of activation patterns, suggesting that both setups are equally effective in this regard.

Comparisons between 2-chamber and 4-chamber configurations, as well as between unipolar and bipolar activation maps, show no significant differences in activation patterns over time. Each experiment displays unique activation maps and maximum length of the AT, and there is no clear evidence that the 4-chamber configuration yields superior results. The measurement method (unipolar vs. bipolar electrograms) does not significantly alter the observed activation patterns, suggesting that both setups are equally effective in this regard. Alternative methods may be more suitable for assessing the heart's physiological ranges and determining optimal configurations.

The ARI and its dispersion remained stable during the working mode, falling within physiological ranges observed in past studies (see chapter 2.1.5). Although one experiment showed higher ARI values, the overall dispersion was not significantly impactful. Both configurations showed no clear distinction over time during the first hour of working mode, indicating that they are comparably stable. This stability underscores the reliability of both setups for long-term studies, though the slightly higher values in one experiment warrant further investigation into the 4-chamber configuration. The higher values came from experiment 7 where the grid had to be substituted but was not properly glued to the arm holding it in place. This could have caused the grid to move out of place during the measurement and alter the results.

Epicardial CV results mostly fell within the expected range but occasionally reached up to 3 m/s (see chapter 2.1.5). Variability in CV results could be due to factors such as grid placement, spacing, and processing errors. The comparable results between the 2-chamber and 4-chamber setups make it challenging to identify a superior configuration. However, the grid issues observed in experiment 7 highlight the need for careful experimental design and setup optimization.

Comparison with the study by Peper et al. [35] for mechanical activation parameters revealed that our results were within the expected range but showed differences in deviation. The 2-chamber configuration exhibited smaller deviations, indicating greater stability. The PV loops in the 2-chamber setup closely resembled those in chapter 2.2, while the 4-chamber configuration showed some irregularities. It was not possible to completely close the loop in the 4-chamber configuration due to lower right heart function, resulting in high preload pressure on the right side. This increased the pressures within the surrounding tubes, potentially influencing the results from the 4-chamber setup.

However, in the 2-chamber configuration, just before the change to the 4-chamber configuration, the PV loop had a similar form, indicating that the irregularities are not only related to the 4-chamber configuration and could be due to the measurement setup. The current setup uses flow probes on the tubing and pressure catheters in the left ventricle. It is possible that some unusual flux occurs within the arteries, which will be picked up by the flow probes and can result in odd-looking PV loops. These findings suggest that while both configurations are valid, the 2-chamber setup may offer more consistent and reliable results but could still be influenced by the measurement setup.

Given the limited scope of measurements, it remains challenging to determine which configuration more accurately reflects physiological conditions. However, the consistent results from the 2-chamber experiments suggest they may provide a more reliable basis for further studies. Future research should focus on expanding the scope of measurements and addressing the observed discrepancies to enhance our understanding of the optimal experimental setup for cardiac studies.

6.4 Ion bolus

This study highlights the significant impact of ionic imbalances on cardiac electrophysiology and mechanical activation patterns. The alterations in the AT map during the calcium (Ca) bolus in the 2-chamber configuration and the counterclockwise shift in the activation pattern during the magnesium (Mg) bolus in the 4-chamber configuration suggest that ionic disturbances can lead to notable electrophysiological changes. These changes may mimic underlying pathologies such as ischemia or infarction. However, they can also be caused by conduction blocks or ectopic pacemaker activations, indicating the potential clinical relevance of these findings. The lack of significant changes with the other boluses in the 2-chamber configuration could also be the result of the grid pacing experiments prior to the boluses. The grid pacing could have contributed to creating re-entry circuits, introducing the shift in the activation patterns. Depending on the pacing duration, this re-entry could disappear within minutes or hours. In the 2-chamber configuration, this shift does not revert to the original activation pattern. It might even overpower subtle changes caused by the ion imbalance, resulting in less prominently visible electrophysiology changes and inconsistent results with respect to the literature (see chapter 2.3). These results suggest a complex interplay of factors influencing these outcomes, including the grid pacing duration.

The unexpected increase in the general ARI with the Ca bolus and the decrease with the Mg bolus in both configurations highlight discrepancies between anticipated and observed electrophysiological responses. These findings suggest that the heart's response to ionic disturbances may not always align with theoretical expectations (see chapter 2.3), necessitating further investigation. This future investigating could include the different intervals like the QRS, QT and JT intervals as mentioned in chapter 2.3, if these intervals are inline with the literature something else might influence the ARI in such a way that it is no longer in line with the initial expectations. Within the ARI maps there are high ARI areas in the 2-chamber configuration within the Ca and Mg bolus measurements with respect to the baseline and a reduction of ARI peaks after the potassium (K) bolus in the same area indicate that this area may be sensitive to specific ionic conditions. For the 4-chamber the Ca bolus seemed to improve the ARI map with no additional peaks. The Mg bolus however introduced low ARI areas, which is opposite to the peaks witnessed in the 2-chamber Mg bolus.

With respect to CV, the Ca bolus induced new high CV spots and an overall increase in CV, likely due to increased myocardial excitability. The differential effects of the Mg bolus on CV in the two configurations underscore the variability in the heart's response to ionic changes. The K bolus's effects on CV were more consistent, aligning with its known hyperkalemic effects (see chapter 2.3).

PV loop analysis further demonstrated the distinct mechanical impacts of the ionic boluses. The widening of the PV loop with the Ca bolus indicates increased contractility and potential challenges in blood ejection due to a high afterload, and the narrowing and left shift of the PV loop with the Mg bolus suggest reduced flow, lower afterload pressure and more effective blood ejection despite a decrease in contractility. The K bolus's effects on the PV loop included narrower loops, moving slightly down and to the right. All ionic bolus effects are associated with hyperkalemia, hypermagnesemia, and hypercalcemia, highlighting the heart's sensitivity to ionic interventions (see chapter 2.3).

The boluses had pronounced effects on mechanical activation parameters, which generally followed expected trends. However, electrophysiological responses were mixed, with some results aligning with expectations and others deviating or showing no effect. This inconsistency may be attributed to the short stabilization period between boluses, potentially insufficient for electrophysiological parameters to return to baseline, resulting in overlapping effects.

Moreover, the pacing from the electrode grid might have influenced the results, particularly in the 2-chamber experiments, by creating re-entry circuits and altering activation patterns. Despite these complexities, mechanical activation patterns remained largely unaffected by prior experiments, suggesting a more robust response to ionic changes.

7 Conclusion

In conclusion, the platform and measurement setup can accurately measure local activation through tests using local stimulations. Regarding the configuration, both 2-chamber and 4-chamber show physiological results suitable for long-term studies. For detecting ion imbalances, results from both electrophysiology and mechanical activation parameters combined can lead to the identification of a specific ion. While both mechanical activation parameters and electrophysiology results can be useful separately, they are even more effective when combined.

To provide more detail, the analysis of AT, ARI, and CV maps during grid pacing reveals that local activation can be effectively measured, with both 2-chamber and 4-chamber configurations showing significant changes. To avoid the loss of critical data from the pacing electrodes, a smoothing algorithm was employed, which may have resulted in slight alterations in the CV peak locations. These peaks are expected to align with the origin of the pacing. Achieving consistent and accurate results requires the ability to pace and measure electrograms at the same location, ensuring no errors in data processing. Therefore, while grid pacing is feasible for assessing local activation, meticulous experimental setup and data handling are essential to ensure reliability and accuracy.

Our findings suggest that despite some irregularities both 2-chamber and 4-chamber configurations produce comparable activation patterns and maintain stable ARI values within physiological ranges, indicating reliability for long-term studies. However, the 2-chamber configuration showed smaller deviations in mechanical activation parameters and more consistent PV loop results, suggesting more consistent and reliable results. Epicardial CV results were comparable, but grid placement issues in the 4-chamber setup highlighted the need for careful experimental design. Overall, the 2-chamber configuration is currently a more stable option, but both setups show promising results. Future research should expand measurements and address observed discrepancies for both configurations to determine the optimal configuration for cardiac studies.

In assessing ion imbalance, mechanical activation patterns clearly reflect the effects of added boluses. However, significant overlaps within the electrophysiology between different boluses complicate identifying the precise ion responsible based solely on mechanical activation or the electrophysiology. By combining the results specific ions can be identified through characteristic sets of alterations as described in Chapter 2.3 of the background. The results of the electrophysiology however diverge from the existing literature, underscoring the need for future research to explore the combined effects of mechanical activation and electrophysiology in detecting ion imbalances under better controlled conditions. However, even with the results currently found it remains feasible to associate specific ions to a set of alterations.

Mechanical activation patterns, including PV loops, demonstrate more reliable changes across experimental setups for ion boluses compared to electrophysiological responses. Conversely, in grid pacing experiments, electrophysiology results are more pronounced than mechanical activation patterns. These results emphasize the need to combine both mechanical and electrophysiological data for a comprehensive understanding of cardiac dynamics and pathology.

8 References

[1] B. Kappler, “Process and quality control in use of isolated beating porcine slaugtherhouse hearts,” 2020. doi: 10.13140/RG.2.2.23299.25121.

[2] J. Egido *et al.*, “Animal models of cardiovascular diseases,” *Journal of Biomedicine and Biotechnology*, vol. 2011. 2011. doi: 10.1155/2011/497841.

[3] R. E. Klabunde, *Cardiovascular Physiology Concepts*, 3rd ed. Wolters Kluwer, 2021.

[4] Z. Murphy, *Cardiovascular | Electrophysiology | Intrinsic Cardiac Conduction System*, (2017). Accessed: May 01, 2024. [Online Video]. Available: https://www.youtube.com/watch?v=1kX6Tp8CWFw&t=2525s&ab_channel=NinjaNerd

[5] Z. Murphy, *Cardiovascular | Electrophysiology | Extrinsic Cardiac Conduction System*, (2017). Accessed: May 27, 2024. [Online Video]. Available: https://www.youtube.com/watch?v=2L4FbEEsy1s&ab_channel=NinjaNerd

[6] Z. Murphy, *EKG Basics | How to Read & Interpret EKGs: Updated Lecture*, (2022). Accessed: May 01, 2024. [Online Video]. Available: https://www.youtube.com/watch?v=CNN30YHsJw0&t=3907s&ab_channel=NinjaNerd

[7] Mayo Clinic, “EP study.” Accessed: May 01, 2024. [Online]. Available: https://www.mayoclinic.org/tests-procedures/ep-study/about/pac-20384999

[8] J. M. T. de Bakker, “Electrogram recording and analyzing techniques to optimize selection of target sites for ablation of cardiac arrhythmias,” *PACE - Pacing and Clinical Electrophysiology*, vol. 42, no. 12. Blackwell Publishing Inc., pp. 1503–1516, Dec. 01, 2019. doi: 10.1111/pace.13817.

[9] Z. F. Issa, J. M. (John M. Miller, and D. P. Zipes, *Clinical arrhythmology and electrophysiology : a companion to Braunwald’s heart disease*.

[10] T. Kinoshita *et al.*, “Activation recovery interval as an electrocardiographic repolarization index to detect doxorubicin-induced cardiotoxicity,” *J Cardiol*, vol. 82, no. 6, pp. 473–480, Dec. 2023, doi: 10.1016/j.jjcc.2023.07.006.

[11] T. Yang, L. Yu, Q. Jin, L. Wu, and B. He, “Activation recovery interval imaging of premature ventricular contraction,” *PLoS One*, vol. 13, no. 6, Jun. 2018, doi: 10.1371/journal.pone.0196916.

[12] X. Zhou *et al.*, “In Vivo and in Silico Investigation into Mechanisms of Frequency Dependence of Repolarization Alternans in Human Ventricular Cardiomyocytes,” *Circ Res*, vol. 118, no. 2, pp. 266–278, Jan. 2016, doi: 10.1161/CIRCRESAHA.115.307836.

[13] S. Ghosh, E. K. Rhee, J. N. Avari, P. K. Woodard, and Y. Rudy, “Cardiac memory in patients with Wolff-Parkinson-White syndrome: Noninvasive imaging of activation and repolarization before and after catheter ablation,” *Circulation*, vol. 118, no. 9, pp. 907–915, Aug. 2008, doi: 10.1161/CIRCULATIONAHA.108.781658.

[14] L. Gepstein, G. Hayam, and S. A. Ben-Haim, “Activation-Repolarization Coupling in the Normal Swine Endocardium,” *Circulation*, vol. 96, no. 11, pp. 4036–4043, 1997, doi: 10.1161/01.CIR.96.11.4036.

[15] W. W. Good *et al.*, “Estimation and Validation of Cardiac Conduction Velocity and Wavefront Reconstruction Using Epicardial and Volumetric Data.” [Online]. Available: http://www.sci.utah.edu/cibc-

[16] B. Abdi, M. S. van Schie, N. M. S. de Groot, and R. C. Hendriks, “Analyzing the effect of electrode size on electrogram and activation map properties,” *Comput Biol Med*, vol. 134, Jul. 2021, doi: 10.1016/j.compbiomed.2021.104467.

[17] M. Rodrigo, P. Ganesan, R. Feng, S. Ruiperez-Campillo, S. M. Narayan, and V. V. Fedorov, “PO-03-097 DEFINING ELECTRODE CONFIGURATION FOR MAPPING MICROANATOMIC REENTRIES SUSTAINING ATRIAL FIBRILLATION,” *Heart Rhythm*, vol. 20, no. 5, pp. S462–S463, May 2023, doi: 10.1016/j.hrthm.2023.03.1010.

[18] M. Beheshti *et al.*, “Determinants of atrial bipolar voltage: Inter electrode distance and wavefront angle,” *Comput Biol Med*, vol. 102, pp. 449–457, Nov. 2018, doi: 10.1016/j.compbiomed.2018.07.011.

[19] M. Takigawa *et al.*, “Detailed Analysis of the Relation Between Bipolar Electrode Spacing and Far- and Near-Field Electrograms,” *JACC Clin Electrophysiol*, vol. 5, no. 1, pp. 66–77, Jan. 2019, doi: 10.1016/j.jacep.2018.08.022.

[20] M. J. Letchumy *et al.*, “The Effects of Electrode Configuration on Omnipolar Electrograms: An In-Silico Approach,” in *Computing in Cardiology*, IEEE Computer Society, 2022. doi: 10.22489/CinC.2022.247.

[21] K. Magtibay *et al.*, “Physiological assessment of ventricular myocardial voltage using omnipolar electrograms,” *J Am Heart Assoc*, vol. 6, no. 8, Aug. 2017, doi: 10.1161/JAHA.117.006447.

[22] M. S. Van Schie *et al.*, “Identification of Low-Voltage Areas: A Unipolar, Bipolar, and Omnipolar Perspective,” *Circ Arrhythm Electrophysiol*, vol. 14, no. 7, p. E009912, Jul. 2021, doi: 10.1161/CIRCEP.121.009912.

[23] S. M. Blanchard, W. M. Smith, W. C. Buhrman, R. E. Ideker, and J. E. Lowe, “COMPUTED BIPOLAR ELECTROGRAMS FROM UNIPOLAR EPICARDIAL RECORDINGS,” *Proceedings. Computers in Cardiology 1988*, pp. 55–60, 1988, doi: 10.1109/CIC.1988.72566.

[24] R. Starreveld *et al.*, “The Impact of Filter Settings on Morphology of Unipolar Fibrillation Potentials,” *J Cardiovasc Transl Res*, vol. 13, no. 6, pp. 953–964, Dec. 2020, doi: 10.1007/s12265-020-10011-w.

[25] B. Kappler *et al.*, “Investigating the physiology of normothermic ex vivo heart perfusion in an isolated slaughterhouse porcine model used for device testing and training,” *BMC Cardiovasc Disord*, vol. 19, no. 1, Nov. 2019, doi: 10.1186/s12872-019-1242-9.

[26] A. Goodwill, “Introduction to PV loops: Understanding points on the PV loop and measures of cardiac function,” AD instruments. Accessed: May 01, 2024. [Online]. Available: https://www.adinstruments.com/blog/introduction-pv-loops-understanding-points-pv-loop-and-measures-cardiac-function

[27] R. Noordam *et al.*, “Effects of Calcium, Magnesium, and Potassium Concentrations on Ventricular Repolarization in Unselected Individuals,” *J Am Coll Cardiol*, vol. 73, no. 24, pp. 3118–3131, Jun. 2019, doi: 10.1016/j.jacc.2019.03.519.

[28] L. J. Drop and D. Scheidegger, “Plasma ionized calcium concentration: Important determinant of the hemodynamic response to calcium infusion,” *Journal of Thoracic and Cardiovascular Surgery*, vol. 79, no. 3, pp. 425–431, 1980, doi: 10.1016/s0022-5223(19)37951-6.

[29] D. Kolte, K. Vijayaraghavan, S. Khera, D. A. Sica, and W. H. Frishman, “Role of magnesium in cardiovascular diseases,” *Cardiology in Review*, vol. 22, no. 4. Lippincott Williams and Wilkins, pp. 182–192, 2014. doi: 10.1097/CRD.0000000000000003.

[30] J. N. Weiss, Z. Qu, and K. Shivkumar, “Electrophysiology of hypokalemia and hyperkalemia,” *Circ Arrhythm Electrophysiol*, vol. 10, no. 3, Mar. 2017, doi: 10.1161/CIRCEP.116.004667.

[31] S. Aziz, S. Ahmed, and M. S. Alouini, “ECG-based machine-learning algorithms for heartbeat classification,” *Sci Rep*, vol. 11, no. 1, Dec. 2021, doi: 10.1038/s41598-021-97118-5.

[32] C. D. Cantwell, C. H. Roney, F. S. Ng, J. H. Siggers, S. J. Sherwin, and N. S. Peters, “Techniques for automated local activation time annotation and conduction velocity estimation in cardiac mapping,” *Comput Biol Med*, vol. 65, pp. 229–242, Oct. 2015, doi: 10.1016/j.compbiomed.2015.04.027.

[33] P. Vijayaraman, P. Bordachar, and K. A. Ellenbogen, “The Continued Search for Physiological Pacing Where Are We Now?,” 2017.

[34] J. I. Laughner, F. S. Ng, M. S. Sulkin, R. Martin Arthur, and I. R. Efimov, “Processing and analysis of cardiac optical mapping data obtained with potentiometric dyes,” *American Journal of Physiology - Heart and Circulatory Physiology*, vol. 303, no. 7. Oct. 01, 2012. doi: 10.1152/ajpheart.00404.2012.

[35] E. S. Peper *et al.*, “An isolated beating pig heart platform for a comprehensive evaluation of intracardiac blood flow with 4D flow MRI: a feasibility study,” *Eur Radiol Exp*, vol. 3, no. 1, Dec. 2019, doi: 10.1186/s41747-019-0114-5.

[36] OpenStax, *Anatomy and Physiology 2e*. Texas: Rice University, 2022. Accessed: Jul. 02, 2024. [Online]. Available: https://assets.openstax.org/oscms-prodcms/media/documents/Anatomy_and_Physiology_2e_-_WEB_c9nD9QL.pdf

[37] K. Gjesdal, M. Bjaanes, and M. Korseberg Stokke, “From the action potential to the ECG,” University of Oslo. Accessed: May 01, 2024. [Online]. Available: https://studmed.uio.no/elaring/fag/hjertesykdommer/index_en.shtml

[38] P. G. Krushna, P. Pravati, and N. Nivedita, “Electrophysiology of the Heart,” in *Comprehensive Textbook of Medical Physiology*, vol. 2, Jaypee Brothers Medical Publishers (P) Ltd., 2017.

[39] A. Davies, “Recognizing and reducing interference on 12-lead electrocardiograms.,” *British journal of nursing (Mark Allen Publishing)*, vol. 16, no. 13. pp. 800–804, 2007. doi: 10.12968/bjon.2007.16.13.24245.

[40] K. Gjesdal, M. Bjaanes, and M. Korseberg Stokke, “Practical electrophysiology,” University of Oslo. Accessed: May 01, 2024. [Online]. Available: https://studmed.uio.no/elaring/fag/hjertesykdommer/index_en.shtml

[41] Thoracickey, “The Cardiac Conduction System.” Accessed: May 01, 2024. [Online]. Available: https://thoracickey.com/the-cardiac-conduction-system/

9 Appendix

9.1 Basic knowledge

9.1.1 Electrophysiology

Electrophysiology is the study of electrical properties of biological cells and tissue. When focused on the heart, it becomes cardiac electrophysiology. This field examines the heart's electrical activity, including how electrical signals control heartbeats. Key aspects of cardiac electrophysiology include understanding action potentials, ion channels, the heart's conduction system, diagnosing arrhythmias, and employing diagnostic techniques like Electrocardiography (ECG) and electrophysiological studies (EPS).

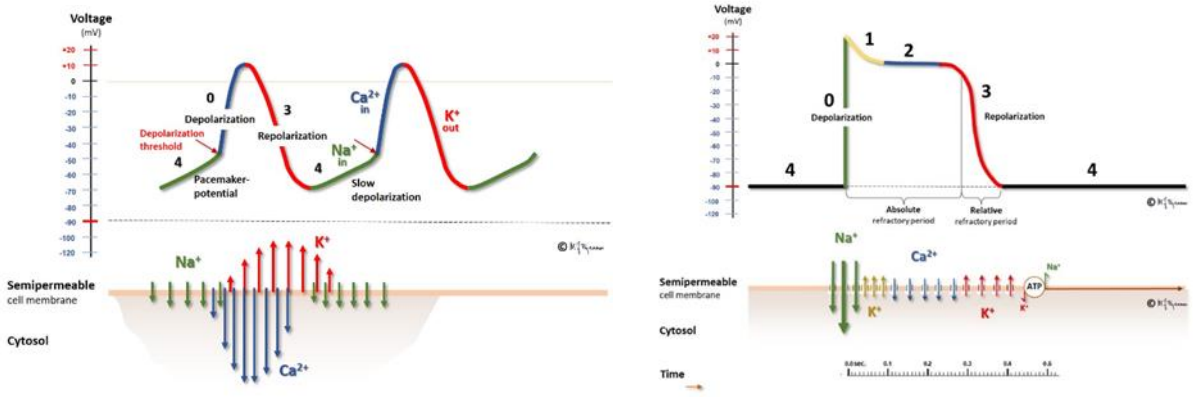

The heart's conduction system [4]

The heart's intrinsic cardiac conduction system, also known as the natural pacemaker of the heart, coordinates its rhythm and contraction. The heart has the intrinsic ability to spontaneously depolarize and trigger action potentials that are spread out over the entire myocardium, the muscle layer of the heart, to trigger the heart muscle to contract. The myocardium consists of two components: the nodal cells and the contractile cells. The nodal cells are non-contractile cells that can intrinsically polarize, generate action potentials, and trigger the contraction of the heart. The SA node, AV node, Bundle of His, bundle branches, and the Purkinje fibers all consist of nodal cells. The nodal cells are connected to each other through gap junctions, which make it possible for positive ions to pass from one cell to the other. Similar connections exist between the nodal cells and the contractile cells, which will be explained later.

The creation of action potentials [4]

Initially, sodium starts to flow into the nodal cell through the funny sodium channels, increasing the potential from -60 mV to -55 mV. Once the potential reaches around -55 mV, T-type calcium channels start to open, further increasing the potential until the depolarization threshold is reached. Once the depolarization threshold is reached, the L-type calcium channels open, causing the inside of the cell to become increasingly positive, resulting in a positive potential of around 10 to 40 mV depending on the location of the nodal cell, fully depolarizing the cell. To ensure that depolarization also occurs within the contractile cells, the cells are connected through gap junctions. Through these gap junctions, positive cations flow from the nodal cell to nodal cell, but also into the contractile cell. This brings the action potential in the contractile cell from -90 mV to -70 mV, also known as the threshold potential. Once the threshold potential is reached, the voltage-gated sodium channels rapidly open, and sodium ions rush into the cell, rapidly depolarizing the cell membrane. This will cause the membrane potential to go from -70 mV to 10 mV, known as depolarization. Along the way, calcium channels already start to open, only a small amount, causing calcium to flow into the contractile cell. This step is called phase 0.

After phase 0, the sodium channels completely close, and potassium channels start to open. As potassium ions flow out of the contractile cell at a higher rate than the calcium ions are flowing in, the membrane potential decreases from 10 mV to 0 mV. This is phase 1. At 0mV, the voltage-gated calcium channels become a little bit sensitive and start to open even more, allowing more calcium ions to enter the cell. The amount of calcium ions that are coming in will become the same as the potassium ions that are coming out. The cell will be maintained in a partially depolarized state known as the plateau phase, also known as phase 2. Additionally, calcium triggers the release of more calcium ions from the sarcoplasmic reticulum by binding to so-called ryanodine receptors. These receptors open the channels that release more calcium into the cell. The amount of calcium will increase even further, but at the same time bind to a special protein called troponin. Troponin changes the tropomyosin in the muscle cells and causes more cross-bridges to form between myosin and actin, causing more muscle contraction resulting in the pumping of the heart initiating muscle contraction. Due to the gap junctions, all the cells are connected, and all the muscle cells will depolarize at around the same time. They synchronize their action to where they contract as a unit, so either the myocardium contracts or it does not.

Once the contraction has taken place, potassium channels open in the nodal cell, and potassium ions exit the nodal cells. This will decrease the action potential in the nodal cell from around 10-40 mV back to -60 mV. Once the resting membrane potential is reached, the potassium channels will close, and the funny sodium channels will open, and the action potential repeats itself. Because the nodal cell becomes more negative, fewer positive cations flow into the contractile cell. The contractile cell has reached its plateau phase, and the L-type calcium channels start closing, and the calcium ions flow back into the sarcoplasmic reticulum through calcium proton ATPases, which is a primary active transport, and through sodium-calcium exchangers, which is a secondary active transport. The calcium is also extracted out of the cell into the extracellular environment by the same means as the calcium flowing into the sarcoplasmic reticulum through primary and secondary active transport. The potassium channels will open even further, and the potassium ions will rapidly exit the contractile cell, repolarizing the membrane potential and restoring the resting state. This will cause the membrane action potential to go from approximately 0mV back to -90mV, marking phase 3.

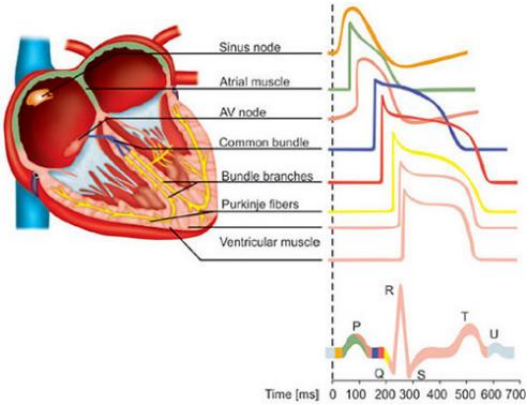

After repolarization, cardiac muscle cells enter a refractory period, phase 4, during which they cannot respond to additional stimuli. This period ensures sufficient time for the heart muscle to relax and refill with blood before the next contraction cycle begins. During this phase the original chemical gradients is restored, meaning that the sodium and calcium that previously went into the cell will come out of the cell and the potassium will flow back into the cell, either through leakage or through primary and secondary active transport. The different phases of the membrane potential in a nodal cell at the SA node are shown in Figure 1 and for the contractile cell are shown in Figure 2.

For the nodal cell, an example was provided concerning the action potential of the SA node. However, the action potential varies along the conduction pathway. Figure 3 illustrates the differences in the action potential along this pathway until the action potential of the contractile cells is reached. The various phases of the cardiac action potential together correspond to the surface ECG. Specifically, the P wave reflects atrial depolarization, the PR interval represents the CV through the AV node, the

QRS complex signifies ventricular depolarization, and the QT interval indicates the duration of ventricular action potential. In Figure 3 the different colors show which action potential has the most influence on the ECG and in which regions. Basically, by adding all the different action potentials together a surface ECG is formed.

ECG wavefroms

A standard ECG comprises 12 different leads: three limb leads, three augmented unipolar limb leads (aVR, aVL, and aVF), and six precordial or chest leads (V1 to V6) from 10 different electrode, which are placed on the limbs and on the chest. Each lead displays distinct patterns. Figure 5 provides examples of the RS complex of the precordial or chest leads, while Figure 4 illustrates the placement of the positive electrode in relation to the heart.

The precordial or chest leads are particularly significant as they offer valuable insights into pathology. These leads are unipolar limb leads, featuring only one positive electrode positioned on the chest at various regions, as depicted in Figure 4. The electrode's placement provides insights into specific regions of the heart. For instance, leads V1 to V3 offer information about the right ventricle, V2-V3 about the basal septum, V2-V4 about the anterior wall of the heart, and V5-V6 about the lateral wall of the left ventricle.

The most notable differences between ECG waveforms lie in the R and S waves. The Q wave, while sometimes present, is not as crucial because its visibility varies. However, in leads V1 to V3, significant Q waves should not be observed. Therefore, the focus lies on the R and S waves. The R-wave represents the upward deflection, while the S-wave denotes the downward deflection following the R-wave (refer to Figure 3). During ventricular depolarization, a small R-wave vector for the right ventricle and a larger left ventricular vector are generated outwardly.

Comparing this to the electrode locations reveals a smaller R-wave vector in V1, primarily indicating the right ventricle. Conversely, due to the larger left ventricular vector, the R-wave vector in V6 should be significantly larger (see Figure 5). The S-wave results from depolarization of the bases, moving away from the electrodes, leading to a downward deflection in the ECG. From V1 to V6, the downward deflection diminishes until it is almost non-existent, as V6's direction is nearly perpendicular to the bases. In summary, the R-wave increases in magnitude from V1 to V6, while the S-wave decreases, as illustrated in Figure 5.

9.2 Activation and Recovery times

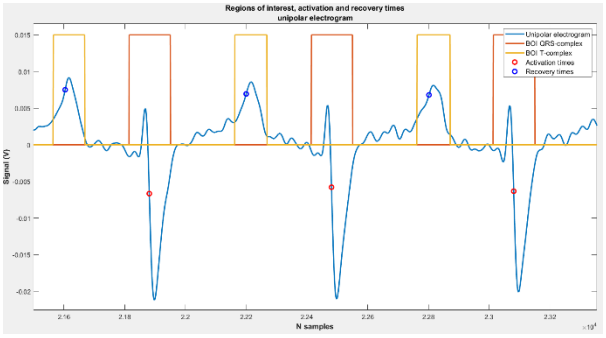

Figure A1 Blocks of interest for the QRS and T complex shown in red and yellow. The resulting AT (red dots) and RT (blue dots). These results are established from a unipolar electrogram from electrode 7 during experiment 5.

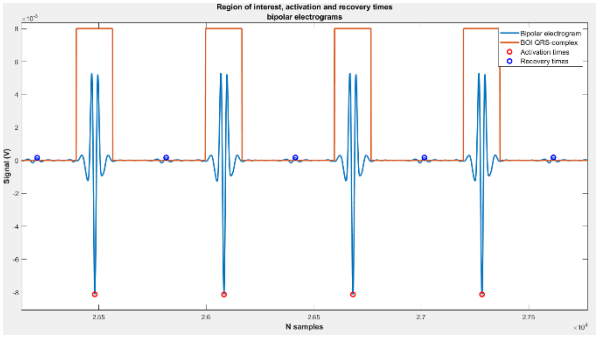

Figure A2: Block of interest for QRS complex shown in red. The resulting AT (red dots) and the RT (blue dots). These results are established from a bipolar electrogram from electrode 7 and 15 on the electrode grid during experiment 5.

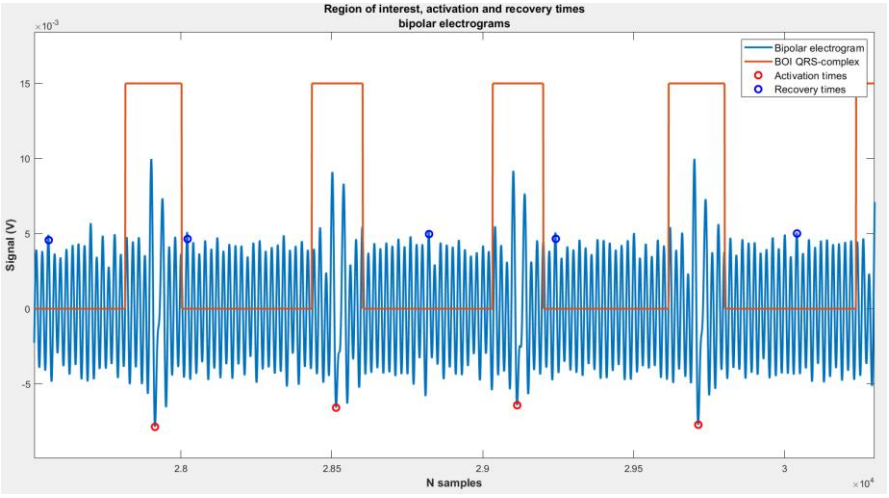

Figure A3 Block of interest for QRS-complex (red line) and the resulting activation (red dot) and RT (blue dot). These results are established from a bipolar electrogram from electrodes 34 and 42 on the electrode grid during experiment 5.

9.3 Activation maps

9.3.1 2-chamber configuration

Unipolar electrograms

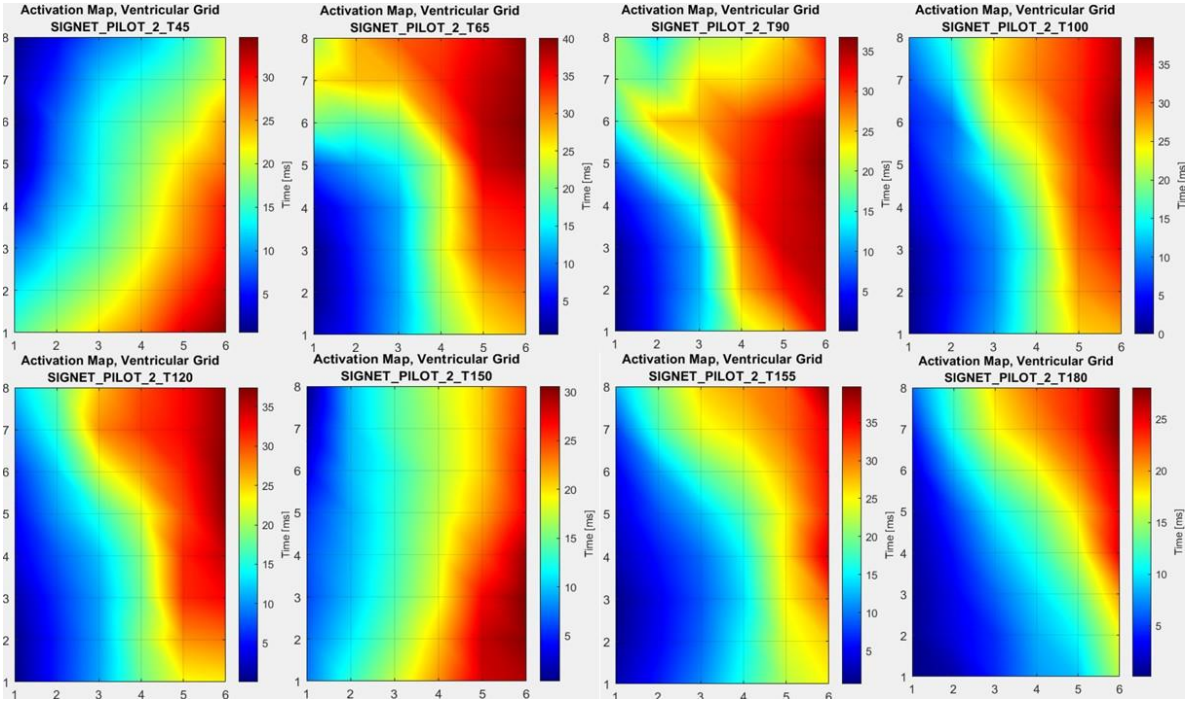

Figure A4: Unipolar electrograms activation maps. At the top row from left to right the activation maps are shown during different moment of an experiment. In the top left the activation map during Langendorff mode is shown and afterwards the platform was changed to working mode. The other maps represent the changes in the activation map along the experiment. In this experiment 7 measurements were taken during working mode.

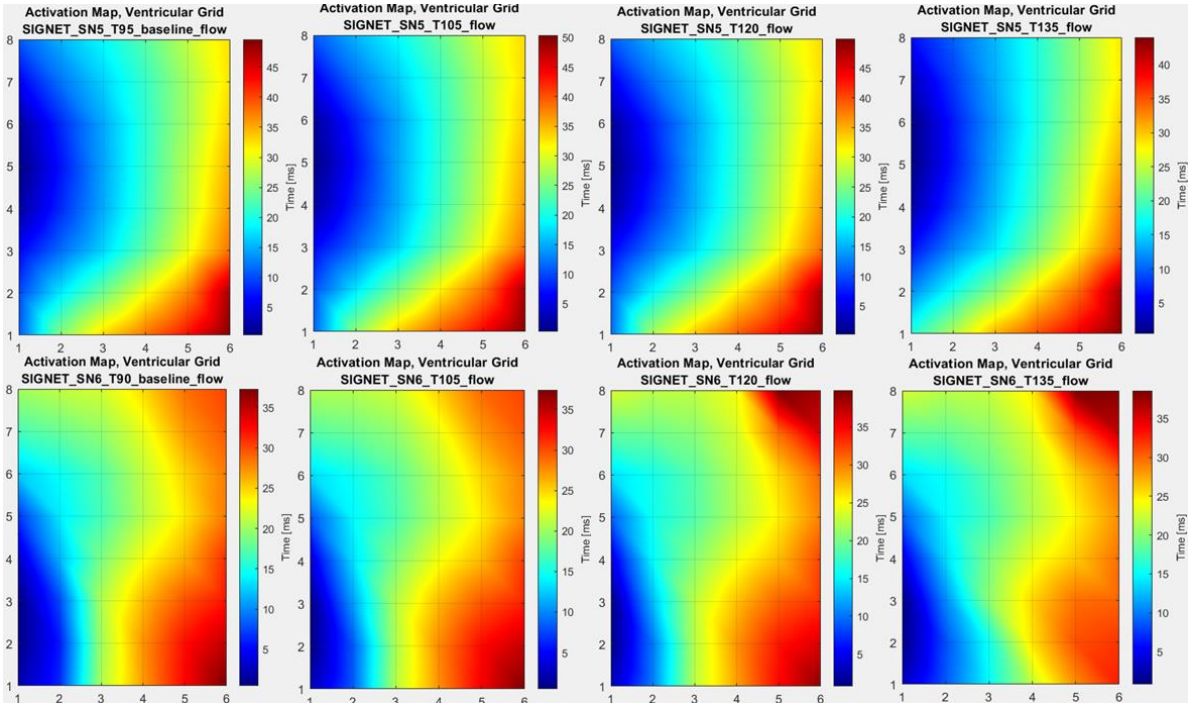

Figure A5: Unipolar electrogram activation maps. At the top row from left to right the activation maps are shown during different moment of the working mode for one experiment. On the bottom row the activation maps are shown also during working mode for a different experiment.

Bipolar electrograms

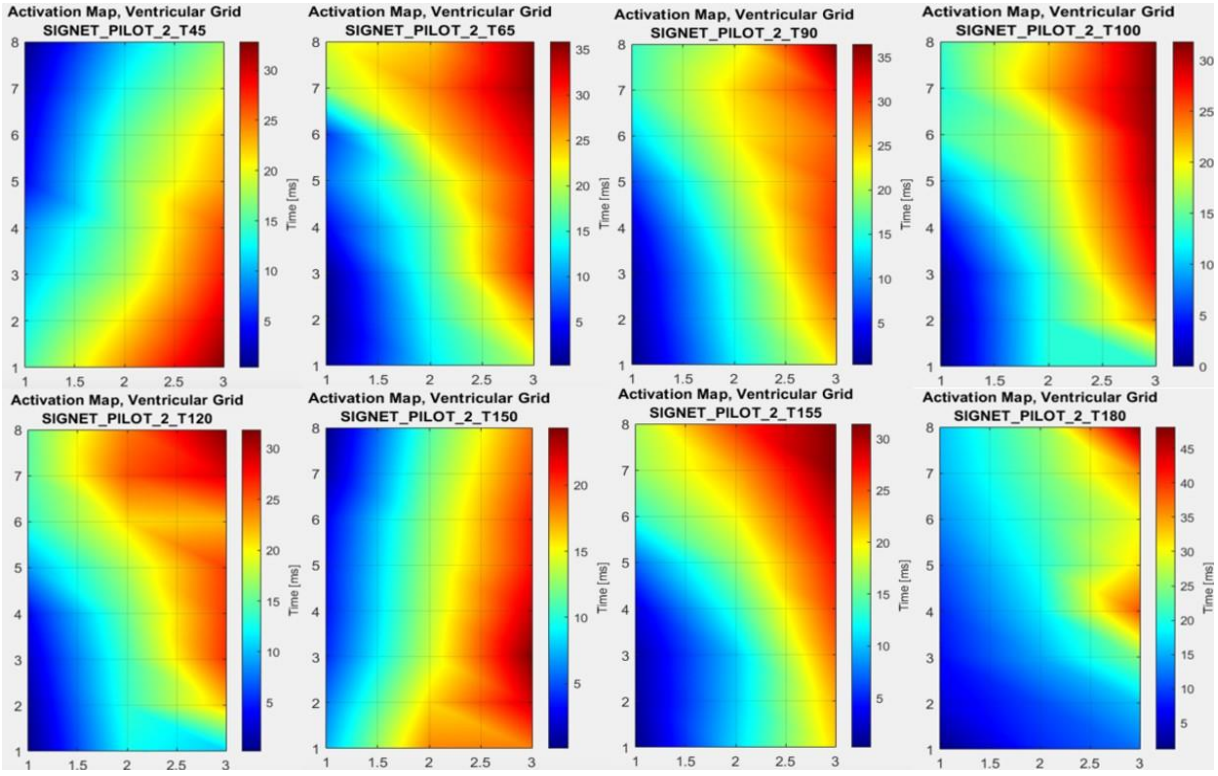

Figure A6: Bipolar electrograms activation maps. At the top row from left to right the activation maps are shown during different moment of an experiment. In the top left the activation map during Langendorff mode is shown and afterwards the platform was changed to working mode. The other maps represent the changes in the activation map along the experiment. In this experiment 7 measurements were taken during working mode.

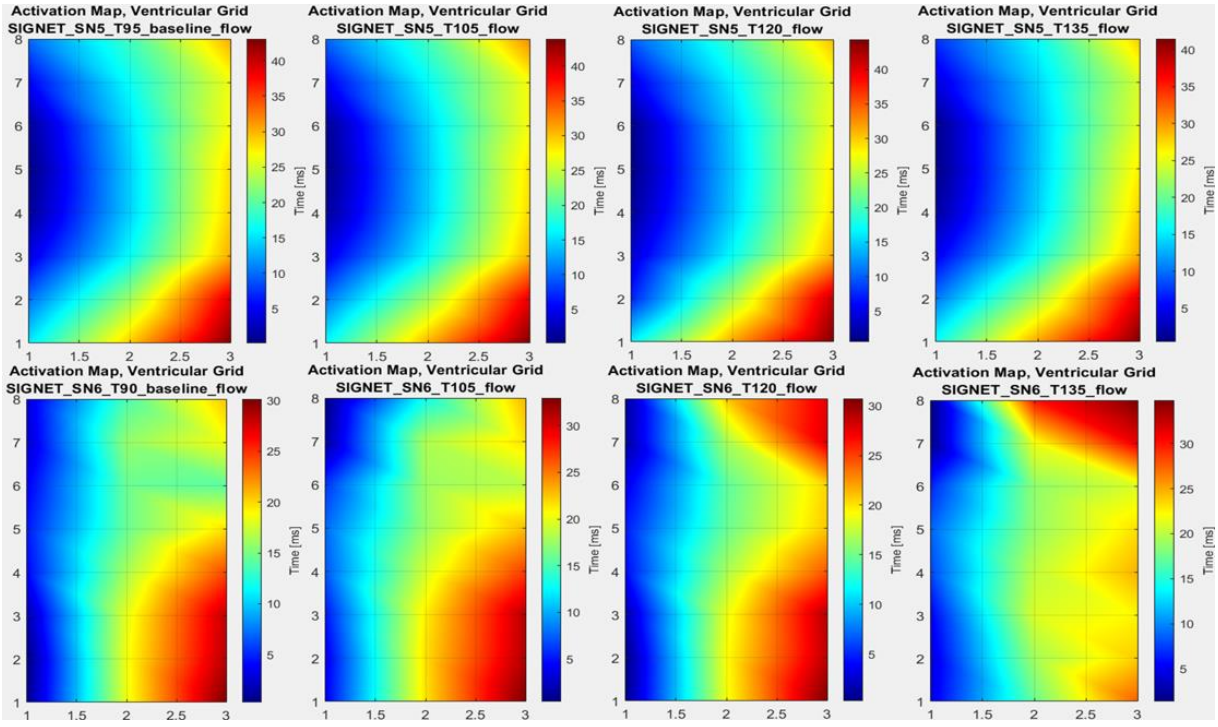

Figure A7: Bipolar electrogram activation maps. At the top row from left to right the activation maps are shown during different moments of the working mode for one experiment. On the bottom row the activation maps are shown also during working mode for a different experiment.

9.3.2 4-chamber configuration

Unipolar electrograms

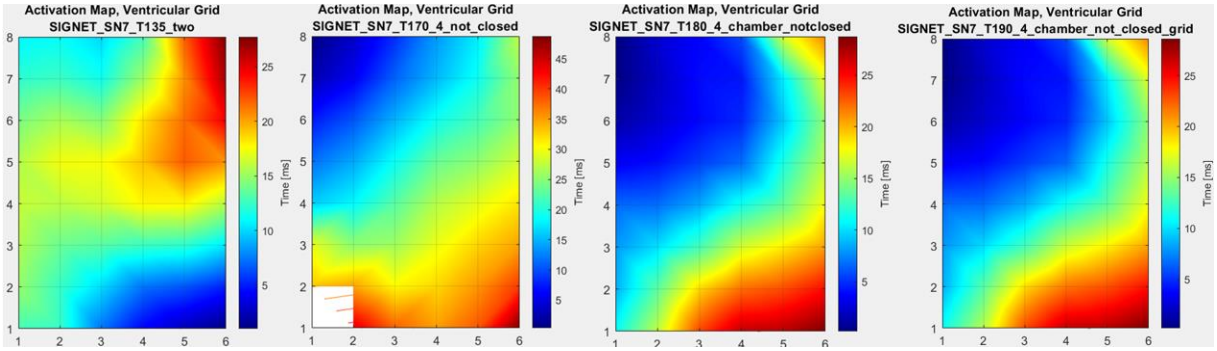

Figure A8: Unipolar electrograms activation maps. From the left to right the activation maps are shown during different moments of the working mode for one experiment. In the first map on the left a measurement in a two-chamber configuration is shown and the next three maps are all in a 4-chamber configuration at different timestamps.

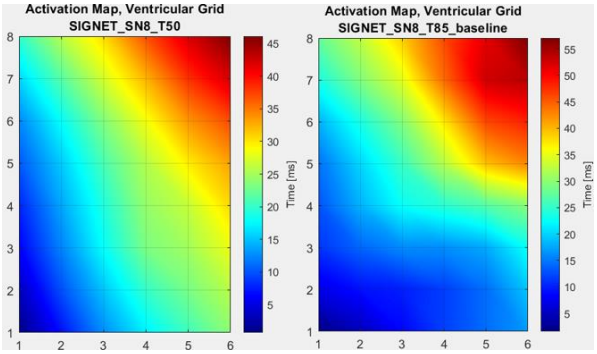

Figure A9: Unipolar electrogram activation maps. On the left map an activation map is shown during Langendorff and to the right an activation map during working mode in a 4-chamber configuration.

9.4 Activation recovery interval

9.4.1 2-chamber configuration

Unipolar electrograms

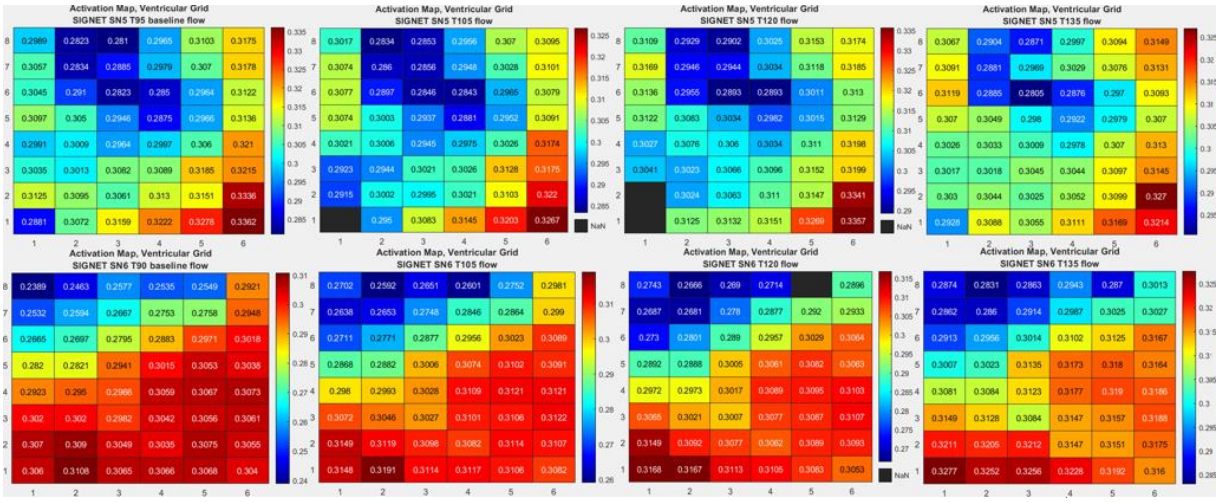

Figure A10: ARI maps of the mean ARI from every unipolar electrogram during a 2-chamber configuration. In this Figure 8 maps are shown from the top left to the top right the maps from experiment 5 are shown during working mode and from the bottom left to bottom right the maps from experiment 6 are shown during working mode at multiple timestamps.

Bipolar electrograms

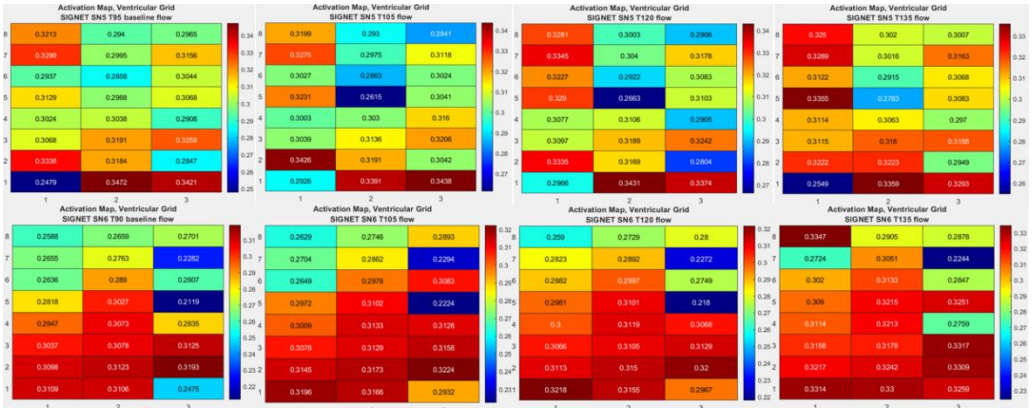

Figure A11: ARI maps of the mean ARI from every bipolar electrogram during a 2-chamber configuration. In this Figure 8 maps are shown from the top left to the top right the maps from experiment 5 are shown during working mode and from the bottom left to bottom right the maps from experiment 6 are shown during working mode at multiple timestamps.

9.4.2 4-chamber configuration

Unipolar electrograms

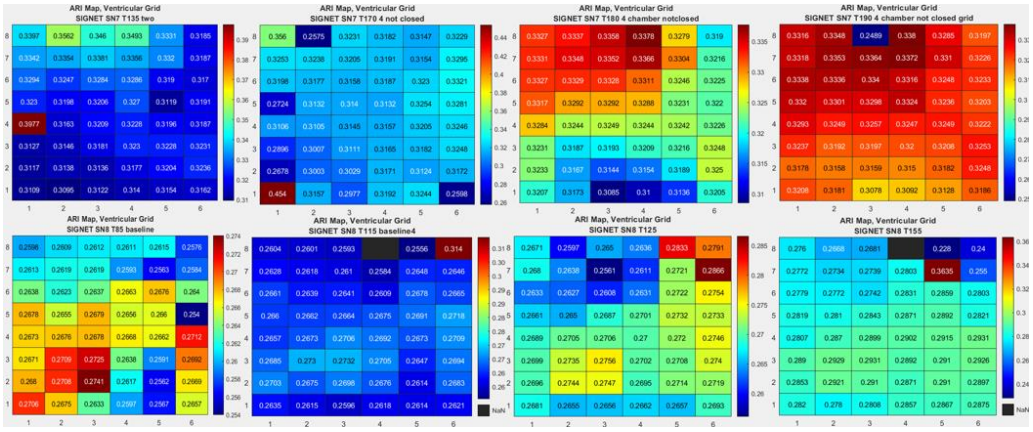

Figure A12: ARI maps of the mean ARI from every unipolar electrogram during a 4-chamber configuration. In this Figure 8 maps are shown from the top left to the top right the maps from experiment 7 are shown during working mode and from the bottom left to bottom right the maps from experiment 8 are shown during working mode at multiple timestamps.

Bipolar electrograms

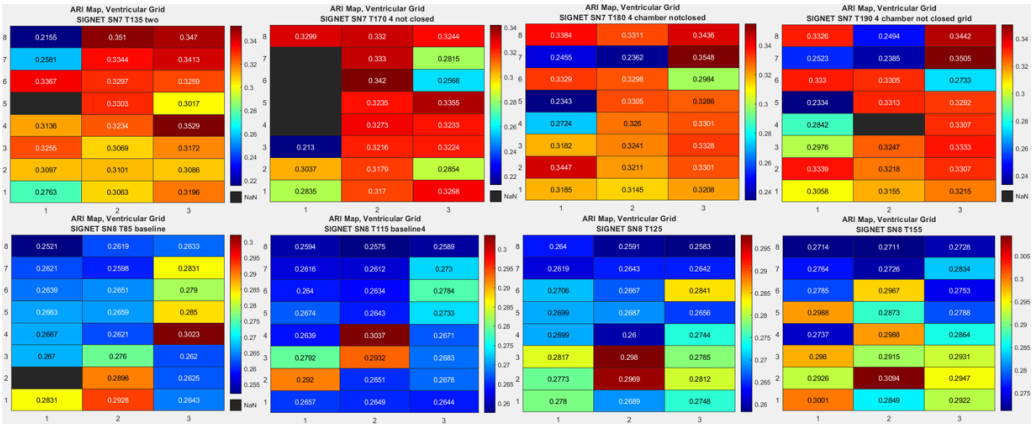

Figure A13: ARI maps of the mean ARI from every bipolar electrogram during a 4 chamber configuration. In this Figure 8 maps are shown from the top left to the top right the maps from experiment 7 are shown during working mode and from the bottom left to bottom right the maps from experiment 8 are shown during working mode at multiple timestamps.

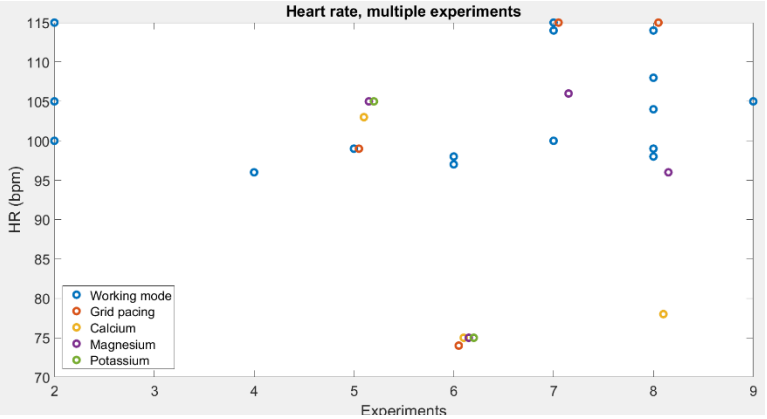

Figure A14: The difference in heart rate during the experiments. During working mode (blue), grid pacing (red), calcium bolus (yellow), magnesium bolus (purple) and potassium bolus (green)

9.5 The mode and standard deviation of the activation recovery interval

9.5.1 2-chamber configuration

Table 6: ARI mode (most frequently found) and standard deviation with respect to the mode for all experiments in a 2-chamber configuration using the unipolar electrograms. The measurements shown are all during working mode.

ARI from unipolar electrograms - 2 chamber configuration						
Experiment 2	**ARI mode**	**ARI std**		**Experiment 4**	**ARI mode**	**ARI std**
T100	0.3100	0.0338		**T75**	0.2650	0.0273
T120	0.3150	0.0253		**T90**	0.2650	0.0255
T150	0.3100	0.0398		**T105**	0.2650	0.0266
T180	0.3150	0.0370		**T120**	0.2750	0.0255
Experiment 5	**ARI mode**	**ARI std**		**Experiment 6**	**ARI mode**	**ARI std**
T95	0.3105	0.0162		**T90**	0.3075	0.0263
T105	0.3025	0.0126		**T105**	0.3125	0.0231
T120	0.3125	0.0130		**T120**	0.3075	0.0176
T135	0.3025	0.0178		**T135**	0.3175	0.0144
				T150	0.3225	0.0149
Experiment 9	**ARI mode**	**ARI std**				
T90	0.2985	0.0145				
T105	0.2925	0.0136				
T120	0.3025	0.0187				

Table 7: ARI mode (most frequently found) and standard deviation with respect to the mode for all experiments in a 2-chamber configuration using the bipolar electrograms. The measurements shown are all during working mode.

ARI from bipolar electrograms - 2 chamber configuration						
Experiment 2	**ARI mode**	**ARI std**		**Experiment 4**	**ARI mode**	**ARI std**
T100	0.3480	0.0423		**T75**	0.2993	0.0361
T120	0.3561	0.0395		**T90**	0.2993	0.0370
T150	0.3196	0.0322		**T105**	0.2993	0.0359
T180	0.3155	0.0369		**T120**	0.3034	0.0297
Experiment 5	**ARI mode**	**ARI std**		**Experiment 6**	**ARI mode**	**ARI std**
T95	0.3074	0.0270		**T90**	0.3115	0.0378
T105	0.3034	0.0197		**T105**	0.3155	0.0361
T120	0.3115	0.0209		**T120**	0.3115	0.0310
T135	0.3074	0.0282		**T135**	0.3236	0.0259
				T150	0.3236	0.0283
Experiment 9	**ARI mode**	**ARI std**				
T90	0.3034	0.0173				
T105	0.2993	0.0180				
T120	0.2993	0.0240				

9.5.2 4-chamber configuration

Table 8: ARI mode (most frequently found) and standard deviation with respect to the mode for all experiments in a 4-chamber configuration using the unipolar electrograms. The measurements shown are all during working mode.

ARI from unipolar electrograms - 4 chamber configuration						
Experiment 7	**ARI mode**	**ARI std**		**Experiment 8**	**ARI mode**	**ARI std**
two T135	0.3195	0.0131		**two T85**	0.2665	0.0046
four T170	0.3175	0.0192		**four T115**	0.2670	0.0056
T180	0.3225	0.0126		**T125**	0.2675	0.0177
T190	0.3230	0.0077		**T140**	0.2725	0.0127
				T155	0.2910	0.0079
				T170	0.2875	0.0186

Table 9: ARI mode (most frequently found) and standard deviation with respect to the mode for all experiments in a 4-chamber configuration using the bipolar electrograms. The measurements shown are all during working mode.

ARI from bipolar electrograms - 4 chamber configuration						
Experiment 7	**ARI mode**	**ARI std**		**Experiment 8**	**ARI mode**	**ARI std**
two T135	0.3318	0.03298		**two T85**	0.2628	0.0160
four T170	0.3236	0.02353		**four T115**	0.2628	0.0133
T180	0.3318	0.03295		**T125**	0.2669	0.0195
T190	0.3318	0.03678		**T140**	0.2669	0.0207
				T155	0.2750	0.0135
				T170	0.2831	0.0167

9.6 Conduction velocity maps

9.6.1 2-chamber configurations

Unipolar electrograms

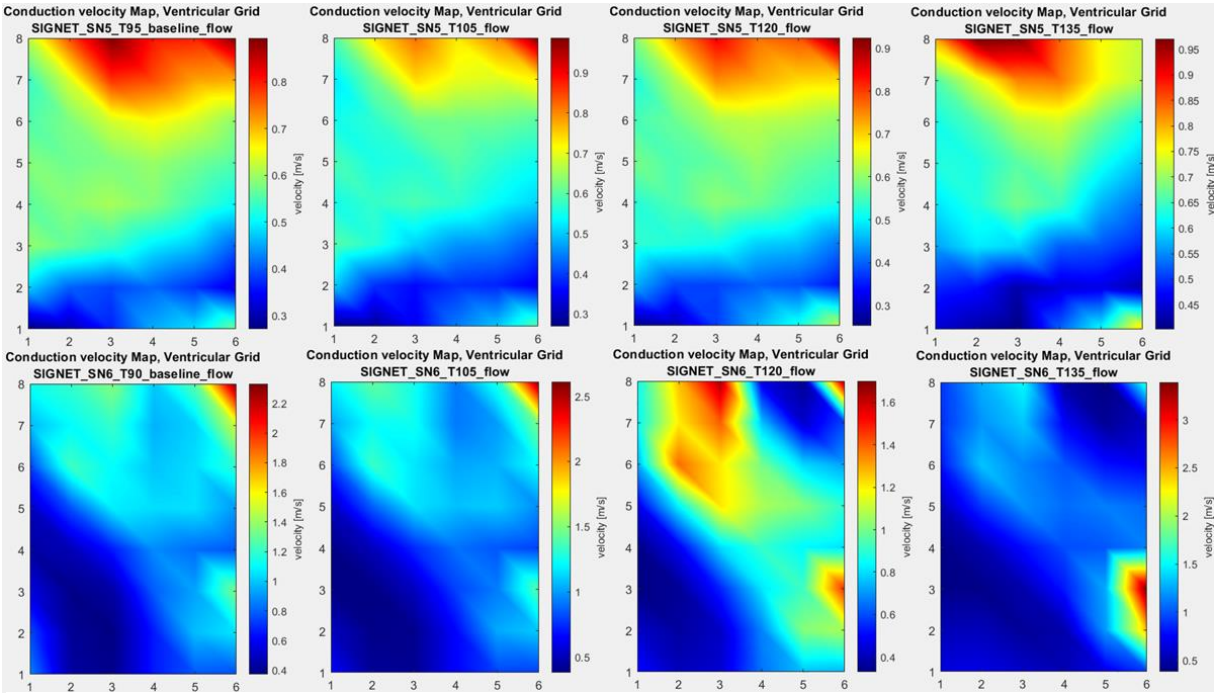

Figure A15: CV maps from the unipolar electrograms during a 2-chamber configuration. In this Figure the maps on the top row are from experiment 5 and the experiments on the bottom row are from experiment 6 during working mode at multiple timestamps.

Bipolar electrograms

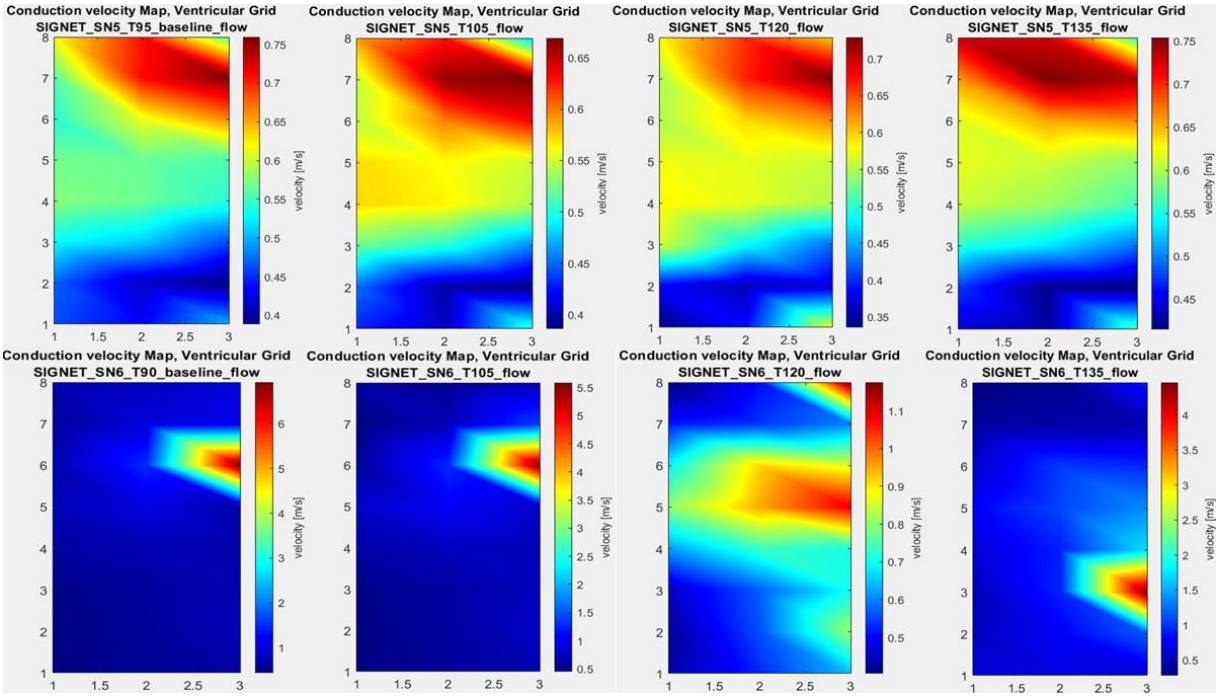

Figure A16: CV maps from the bipolar electrograms during a 2-chamber configuration. In this Figure the maps on the top row are from experiment 5 and the experiments on the bottom row are from experiment 6 during working mode at multiple timestamps.

9.6.2 4-chamber configuration

Unipolar electrograms

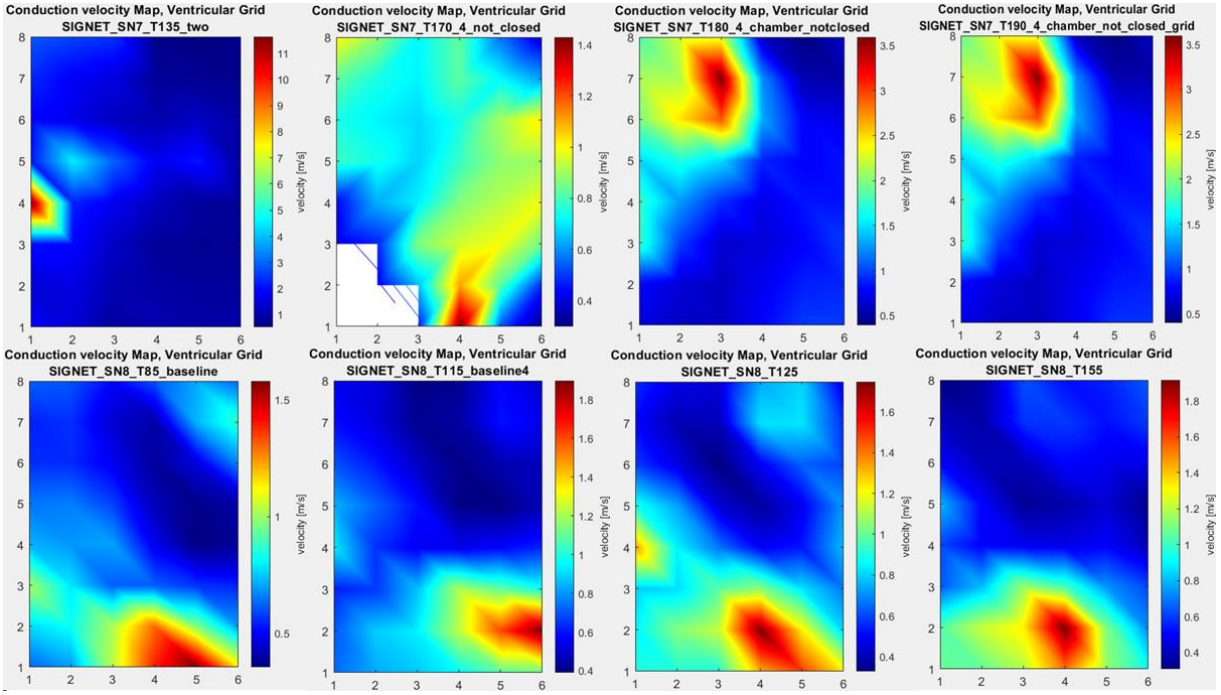

Figure A17: CV maps from the unipolar electrograms during a 4-chamber configuration. In this Figure the maps on the top row are from experiment 7 and the experiments on the bottom row are from experiment 8 during working mode at multiple timestamps.

Bipolar electrograms

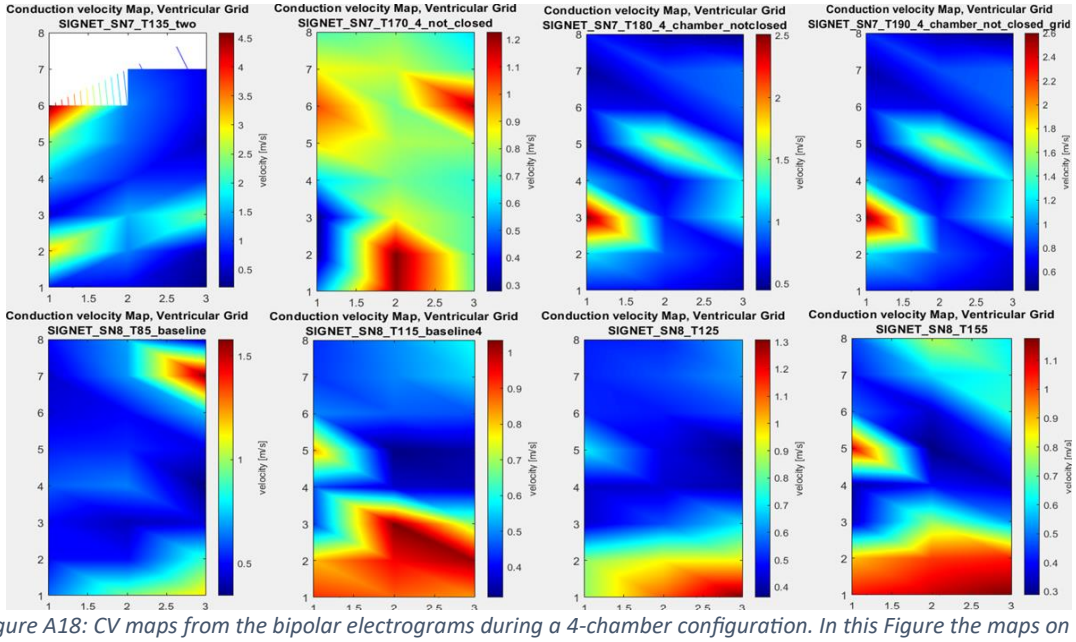

Figure A18: CV maps from the bipolar electrograms during a 4-chamber configuration. In this Figure the maps on the top row are from experiment 5 and the experiments on the bottom row are from experiment 6 during working mode at multiple timestamps.

9.7 Mean and Ranges of the conduction velocity

9.7.1 2-chamber configuration

Table 10: Mean and range of the CV from the unipolar electrograms using the 2-chamber configuration. The range is determined as 90% of the total amount of data points present, so from 5% to 95% of an ordered CV range. From this range the mean was taken as the data set is too small to identify the mode.

CV from unipolar electrograms - 2 chamber configuration						
Experiment 2	**CV mean (90% CI)**	**CV range (90%)**		**Experiment 4**	**CV mean (90%CI)**	**CV range (90%CI)**
T100	0.6857	0.4022-1.0687		**T75**	0.8258	0.5586-1.4114
T120	0.6992	0.4174-1.1518		**T90**	0.8436	0.5939-1.2718
T150	0.8710	0.5770-1.3258		**T105**	0.8673	0.5953-1.4338
T180	0.9347	0.5139-1.6961		**T120**	0.8808	0.6112-1.3457
Experiment 5	**CV mean (90%CI)**	**CV range (90%CI)**		**Experiment 6**	**CV mean (90%CI)**	**CV range (90%CI)**
T95	0.5670	0.3263-0.8140		**T90**	0.8796	0.3886-1.3707
T105	0.5558	0.3399-0.8022		**T105**	0.8976	0.3926-1.4355
T120	0.5565	0.3392-0.7939		**T120**	0.7932	0.3530-1.4899
T135	0.6261	0.4232-0.8559		**T135**	0.8576	0.3994-1.7459
				T150	0.9891	0.4430-1.9849
Experiment 9	**CV mean (90%CI)**	**CV range (90%CI)**				
T90	1.2188	0.8063-3.0286				
T105	0.9395	0.3790-1.5402				
T120	0.9933	0.7624-1.5615				

Table 11: Mean and range of the CV from the bipolar electrograms using the 2-chamber configuration. The range is determined as 90% of the total amount of data points present, so from 5% to 95% of an ordered CV range. From this range the mean was taken as the data set is too small to identify the mode.

CV from bipolar electrograms - 2 chamber configuration						
Experiment 2	**CV mean (90%CI)**	**CV range (90%CI)**		**Experiment 4**	**CV mean (90%CI)**	**CV range (90%CI)**
T100	0.6978	0.4308-1.2636		**T75**	0.8051	0.6009-1.5794
T120	0.7707	0.4153-1.7620		**T90**	0.8757	0.4982-4.6774
T150	0.8485	0.7125-1.0453		**T105**	0.8325	0.6339-1.9709
T180	0.8878	0.7415-1.2253		**T120**	0.8480	0.6470-2.0292
Experiment 5	**CV mean (90%CI)**	**CV range (90%CI)**		**Experiment 6**	**CV mean (90%CI)**	**CV range (90%CI)**
T95	0.5506	0.4064-0.7243		**T90**	0.7660	0.4463-3.1215
T105	0.5322	0.3931-0.6639		**T105**	0.7270	0.4495-1.6448
T120	0.5705	0.3618-0.7033		**T120**	0.6664	0.4176-1.1170
T135	0.5841	0.4176-0.7428		**T135**	0.7917	0.3222-2.5452
				T150	0.7672	0.3781-1.3708
Experiment 9	**CV mean (90%CI)**	**CV range (90%CI)**				
T90	1.0626	0.5931-2.5197				
T105	0.9618	0.7569-1.7032				
T120	0.9842	0.7493-1.5681				

9.7.2 4-chamber configuration

Table 12: Mean and range of the CV from the unipolar electrograms using the 4-chamber configuration. The range is determined as 90% of the total amount of data points present, so from 5% to 95% of an ordered CV range. From this range the mean was taken as the data set is too small to identify the mode.

CV from unipolar electrograms - 4 chamber configuration						
Experiment 7	**CV mean (90%CI)**	**CV range (90%CI)**		**Experiment 8**	**CV mean (90%CI)**	**CV range (90%CI)**
two T135	1.3966	0.6365-3.0748		**two T85**	0.6653	0.3818-1.3108
four T170	0.7434	0.4092-1.0419		**four T115**	0.6934	0.3976-1.2693
T180	1.1209	0.5326-2.0076		**T125**	0.7523	0.3907-1.3605
T190	1.1335	0.5402-2.5520		**T140**	0.6697	0.3467-1.4759
				T155	0.6753	0.3376-1.3537
				T170	0.7955	0.3691-1.6906

Table 13: Mean and range of the CV from the bipolar electrograms using the 4-chamber configuration. The range is determined as 90% of the total amount of data points present, so from 5% to 95% of an ordered CV range. From this range the mean was taken as the data set is too small to identify the mode.

CV from bipolar electrograms - 4 chamber configuration						
Experiment 7	**CV mean (90%CI)**	**CV range (90%CI)**		**Experiment 8**	**CV mean (90%CI)**	**CV range (90%CI)**
two T135	1.1646	0.2787-3.8096		**two T85**	0.5980	0.3914-1.2798
four T170	0.7677	0.2833-1.2138		**four T115**	0.6046	0.3321-1.0200
T180	0.8239	0.4865-1.8513		**T125**	0.6208	0.3869-1.1665
T190	0.8331	0.4983-1.8919		**T140**	0.8317	0.2534-1.4362
				T155	0.6503	0.3083-1.1339
				T170	0.8658	0.2843-2.0842

9.8 Pressure-volume loops – working mode

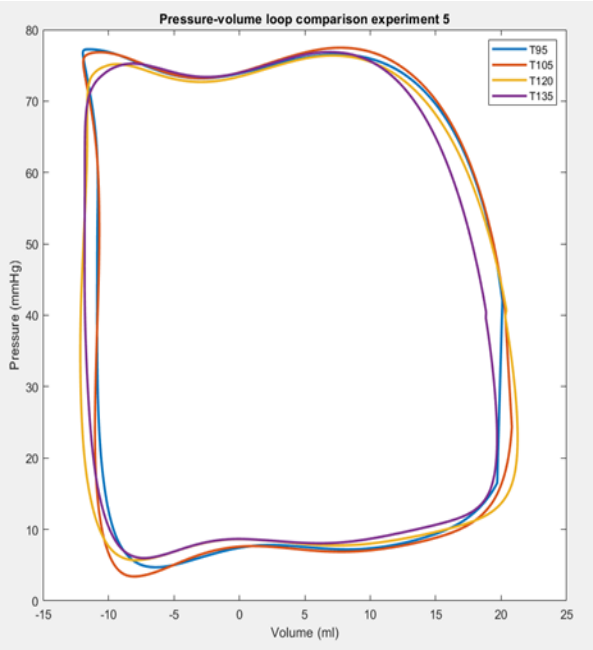

Figure A19: PV loops of experiment 5 during working mode in a 2-chamber configuration.

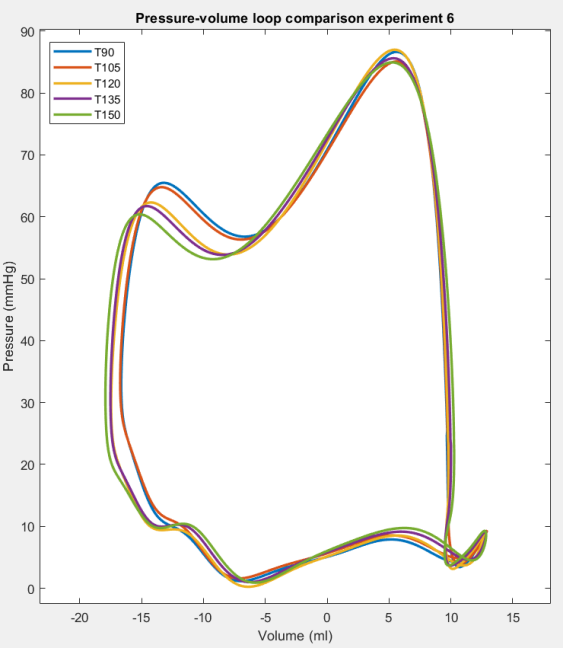

Figure A20: PV loops of experiment 6 during working mode in a 2-chamber configuration.

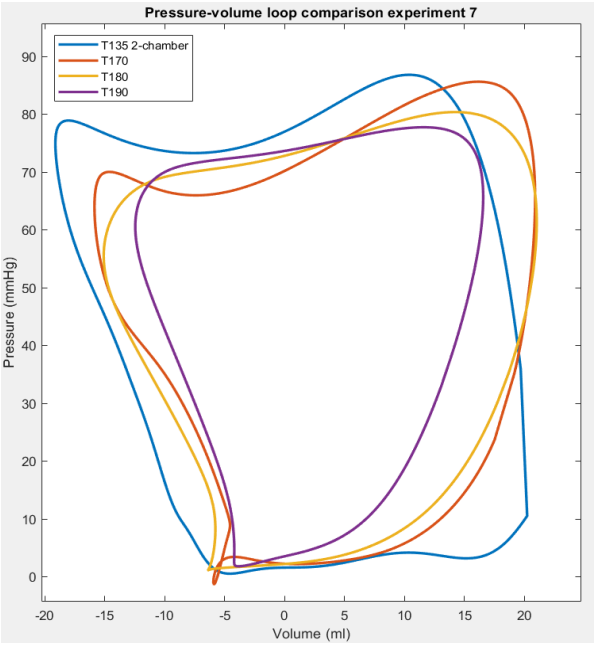

Figure A21: PV loops of experiment 7 during working mode in a 4-chamber configuration. The blue line indicates the loop in a 2-chamber configuration just before the change to 4. Directly afterwards large changes can be observed in the PV loop.

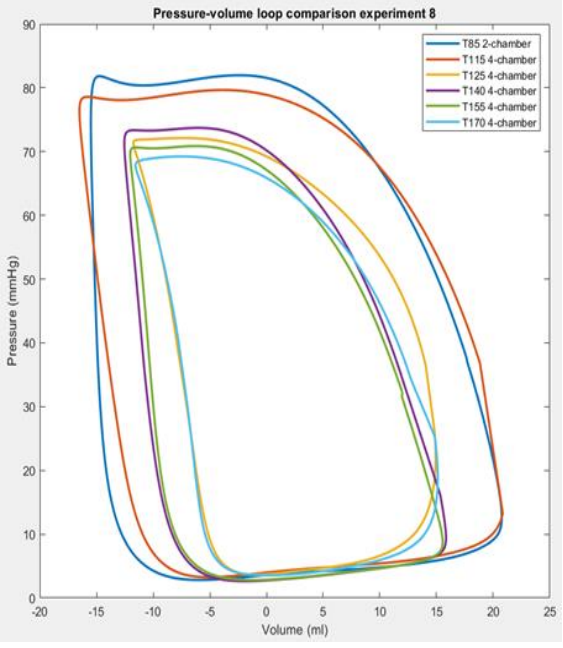

Figure A22: PV loops of experiment 8 during working mode in a 4-chamber configuration. The blue line indicates the loop in a 2-chamber configuration just before change and at T125 a large shift in PV loop can be observed.

9.9 Grid pacing

9.9.1 4-chamber configuration

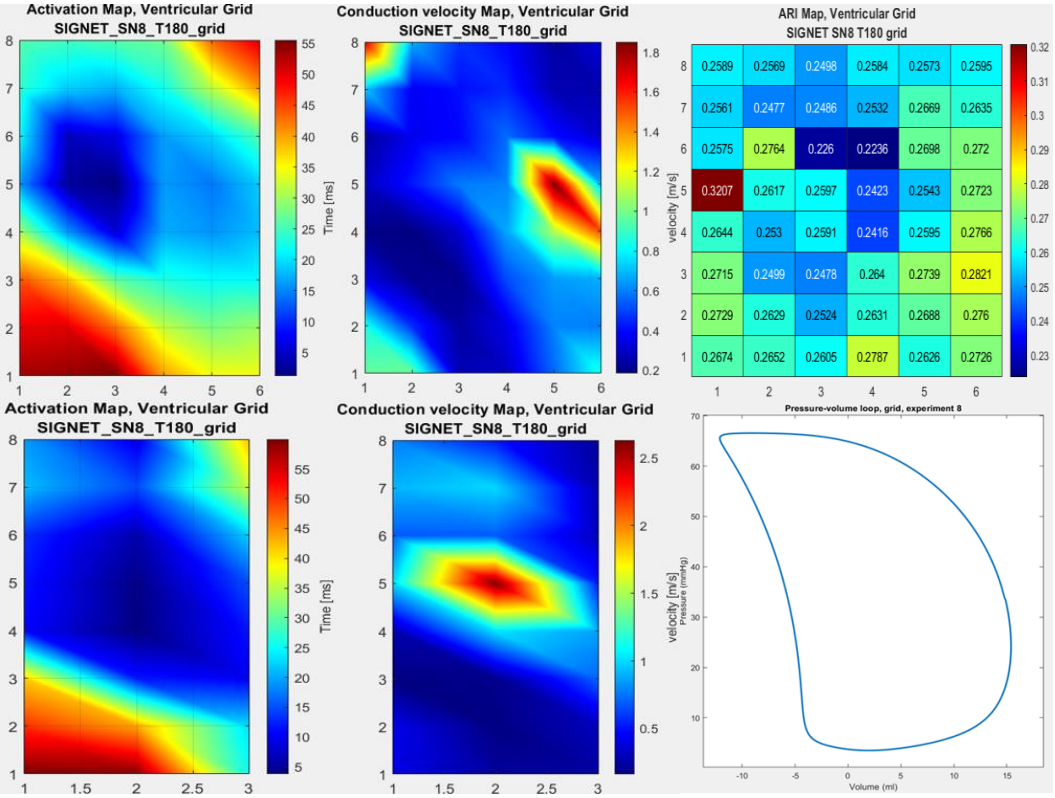

Figure A23: Top row from left to right, activation map, CV map and ARI map from the unipolar electrograms. Bottom row from left to right, activation map and CV map from the bipolar electrograms and the last figure contains the PV-loops during pacing on the grid. These figures represent the results from experiment 8 during 4-chamber configuration.

9.9.2 Pressure-volume loops

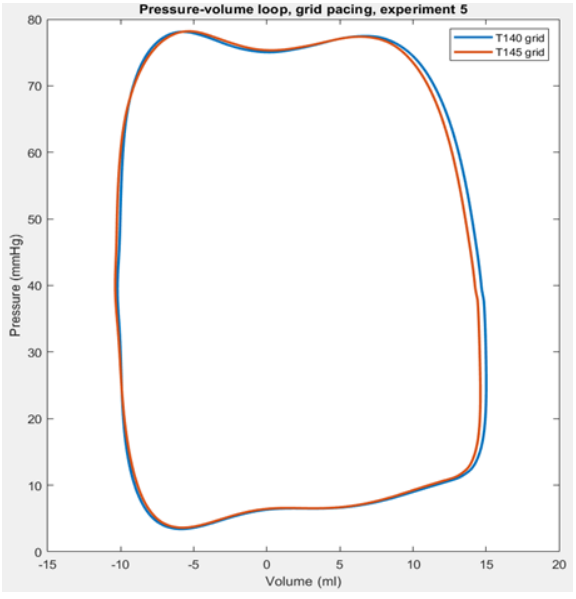

Figure A24: PV loops of grid pacing from experiment 5 in a 2-chamber configuration.

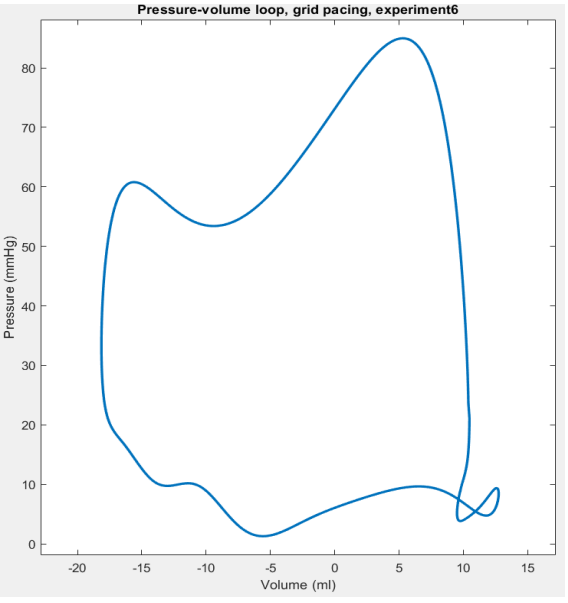

Figure A25: PV loop op grid pacing from experiment 6 in a 2-chamber configuration.

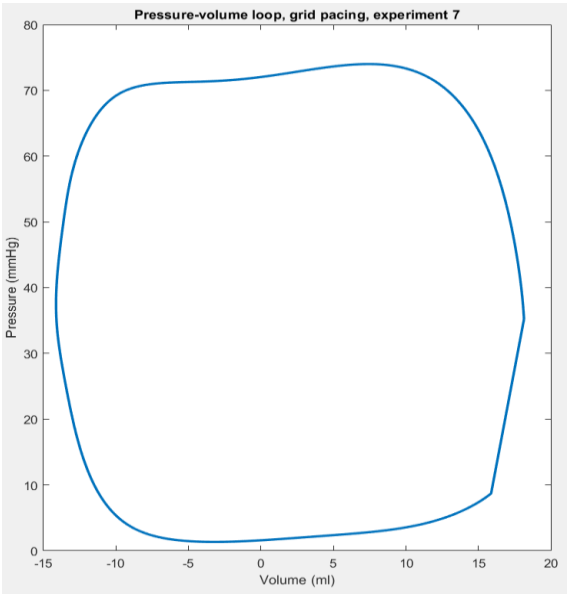

Figure A26: PV loop of grid pacing from experiment 7 in a 4-chamber configuration.

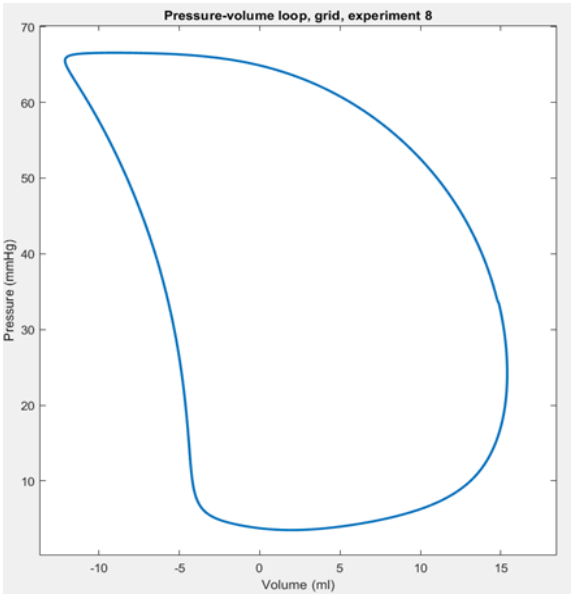

Figure A27: PVloop of grid pacing from experiment 8 in a 4-chamber configuration.

9.10 Ion bolus

Calcium bolus

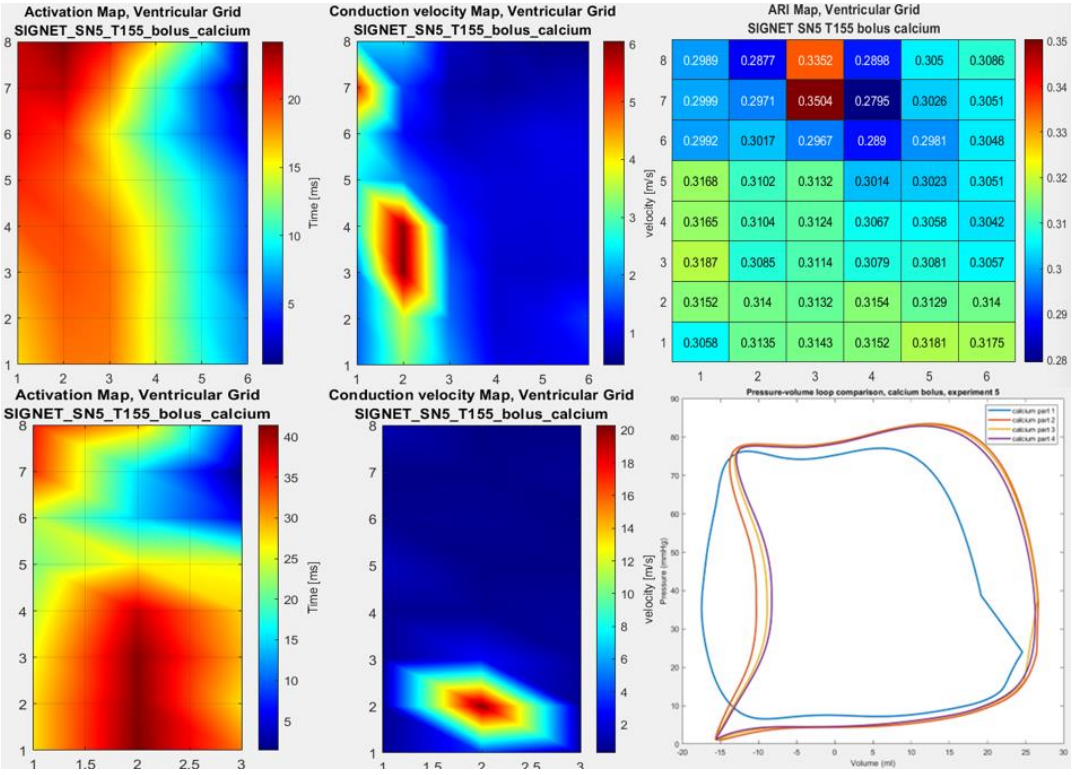

Figure A28: Top row from left to right, activation map, CV map and ARI map from the unipolar electrograms. Bottom row from left to right, activation map and CV map from the bipolar electrograms and the last figure contains the PV-loops during a calcium bolus. These figures represent the results from experiment 5 during 2-chamber configuration.

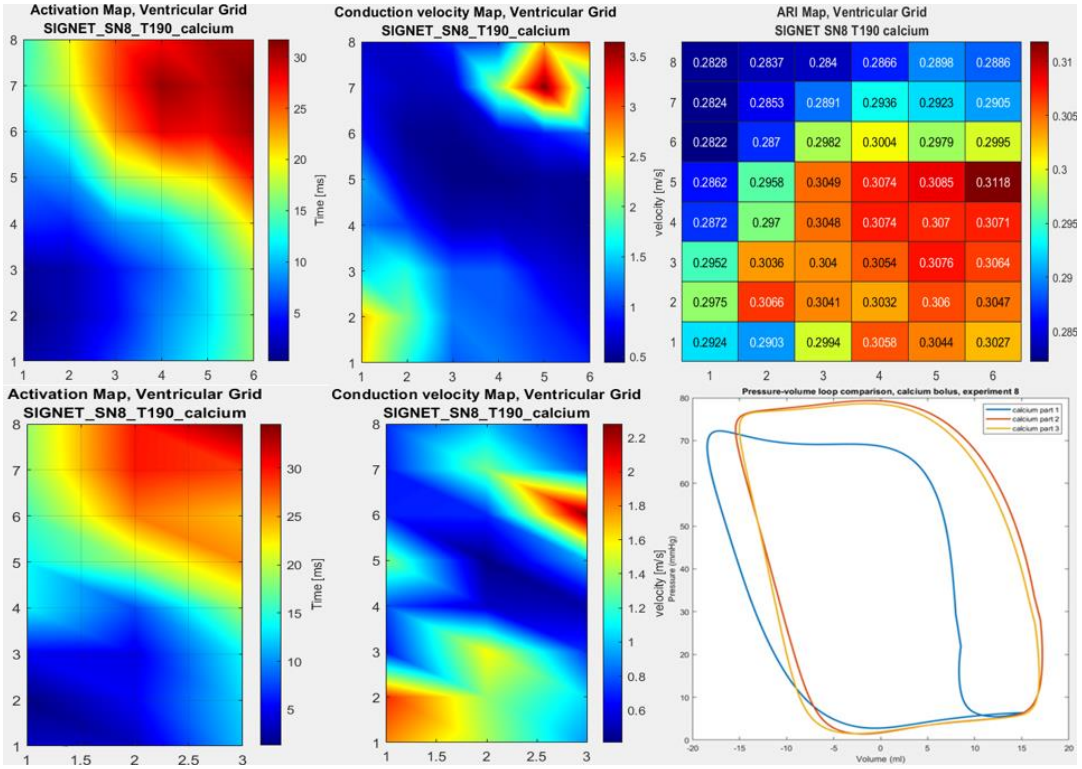

Figure A29: Top row from left to right, activation map, CV map and ARI map from the unipolar electrograms. Bottom row from left to right, activation map and CV map from the bipolar electrograms and the last figure contains the PV-loops during a calcium bolus. These figures represent the results from experiment 8 during 4-chamber configuration.

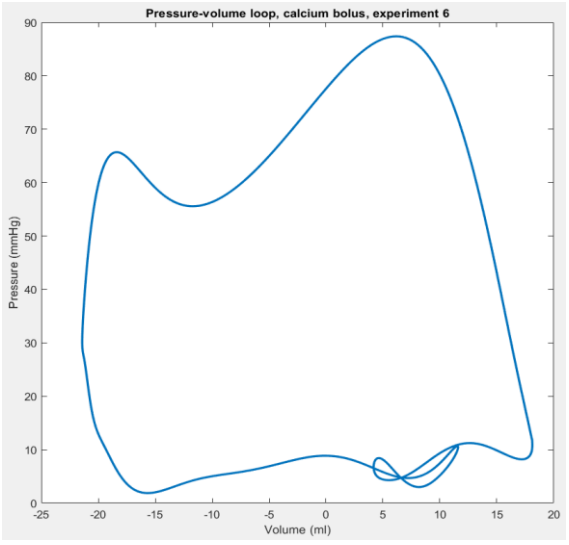

Figure A30: PV loop of a calcium bolus from experiment 6 in a 2-chamber configuration.

Magnesium bolus

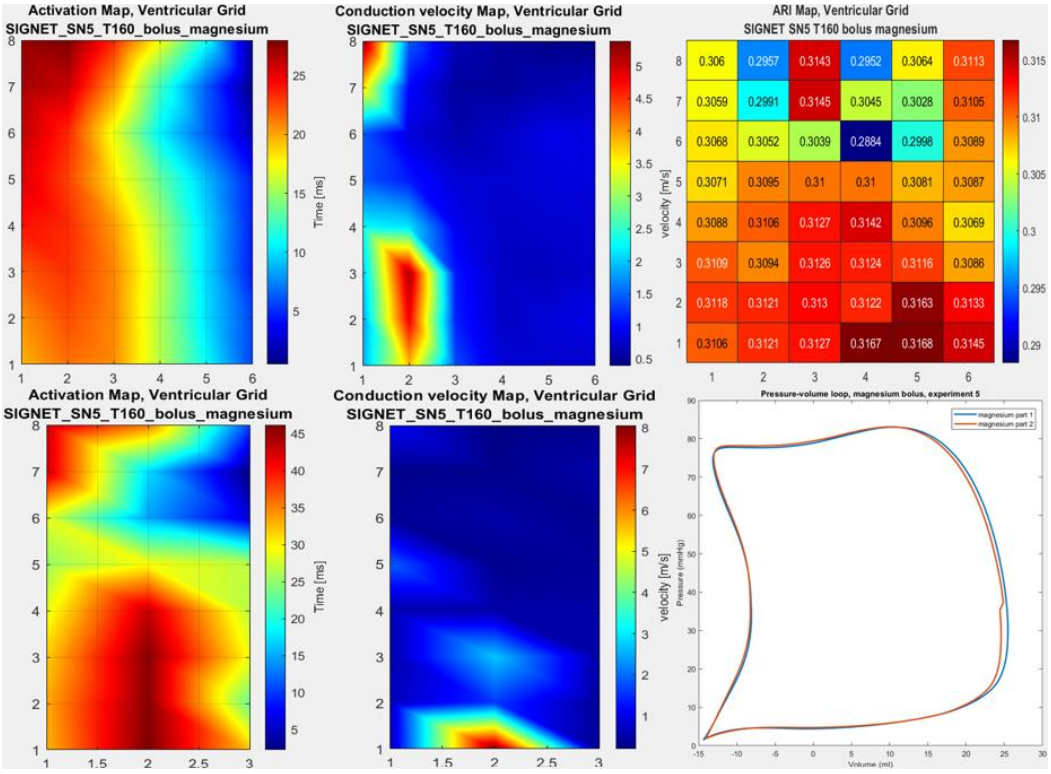

Figure A31: Top row from left to right, activation map, CV map and ARI map from the unipolar electrograms. Bottom row from left to right, activation map and CV map from the bipolar electrograms and the last figure contains the PV-loops during a magnesium bolus. These figures represent the results from experiment 5 during 2-chamber configuration.

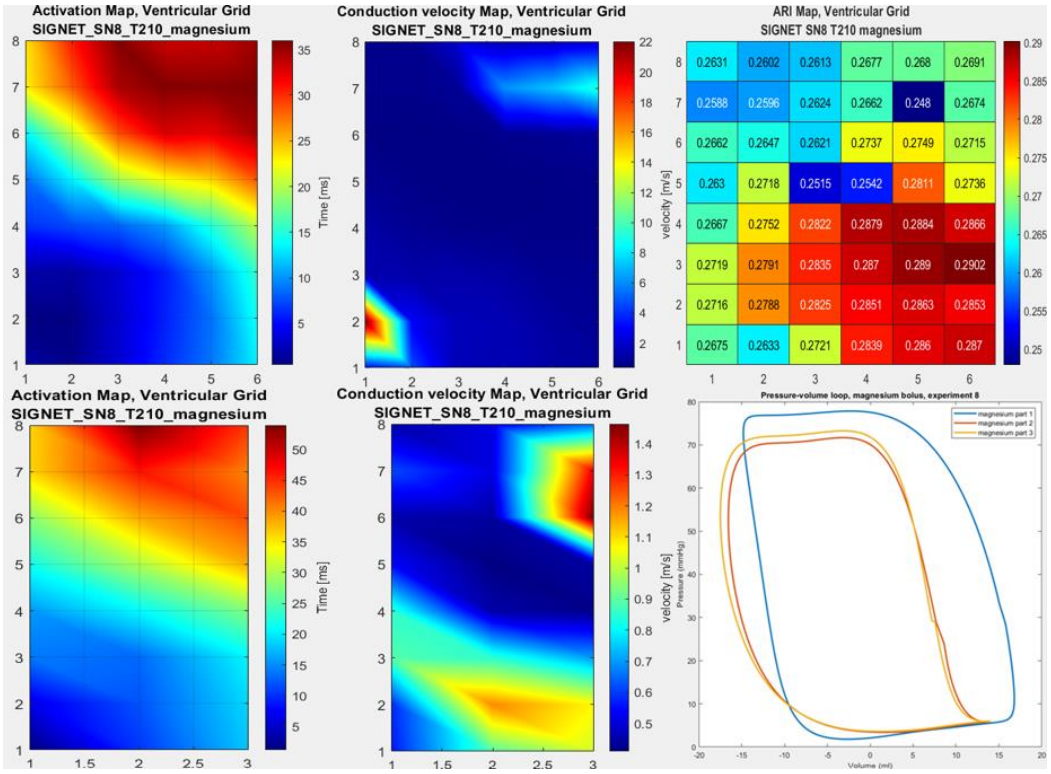

Figure A32: Top row from left to right, activation map, CV map and ARI map from the unipolar electrograms. Bottom row from left to right, activation map and CV map from the bipolar electrograms and the last figure contains the PV-loops during a magnesium bolus. These figures represent the results from experiment 8 during 4-chamber configuration.

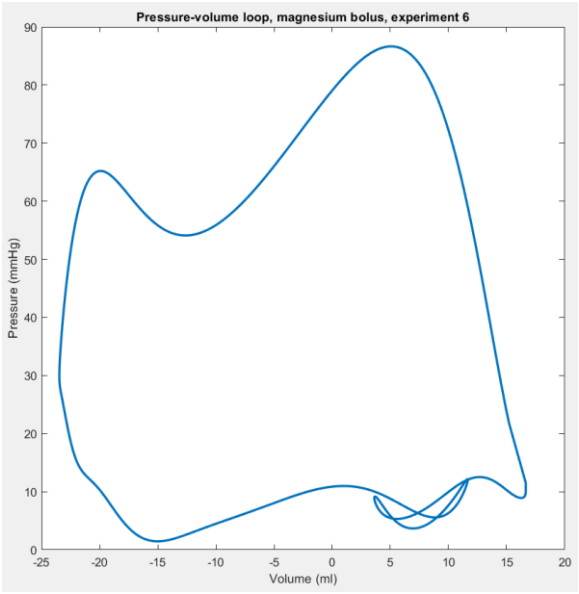

Figure A33: PV loop of a magnesium bolus from experiment 6 in a 2-chamber configuration.

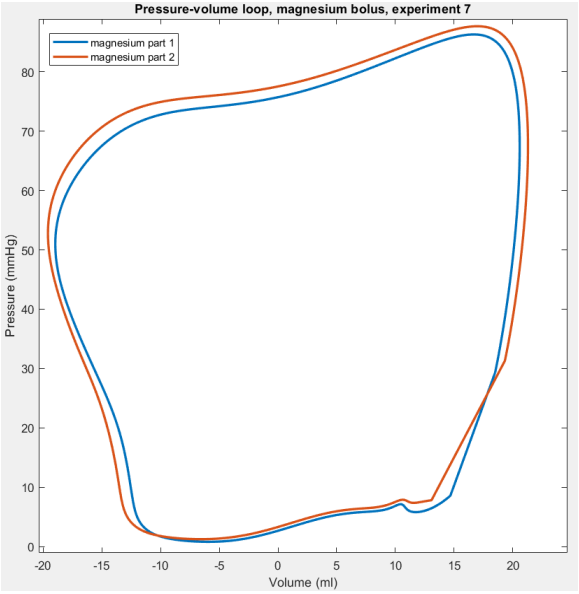

Figure A34: PV loop of a magnesium bolus from experiment 7 in a 4-chamber configuration.

Potassium bolus

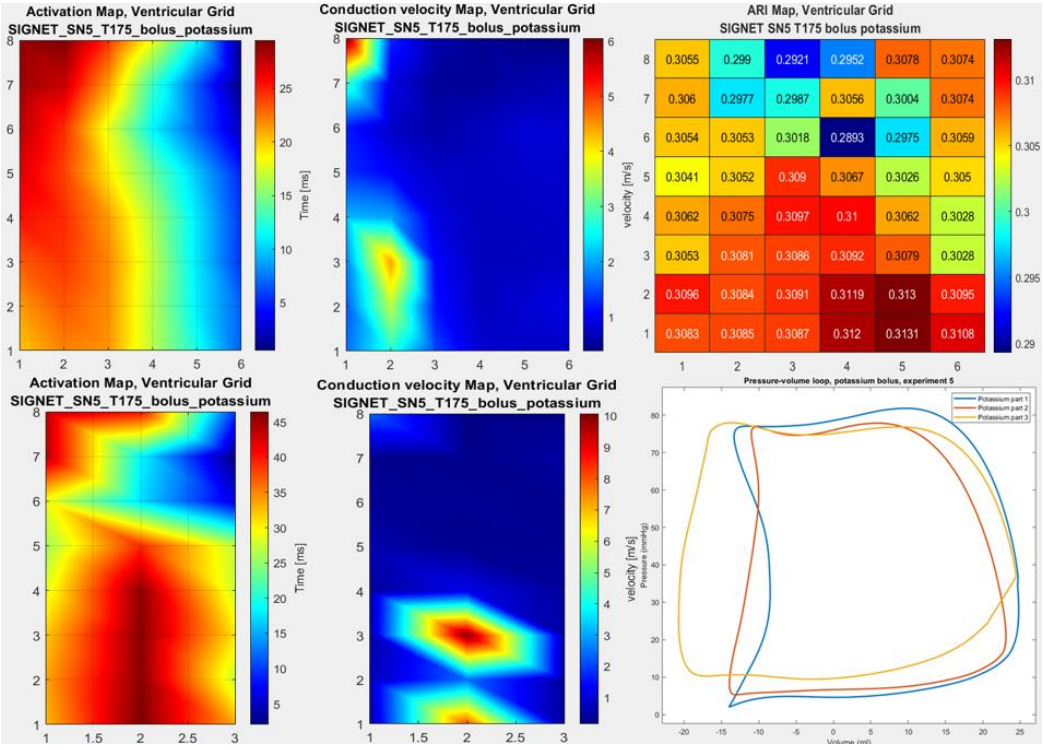

Figure A35: Top row from left to right, activation map, CV map and ARI map from the unipolar electrograms. Bottom row from left to right, activation map and CV map from the bipolar electrograms and the last figure contains the PV-loops during a potassium bolus. These figures represent the results from experiment 5 during 2-chamber configuration.

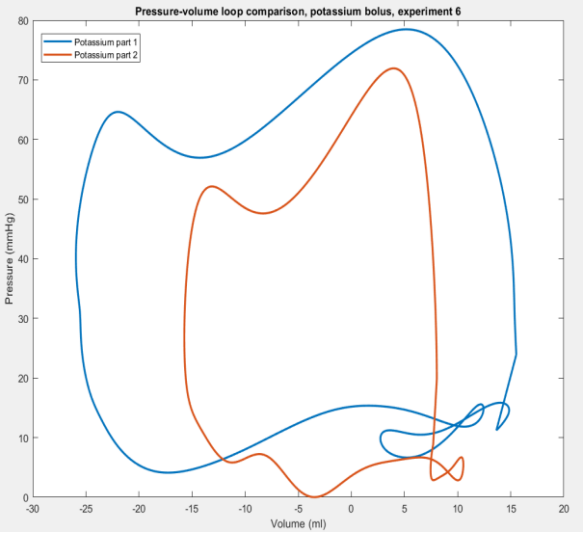

Figure A36: PV loops of a potassium bolus from experiment 6 in a 2-chamber configuration.